TU Delft

Delft University of Technology

# Characteristics of slurry transport regimes

## Insights from experiments and interface-resolved Direct Numerical Simulations

Shajahan, Tariq; Schouten, Thijs; Raaghav, Shravan K.R.; van Rhee, Cees; Keetels, Geert; Breugem, Wim Paul

**DOI**
10.1016/j.ijmultiphaseflow.2024.104831

**Publication date**
2024

**Document Version**
Final published version

**Published in**
International Journal of Multiphase Flow

**Citation (APA)**
Shajahan, T., Schouten, T., Raaghav, S. K. R., van Rhee, C., Keetels, G., & Breugem, W. P. (2024). Characteristics of slurry transport regimes: Insights from experiments and interface-resolved Direct Numerical Simulations. *International Journal of Multiphase Flow*, *176*, Article 104831. https://doi.org/10.1016/j.ijmultiphaseflow.2024.104831

**Important note**
To cite this publication, please use the final published version (if applicable).
Please check the document version above.

**Copyright**
Other than for strictly personal use, it is not permitted to download, forward or distribute the text or part of it, without the consent of the author(s) and/or copyright holder(s), unless the work is under an open content license such as Creative Commons.

**Takedown policy**
Please contact us and provide details if you believe this document breaches copyrights.
We will remove access to the work immediately and investigate your claim.

*This work is downloaded from Delft University of Technology.*
*For technical reasons the number of authors shown on this cover page is limited to a maximum of 10.*

International Journal of Multiphase Flow 176 (2024) 104831

Contents lists available at ScienceDirect

International Journal of Multiphase Flow

journal homepage: www.elsevier.com/locate/ijmulflow

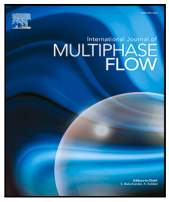

# Characteristics of slurry transport regimes: Insights from experiments and interface-resolved Direct Numerical Simulations

Tariq Shajahan [a], Thijs Schouten [b], Shravan K.R. Raaghav [a], Cees van Rhee [b], Geert Keetels [b], Wim-Paul Breugem [a,*]

[a] Laboratory for Aero & Hydrodynamics, Delft University of Technology, 2628 CD Delft, The Netherlands
[b] Dredging Engineering, Delft University of Technology, 2628 CD Delft, The Netherlands

ARTICLE INFO

Dataset link: https://doi.org/10.4121/a3aa03d5-f01b-4de3-8e29-5766bd11489e

*Keywords:*
Slurry transport
Flow regimes
Pipe flow
Experiments
Interface-resolved Direct Numerical Simulation

ABSTRACT

A common way to transport solids in large quantities is by using a carrier fluid to transport the solids as a concentrated solid/liquid mixture or *slurry* through a pipeline. Typical examples are found in dredging, mining and drilling applications. Dependent on the slurry properties and flow conditions, horizontal slurry pipe flow is either in the fixed-bed, sliding-bed or fully-suspended regime. In terms of non-dimensional numbers, the flow is fully characterized by the bulk liquid Reynolds number ($Re$), the Galileo number ($Ga$, a measure for the tendency of particles to settle under gravity), the solid bulk concentration ($\phi_b$), the particle/fluid density ratio ($\rho_p/\rho_f$), the particle/pipe diameter ratio ($D_p/D_{pipe}$), and parameters related to direct particle interactions such as the Coulomb coefficient of sliding friction ($\mu_c$). To further our fundamental understanding of the flow dynamics, we performed experiments and interface-resolved Direct Numerical Simulations (DNS) of slurry flow in a horizontal pipe. The experiments were performed in a transparent flow loop with $D_{pipe} = 4$ cm. We measured the pressure drop along the pipeline, the spatial solid concentration distribution in the cross-flow plane through Electrical Resistance Tomography (ERT), and used a high-speed camera for flow visualization. The slurry consisted of polystyrene beads in water with $D_p = 2$ mm, $\rho_p/\rho_f = 1.02$, $Ga$ between 40–45 and $\phi_b$ between 0.26–0.33. The different flow regimes were studied by varying the flow rate, with $Re$ varying from 3272 till 13830. The simulations were performed for the same flow parameters as in the experiments. Taking the experimental uncertainty into account, the results from the DNS and the experiments are in reasonably good agreement. The results for the pressure drop agree also fairly well with popular empirical models from literature. In addition, we performed a parametric DNS study in which we solely varied $Re$ and $Ga$. In all flow regimes, a secondary flow of Prandtl's second kind is present, ascribed to the presence of internal flow corners and a ridge of densely packed particles at the pipe bottom during transition towards the fully-suspended regime. In the bulk of the turbulent flow above the bed, secondary flow transport of streamwise momentum dominates over turbulent diffusion in regions where the secondary flow is strong and vice versa where it is weak. The transition between flow regimes appears to be governed by the competition between the net gravity force on the particles and shear-induced particle migration from particle–particle interactions. This competition can be expressed by the Shields number, $\theta$. For $\theta \lesssim 0.75$, gravity is dominant and the flow is in the fixed-bed regime. For $\theta \gtrsim 0.75$, shear-induced migration becomes progressively more important for increasing $\theta$. Low-concentration zones flanking the sliding bed start to form at the top corners of the bed, and gradually expand downwards along the pipe wall till the pipe bottom is reached. For $\theta \gtrsim 1.5$, shear-induced migration is responsible for lifting the particle bed away from the wall, associated with the onset of the suspended regime. For $\theta \gg 1$, gravity is of minor importance and the mean flow eventually reaches axi-symmetry with a high-concentration particle core at the pipe center and negligible secondary flow.

## 1. Introduction

Slurry transport refers to the flow of a concentrated mixture of insoluble solid matter in a liquid. A thorough understanding of slurry flow physics is relevant to the design and operation of slurry pipelines in many applications such as the transport of domestic waste in sanitation systems (Radhakrishnan, 2019), excavated soil in dredging (Miedema,

* Corresponding author.
*E-mail address:* W.P.Breugem@tudelft.nl (W.-P. Breugem).

https://doi.org/10.1016/j.ijmultiphaseflow.2024.104831
Received 3 August 2023; Received in revised form 6 March 2024; Accepted 14 April 2024
Available online 23 April 2024
0301-9322/© 2024 The Author(s). Published by Elsevier Ltd. This is an open access article under the CC BY license (http://creativecommons.org/licenses/by/4.0/).

2016), coal in mining (Chen et al., 2009), debris in drilling (Gurung et al., 2016) and food and materials in process industry (Lareo et al., 1997). Slurries can also be observed in nature such as the transport of sediments in rivers. The fundamental challenges in studying slurry flows arise from, first, the carrier fluid, which is typically turbulent and characterized by a broad spectrum of 3D fluctuating motions and flow structures with different length and time scales (Pope, 2000). Here, the principal mechanisms and coherent flow structures by which turbulence in slurry flows is maintained and how solids are distributed across the pipe (Miedema, 2016), are still not fully understood. Second, the hydrodynamic particle–particle interactions (e.g., lubrication) and collisions are complex (Stickel and Powell, 2005). Third, the solids exhibit typically a distribution in shape, size and mass density. These features of the flow result in a multitude of non-linear fluid/solid (two-way) and solid/solid (four-way) interactions (Balachandar and Eaton, 2010; Elghobashi, 1994). Another complicating aspect is that slurries are generally opaque, which prohibits the use of optical diagnostics such as Particle Image Velocimetry (Deen et al., 2002).

In the present study, we focus our attention on the transport of slurries in horizontal pipelines. This is of relevance to the dredging industry in the Netherlands to maintain coastal and inland waterways and so historically the dynamics of slurry transport have been of long-standing interest. The behavior of slurry flows can vary significantly depending on the operating conditions and slurry characteristics and may severely impact the operation of slurry pipelines. For instance, formation of stationary deposits may block the pipe and a sliding bed layer may increase wear of pipelines. Additionally, it is desired to estimate the pressure drop accurately to optimally position booster pumps along the pipeline.

Based on their behavior, slurry flows have been broadly classified into different slurry transport regimes. However, there has been a lot of ambiguity in defining the different transport regimes, ranging from three regimes defined by Doron and Barnea (1996) to even nine regimes defined by Ramsdell and Miedema (2013). For simplicity we defer to the characterization of the three basic transport regimes as defined by Doron and Barnea (1996), which are the fixed-bed regime (where most particles are settled at the pipe bottom and are at rest), the sliding-bed regime (where a fraction of the particles is suspended in the flow and a bed of particles slides along the pipe bottom), and the fully-suspended regime (where all particles are completely suspended in the flow).

The complexity in the dynamics of the flow regimes arises from the interplay between turbulence, buoyancy effects, and particle/particle and particle/wall lubrication and collision forces. In terms of non-dimensional numbers, the flow dynamics are governed by the bulk liquid Reynolds number $Re = v_{bl} D_{pipe}/\nu_f$, the Galileo number $Ga = \sqrt{(\rho_p/\rho_f - 1)|\tilde{\mathbf{g}}| D_p^3/\nu_f^2}$ that measures the tendency of particles to settle under gravity (Raaghav et al., 2022), the bulk solid volume concentration $\phi_b = (\pi N D_p^3/6)/(\pi D_{pipe}^2 L_{pipe}/4)$ with $N$ the number of particles in a pipe segment of length $L_{pipe}$, the particle-to-pipe diameter ratio $D_p/D_{pipe}$, the solid-to-fluid density ratio $\rho_p/\rho_f$ and parameters related to direct particle/particle interactions such as the Coulomb coefficient of sliding friction $\mu_c$. Here, $v_{bl}$ is the liquid bulk velocity, $D_{pipe}$ is the pipe diameter, $\nu_f$ is the kinematic viscosity of the liquid, $D_p$ is the particle diameter and $\tilde{\mathbf{g}}$ is the gravitational acceleration.

The early research on slurry transport in pipelines was focused on the development of empirical and semi-empirical models for the Limit Deposit Velocity (LDV) (Durand and Condolios, 1953; Wilson, 1942; Turian et al., 1987), often defined as the bulk mixture velocity below which a bed starts to form, and the pressure drop along the pipeline (Durand, 1953; Vocadlo and Charles, 1972; Doron et al., 1987; Gibert, 1960). Some models, such as proposed by Durand and Condolios (1953) and Führböter (1961) are still widely used in the industry. However, most models contain empirical coefficients obtained from a best fit with available experimental data and hence rely heavily on the accuracy of the experimental data used. Furthermore, they work reasonably well under conditions for which these coefficients have been determined, but may fail when applied to slurries with different characteristics and under other flow conditions (Miedema, 2016).

In the later research on slurry transport, mechanistic layer models were developed, which treat different strata of the pipe as different layers having distinct physical dynamics. Wilson et al. (2006) proposed a two-layer and a three-layer model based on force equilibrium for the bed. Doron et al. (1987) introduced a two-layer model considering a bed layer at the bottom and a heterogeneous mixture above. This work was further extended by Doron and Barnea (1993) to a three-layer model that included a stationary layer at the bottom, a moving bed layer in the middle, and a heterogeneous mixture layer on top. Furthermore, multicomponent models were proposed for slurries with a broad particle size distribution, in which distinction is made between, e.g., fluid, pseudo-homogeneous, and fully stratified components (Wilson and Sellgren, 2016). Since the layer models are bound by physical laws, their application may be extended beyond the parameters of any specific setup. However, the layer models are still strongly dependent on many assumptions and closure relations in their governing equations. An overview of the above described models is provided by Miedema (2016).

Computational Fluid Dynamics (CFD) simulations facilitate a more detailed analysis of the flow regimes in slurry transport. In recent years, Eulerian-based continuum models have become increasingly popular to simulate liquid–solid flows, see, e.g., the review by Messa and Matoušek (2020). Ling et al. (2003) proposed a simplified 3D Algebraic Slip Mixture (ASM) model combined with the Renormalization Group (RNG) $k-\epsilon$ turbulence model, showing good predictions for the mean pressure gradient in fully developed turbulent flows. In other studies, the Two-Fluid Model (TFM) has been used for slurry flow modeling in which the solid and liquid phases are treated as two interpenetrating fluids. Ekambara et al. (2009) conducted TFM simulations using the Kinetic Theory of Granular Flows (KTGF) for modeling the solids stress tensor, achieving overall good agreement with experimental data for slurry flow. Kaushal et al. (2012) simulated slurry pipe flow using the ASM and TFM/KTGF models to test the performance of the different modeling approaches. Capecelatro and Desjardins (2013a,b) developed an Euler–Lagrange Large Eddy Simulation (LES) framework. They model the fluid phase as a continuum as in the TFM approach, while a Discrete Particle Model (DPM) is used to track particles individually from the forces acting on them. The latter enables the treatment of particle collisions in a direct manner. Unlike the RANS approach, in their LES approach the large-scale turbulent motions are explicitly resolved. The same Euler/Lagrange LES framework was also applied in a later study on slurry pipe flow by Arolla and Desjardins (2015). Uzi and Levy (2018) combined DPM for the particles with a RANS approach for the fluid phase using the $k-\epsilon$ turbulence model. The effect of the particles on the liquid flow was modeled through the inclusion of a liquid-particle interaction source term at the right-hand side of the momentum equations. Finally, Zhang et al. (2021a,b, 2022) employed an Euler–Lagrange framework to study the behavior of particle-laden gas–solid flows in a horizontal pipe. They used a fine computational grid for the fluid phase and referred to their approach as Direct Numerical Simulation (DNS) combined with four-way coupled Lagrangian Particle Tracking (LPT). However, the equations solved in their approach are similar as in the LES/DPM approach of Capecelatro and Desjardins (2013a) but with omission of the subfilter-scale Reynolds stress. This approximation is expected to hold only for sufficiently small particles, in which case the implicit filter length associated with the Volume-Averaged Navier–Stokes (continuum) equations is small compared to the length scales of turbulence (Breugem et al., 2006).

From the above brief overview of different CFD approaches used to simulate slurry pipe flow, it appears that the Euler–Lagrange LES/DPM approach of Capecelatro and Desjardins (2013b) and Arolla and Desjardins (2015) is the most detailed one. An even more detailed approach would be interface-resolved Direct Numerical Simulation (DNS)

(Maxey, 2017) in which the flow is resolved completely by solving the Navier–Stokes and Newton–Euler equations for the fluid and the individual particles, respectively. Obvious advantages of interface-resolved DNS over LES are that (a) no turbulence modeling is required in DNS, and (b) the flow around the particles is explicitly resolved, avoiding the need of parameterizing the particle/fluid interaction forces as in LES. Interface-resolved DNS was used by Kidanemariam and Uhlmann (2014, 2017) to study sediment pattern formation in channel flow. However, to the best of the authors' knowledge, interface-resolved DNS has not been applied yet to slurry pipe flow.

An intriguing aspect of particle-laden pipe flows is the presence of a mean secondary flow (Kaushal et al., 2012; Zhang et al., 2021b, 2022; Liu et al., 2023), i.e., mean fluid and particle motions perpendicular to the main flow direction. Secondary flows have been widely studied for single-phase flows. Commonly, a distinction is made between secondary flow of Prandtl's first kind, originating from centrifugal forces acting on the flow in a curved channel, and secondary flow of Prandtl's second kind in non-circular ducts related to the generation of mean streamwise vorticity by spatial gradients in Reynolds stresses (Prandtl, 1952; Bradshaw, 1987; Nezu, 2005; Larsson et al., 2011). Nikitin et al. (2021) provide a recent review of experimental, theoretical and numerical studies on secondary flows of the second kind in a number of different flow geometries and also discuss the effect of variations in surface roughness. For square ducts, the secondary flow in the vicinity of a corner is characterized by a pair of two counter-rotating streamwise vortices centered around the corner bisector. This can be explained from turbulent (fluctuating) fluid motions along arc-shaped paths near the corner, causing a mean excess pressure in the corner through centrifugal forces and which subsequently drives an outward-directed mean flow parallel to the adjacent walls (Nikitin et al., 2021).

For single-phase duct flows, turbulent motions are a prerequisite for the appearance of a secondary flow. Interestingly, for duct flows laden with neutrally-buoyant particles, the interface-resolved DNS study of Kazerooni et al. (2017) shows that a secondary flow is also present in the laminar regime. They ascribed this to spatial gradients in particle-induced stresses similar to the generation of secondary flow in the turbulent regime by spatial gradients in Reynolds stresses. This study was extended by Fornari et al. (2018) to duct flow of neutrally-buoyant suspensions in the turbulent regime. The particles were found to preferentially accumulate near the duct corners and to enhance the secondary flow intensity at the lower bulk solid volume fractions (0.05 and 0.1) compared to the unladen case, while they accumulated preferentially in the core and reduced the secondary flow intensity at the highest bulk solid volume fraction (0.2). Similar findings are reported in the interface-resolved DNS study of Lin et al. (2017b) for the low and moderate concentration range (0.0078–0.0707). In another study, Lin et al. (2017a) found that heavy particles break down the up–down symmetry of the secondary flow patterns. Sedimentation causes a stronger downward flow in the top-central region of the duct and an enhanced upward flow along the side walls. The breakdown of up–down flow symmetry and an enhanced upward flow along the side walls was also found by Zade et al. (2019) in a combined experimental/numerical study of relatively heavy particles in turbulent duct flow. The enhanced upward secondary flow was likely responsible for a higher elevation of the suspended particles near the side walls.

Compared to particle-laden duct flows, the presence of a mean secondary flow in particle-laden pipe flows has received much less attention. Liu et al. (2023) studied the behavior of heavy particles in a turbulent gas flow through a semi-circular pipe section using LES combined with one-way coupled Lagrangian Particle Tracking. The presence of a mean secondary flow was found to have a significant impact on the spatial particle distribution and on particle deposition and resuspension from the pipe floor. In two numerical studies of horizontal gas–solid pipe flow based on a four-way coupling Euler–Lagrange approach, Zhang et al. (2021b, 2022) identified different flow regimes as function of the governing flow parameters and explored the characteristics and underlying mechanisms of the mean secondary flow in each regime. To our knowledge, secondary flow patterns have not yet been systematically explored for liquid–solid slurry pipe flows.

The aim of this work is to gain insight into the structure and dynamics of slurry pipe flow in the different transport regimes by means of both experiments and interface-resolved DNS. We want to address the following research questions: (1) How do the results from the experiments compare to the results from the DNS at the same flow conditions? (2) What are the main characteristics of the different flow regimes? (3) More specifically, how do mean secondary flow patterns evolve across the different flow regimes and what are the physical mechanisms responsible for their creation? (4) What is the relative importance of the mean secondary flow, the Reynolds stress (from turbulent motions) and the particle stress to transport of mean streamwise momentum across the pipe? (5) What is the effect of solely varying $Re$ or $Ga$ on the dynamics of slurry pipe flow? (6) What are the physical mechanisms governing the transition between flow regimes? And, related to this, what dimensionless number can be used as an appropriate metric for the transition between flow regimes?

The experiments were performed in a 4 cm-diameter circulating slurry flow loop using 2 mm-diameter polystyrene balls in water. The polystyrene/water density ratio is only slightly larger than one. Therefore a fully-suspended state could be reached at fairly low Reynolds number within the computational reach of DNS. For the DNS a computationally efficient Immersed Boundary method (IBM) was used for the fluid/solid coupling on a fixed grid. A frictional soft-sphere collision model was employed to model particle–particle interactions. The same flow conditions were used for the DNS as in the experiments to allow for a comparison of the numerical results with the experimental data.

The remainder of this manuscript is structured as follows. In Sections 2, 3 and 4, we describe, respectively, the governing equations, the experimental slurry flow loop and the computational setup. The volume and time averaging used to analyze the DNS data, is explained in Section 5. Following which, a comparison of the experiments and the DNS is provided in Section 6. Furthermore, results from additional DNS are provided in Section 7 to study the influence of $Re$ and $Ga$ on the dynamics of slurry transport. Finally, the main conclusions and a discussion are given in Section 8.

## 2. Governing equations

The particles in the present study are non-colloidal (non-Brownian) spheres, which are (nearly) monodisperse in size and density. The particles' motions are governed by the Newton–Euler equations. The carrier fluid is a Newtonian liquid and governed by the incompressible Navier–Stokes equations. The governing equations are made non-dimensional using $D_p$ as a characteristic length scale, $v_{bl}$ as a characteristic velocity scale and the ratio $D_p/v_{bl}$ as a characteristic time scale. The non-dimensional Navier–Stokes equations are then given by:

$$\nabla \cdot \mathbf{u}_f = 0\,, \tag{1a}$$

$$\left(\frac{\partial \mathbf{u}_f}{\partial t} + \nabla \cdot \mathbf{u}_f \mathbf{u}_f\right) = -\nabla p_e - \nabla p + \left(\frac{1}{Re}\frac{D_{pipe}}{D_p}\right)\nabla^2 \mathbf{u}_f\,, \tag{1b}$$

where $\mathbf{u}_f$ is the fluid velocity vector, $p$ is the modified fluid pressure defined as $p = p_{tot} - \nabla p_e \cdot \mathbf{x} - \mathbf{g}\cdot\mathbf{x}$ with $p_{tot}$ the total fluid pressure and $\mathbf{g} = \tilde{\mathbf{g}} D_p / v_{bl}^2$, and $\nabla p_e$ is the externally imposed pressure gradient that drives the flow. We remark that the non-dimensional gravitational acceleration is related to the well-known Galileo number $Ga$ for gravitational particle settling as:

$$|\mathbf{g}| = \left(\frac{Ga}{Re}\frac{D_{pipe}}{D_p}\right)^2 \frac{1}{(\rho_p/\rho_f - 1)}\,. \tag{2}$$

The non-dimensional Newton–Euler equations are given by:

$$\frac{\rho_p}{\rho_f}\frac{d\mathbf{u}_p}{dt} = \frac{6}{\pi}\left(\oint_{\partial V} (\boldsymbol{\tau}_f \cdot \mathbf{n}) dA + \frac{\pi}{6}\left(\frac{\rho_p}{\rho_f} - 1\right)\mathbf{g} - \frac{\pi}{6}\nabla p_e + \mathbf{F}_c\right), \tag{3a}$$

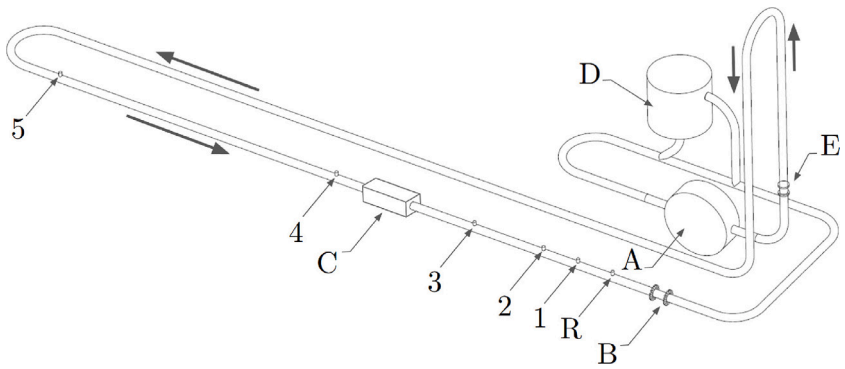


**Fig. 1.** Experimental slurry loop setup, where A, B, C, D and E, indicate the locations of the centrifugal pump, ERT measuring planes, location where high-speed camera images were taken, sump and magnetic flow meter, respectively. The numbers 1-5 correspond to the locations of the pressure transmitters. The arrows indicate the flow direction.

$$\frac{\rho_p}{\rho_f}\frac{d\boldsymbol{\omega}_p}{dt} = \frac{60}{\pi}\left(\oint_{\partial V} \mathbf{r}\times(\boldsymbol{\tau}_f\cdot\mathbf{n})dA + \mathbf{T}_c\right), \tag{3b}$$

where $\mathbf{u}_p$ and $\boldsymbol{\omega}_p$ are the translational and rotational velocity of the particle, respectively, $\rho_p$ and $\rho_f$ are the solid and liquid mass density, respectively, $\mathbf{r}$ is the position vector with respect to the particle centroid, $\mathbf{n}$ is the unit normal vector directed from the surface ($\partial V$) of the particle into the fluid, $\boldsymbol{\tau}_f = -p\mathbf{I} + (1/Re)(D_{pipe}/D_p)(\nabla\mathbf{u}_f + \nabla\mathbf{u}_f^T)$ is the modified stress tensor for a Newtonian fluid based on the modified pressure and with $\mathbf{I}$ the unit tensor, and $\mathbf{F}_c$ and $\mathbf{T}_c$ are, respectively, the collision force and collision torque acting on the particle.

The Navier–Stokes and Newton–Euler equations are coupled with each other through the no-slip/no-penetration condition at the surface of the particles:

$$\mathbf{u}_f = \mathbf{u}_p + \boldsymbol{\omega}_p\times\mathbf{r} \text{ at } \partial V\,. \tag{4}$$

Finally, the fluid phase has to obey the no-slip/no-penetration condition at the pipe wall.

The governing equations imply that the slurry flow dynamics are governed by the following non-dimensional numbers: $Re$, $Ga$, $\phi_b$, $D_p/D_{pipe}$, $\rho_p/\rho_f$, and the parameters related to particle collisions discussed later.

## 3. Experimental setup

The experimental setup is shown in Fig. 1. It comprises an optically transparent plexiglass pipe with a diameter of 4 cm and 10 m long, and a 2 m high U-loop. The slurry consisting of water and polystyrene particles is driven by a centrifugal pump (A). The measuring section of the circuit is 4.65 m long and is equipped with a dual-plane Electric Resistance Tomography (ERT Z8000) sensor (B) to measure the spatial concentration distribution within the cross-flow plane. The ERT sensor is positioned at the end of the horizontal test section at a distance of 403 cm from the upstream bend and 23 cm before the downstream bend, which is well within the region where effects of both bends can be safely neglected. From the ERT data the bulk concentration $\phi_b$ in the test section was determined by integrating the spatial distribution over the cross-section. A high-speed camera with a frame rate of 1125 Hz (C) is placed at a distance of 214 cm from the upstream bend and thus in a well developed region of the flow. During operation, the bypass is opened and the inlet to the sump (D) is closed, allowing the polystyrene particles to enter the slurry loop by the action of gravity.

Differential pressure measurements are taken (using Rosemount 1151 DP4S22 pressure transmitters) at 5 different positions along the measurement section at distances of 35 cm, 75 cm, 132 cm, 167 cm and 377 cm, respectively, from the reference point (R). The uncertainty in the pressure transmitters is 2.5 Pa. An EndressHauser promag 55S40 magnetic flow meter (E) is used to measure the liquid bulk velocity (Bernier and Brennen, 1983; Xu et al., 2009) in the riser section of the U-loop with an instrumental uncertainty of 0.002 m/s.

Additional tilted flume experiments were performed to determine the Coulomb coefficient of static friction for particle-particle contacts and particle-wall contacts. In Appendix A we provide details of the measurements of the material properties. The density ratio of the polystyrene particles to water was determined to be $\rho_p/\rho_f = 1.02$. The ratio of the pipe diameter to the particle diameter is 20. The temperature in the three investigated cases was measured and this was used to determine the water viscosity and density. The experiments were conducted at different $Re$ with the aim of accessing different transport regimes.

Originally, pressure sensors were placed in the riser and downcomer section of the U-loop with the intention of determining the bulk concentration from the difference in vertical pressure gradient between the riser and the downcomer, which could then be combined with the liquid bulk velocity measurement from the magnetic flow meter (E) to obtain the liquid flow rate. However, the obtained signal turned out to be too noisy as a result of the small density difference between the polystyrene spheres and water, and was therefore disregarded. The problem in determining the liquid flow rate was overcome by an estimate based on equating the solid and fluid volume fluxes in the *horizontal* test section and the corresponding fluxes in the *vertical* riser. The final estimation of the intrinsic liquid bulk velocity in the test section, $v_{bl}$, involved three steps. First, the solid volume flux in the test section was estimated using a combination of the velocity profile of the particles (estimated from the video recordings) and the concentration profile (obtained from the ERT sensor) as function of height in the pipe. Second, the solid volume flux balance over the horizontal test section and the vertical riser was used to estimate the concentration of particles in the riser. This was then used to estimate the fluid volume flux in the riser based on an empirical correlation for the macroscopic particle/fluid slip velocity. Third, the fluid volume flux balance over the test section and the riser was used to finally estimate the liquid bulk velocity in the test section. In Appendix B we provide a detailed description of the estimation and the assumptions used.

Though it was intended to maintain $\phi_b$ constant at a value of 0.25 (25%), it was observed *a posteriori* from the ERT measurements that the bulk concentration of particles in the test section was higher than originally planned due to an increased settling of particles in horizontal sections of the slurry loop when lowering the flow rate. The parameters $Re$, $Ga$ and $\phi_b$ corresponding to the experimental runs are listed in Table 1. This table also provides the values for the densimetric Froude number defined as $Fr = v_{mix}/\sqrt{(\rho_p/\rho_f - 1)|\tilde{\mathbf{g}}|D_{pipe}}$, where $v_{mix}$ is the mixture bulk velocity defined as the sum of the liquid and solid flow rate divided by the pipe cross-sectional area. The densimetric Froude number is often used to assess whether particles will deposit on the bottom of the pipe. According to Miedema (2016) (p. 156), the critical mixture velocity below which a bed will be present, corresponds to $Fr \approx 2$ for large particles as considered here. Based on the computed values we expect a bed for case E1 and possibly also for case E2.

**Table 1**
Flow parameters in the experiments and the DNS: $Re$, $Ga$, $\phi_b$ and $Fr$, which correspond to the bulk liquid Reynolds number, the Galileo number, the solid bulk concentration and the densimetric Froude number, respectively. See main text for definitions of these numbers. E1–E3 refer to the experimental runs and D1–D3 are the corresponding DNS using the values of the governing dimensionless numbers estimated from the experiments. S1–S5 are additional DNS for a parametric study on the effect of $Re$ and $Ga$ on the flow dynamics where all other parameters were kept fixed. The particle-to-fluid density ratio is $\rho_p/\rho_f = 1.02$ and the pipe-to-particle diameter ratio is $D_{pipe}/D_p = 20$.

| Case | $Re$ | $Ga$ | $\phi_b$ | $Fr$ |
|---|---|---|---|---|
| D1/E1 | 3272 | 44.0 | 0.325 | 0.60 |
| D2/E2 | 8513 | 43.6 | 0.284 | 2.00 |
| D3/E3 | 13 830 | 43.2 | 0.268 | 3.67 |
| S1 | 2500 | 37.9 | 0.25 | 0.56 |
| S2 | 5200 | 37.9 | 0.25 | 1.30 |
| S3 | 7100 | 37.9 | 0.25 | 1.90 |
| S4 | 12 000 | 37.9 | 0.25 | 3.56 |
| S5 | 12 000 | 18.9 | 0.25 | 7.45 |

## 4. Computational setup

Interface-resolved Direct Numerical Simulations (DNS) were carried out for a cylindrical pipe filled with a viscous fluid and a prescribed bulk concentration of solid spheres, see Fig. 2. A Cartesian coordinate system was used where the axis of the pipe was aligned with the $y$ direction and gravity was acting in the negative $z$ direction. A total of eight simulations were performed, see Table 1. The governing dimensionless numbers in cases D1–D3 were chosen to match the estimated dimensionless numbers from the corresponding experiments, cases E1–E3, respectively. In addition, a parametric study was performed to study the sole effect of varying the bulk liquid Reynolds number while all other numbers were kept fixed, see cases S1–S4. Finally, in case S5 we tested the sensitivity of the flow to a change in Galileo number at the highest investigated Reynolds number.

In the DNS the Navier–Stokes equations are solved using the finite-volume method with a standard fractional step (predictor/corrector) scheme and the three-step Runge–Kutta method for the integration in time. Spatial gradients are approximated by the second-order accurate central-differencing scheme. The DNS makes use of two different grids: a fixed, staggered and isotropic Cartesian grid for the fluid phase and a uniform Lagrangian grid attached to the surface of every particle. The computationally efficient Immersed Boundary Method (IBM) of Breugem (2012) is used for the fluid/solid coupling, which is a modified version of the original method introduced by Uhlmann (2005). The principle of the IBM is that the no-slip/no-penetration condition, Eq. (4), is not imposed in a direct manner, but that forces are locally added to the right-hand side of Eq. (1b) in a thin spherical shell around each particle surface to enforce this condition by good approximation. Main advantage of the IBM is that a simple and continuous fluid grid can be used without the need of regridding every time particles have moved in space. The force distribution is computed from a combination of the regularized delta-function approach introduced by Peskin (1972) and the direct-forcing approach of Fadlun et al. (2000). The fluid/solid coupling is explicit: first the Navier–Stokes equations are integrated to the next time level using the previous particle velocities and positions, then the Newton–Euler equations are integrated in time with the same Runge–Kutta method using the hydrodynamic force and torque computed from the IBM force distribution on the particle surface. As the Cartesian fluid grid did not conform to the cylindrical shape of the pipe, we used another IBM based on a volume-penalization approach to impose the no-slip/no-penetration condition for the fluid on the pipe wall. This method is described in more detail in Appendix C.

The pipe length was set equal to five pipe diameters (100 particle diameters) and a periodic boundary condition is imposed in the streamwise direction. The flow is driven by a streamwise pressure gradient, which is adjusted every time step to maintain a constant intrinsic liquid bulk velocity, see Appendix C for more details. We used the same grid resolutions in all DNS cases, corresponding to $D_p/\Delta x = 16$ ($D_{pipe}/\Delta x = 320$) and 746 Lagrangian grid points on the surface of the particles. This was sufficient to resolve both the turbulent flow structures in the carrier fluid as well as the flow around the particles. The DNS/IBM code has been extensively validated (Breugem, 2012) and was used in many previous studies of, e.g., the rheology of dense neutrally-buoyant suspensions in plane Couette flow (Picano et al., 2013), the behavior of dense neutrally-buoyant suspensions in turbulent channel flow (Picano et al., 2015; Costa et al., 2016, 2018) and the sedimentation of heavy sphere suspensions in the inertial flow regime (Shajahan and Breugem, 2020, 2023). In Appendix C we provide additional validation of the volume-penalization method for turbulent single-phase pipe flow.

Particle–particle and particle–wall collisions and contacts are treated using a soft-sphere collision model described by Costa et al. (2015) which simulates a spring-damper interaction that accounts for the stick–slip nature of frictional collisions. Lubrication effects are automatically accounted for in the DNS, although underresolved at interparticle distances smaller than a grid cell, for which a normal lubrication force correction is added to the right-hand side of Eq. (3a). The lubrication force is capped when the interparticle distance is smaller than a threshold distance of 0.2% of the particle diameter as to mimic the effect of particle roughness on lubrication. Due to the large pipe-to-particle diameter ratio ($D_{pipe}/D_p = 20$), the collision of a particle with the curved pipe wall is treated as a collision with the tangent plane to the pipe wall at the point of particle/wall contact. The collision model depends on three main parameters: the normal and tangential dry coefficients of restitution, $e_n$ and $e_t$, respectively, and the Coulomb coefficient of sliding friction, $\mu_c$. We have chosen $e_n = 0.97$ as this is a typical value for many materials (Costa et al., 2015) and $\mu_c = 0.39$ based on the tilted-flume experiments described in Appendix A. The value of $e_t = 0.1$ is an educated guess given that the particles appear rather smooth; the higher the value of $e_t$, the earlier the transition from stick to slip behavior (Costa et al., 2015).

The particles were initially randomly distributed in space and a laminar Poiseuille (parabolic) profile was prescribed for the streamwise fluid and solid phase velocity. The particles were also initialized with an angular velocity in the azimuthal direction equal to half the vorticity obtained from the prescribed Poiseuille flow. The computational time step was initially adjusted based on the von Neumann stability criteria for the three-step Runge–Kutta scheme used. After a few thousand time steps it was fixed in time at a value well below the maximum allowed value for stable integration in time. The temporal evolution of the flow was monitored by the time series of variables such as the averaged vertical position of the particles, the averaged streamwise velocity of all the particles and the driving streamwise pressure gradient. After the flow reached a fully-developed state, equidistant sampling of the DNS results was started for computing statistics with part of the statistics (e.g., spatial averages) computed and stored during runtime.

To evaluate whether the slurry flow is sufficiently resolved in space, two values for the normalized grid spacing are included in Table 2: one based on the liquid viscosity $\Delta x\, u_\tau/\nu_f$ and one based on the effective suspension viscosity $\Delta x\, u_\tau/\nu_s$ calculated at the prescribed bulk concentration and estimated from Eilers' correlation (Eilers, 1941) with the coefficients taken from Costa et al. (2016). Here, the wall friction velocity $u_\tau$ is used as a first proxy for the typical velocity scale of the large eddies when a turbulent flow is present, given by:

$$u_\tau/u_{bl} = \sqrt{-\frac{1}{4}\left(\frac{D_{pipe}}{D_p}\right)\overline{\frac{dp_e}{dy}}}\,. \tag{5}$$

The effective suspension viscosity $\nu_s$ is estimated from:

$$\nu_s/\nu_f = \left(1 + 1.25\,\frac{\phi_b}{(1-\phi_b/0.64)}\right)^2. \tag{6}$$

While $\nu_f/u_\tau$ may be used as a first estimate of the viscous wall unit for the stratified cases with the presence of a distinct bed and liquid

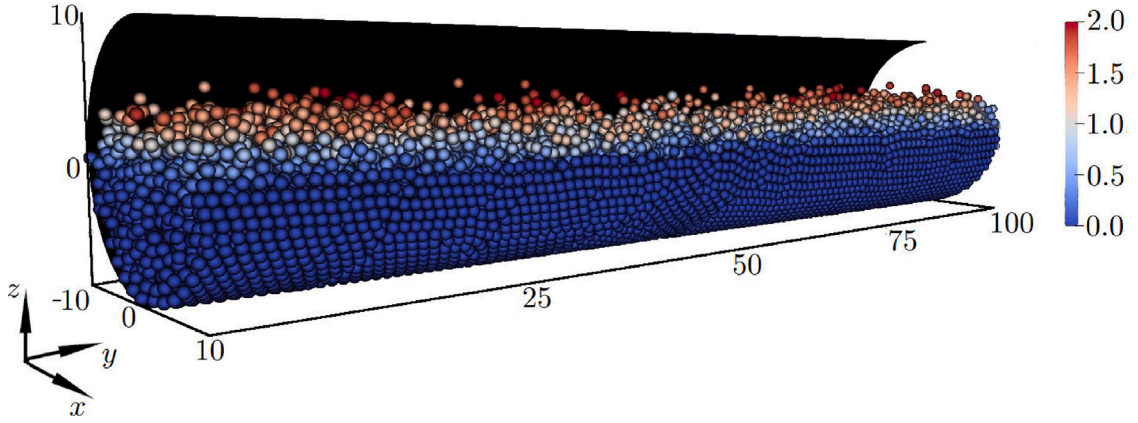


**Fig. 2.** Computational setup used in the DNS (corresponding to case D1, see Table 1). The particles are colored by the streamwise particle velocity $v_p$ scaled with the liquid bulk velocity $v_{bl}$. The fluid is not shown in the figure for clarity. A periodic boundary condition in the streamwise ($y$) direction and a no-slip boundary condition at the pipe wall are imposed. The pipe-to-particle diameter ratio is $D_{pipe}/D_p = 20$ and the pipe has a length of 100 particle diameters.

**Table 2**
Additional parameters and computed numbers from the DNS where $t_{obs}$ is the observation time over which statistics were collected, $N_s$ is the number of samples, $\Delta t$ is the time step, $v_{bs}$ is the mean solid bulk velocity, $v_{bl}$ is the mean liquid bulk velocity, $v_\tau$ is the average wall friction velocity, $\nu_f$ is the viscosity of the fluid, $\nu_s$ is the effective suspension viscosity of the solid/fluid mixture computed from Eilers' empirical model, $Re_\tau$ is the friction Reynolds number, $Re_{\tau,s}$ is the suspension friction Reynolds number and $\theta$ is the Shields number.

| | $t_{obs}v_{bl}/D_p$ | $N_s$ | $\Delta t\, v_{bl}/D_p$ | $v_{bs}/v_{bl}$ | $v_\tau/v_{bl}$ | $\Delta x\, v_\tau/\nu_f$ | $\Delta x\, v_\tau/\nu_s$ | $Re_\tau$ | $Re_{\tau,s}$ | $\theta$ |
|---|---|---|---|---|---|---|---|---|---|---|
| D1 | 2000 | 200 | 0.0125 | 0.13 | 0.20 | 2.02 | 0.61 | 323.3 | 97.0 | 0.54 |
| D2 | 2000 | 200 | 0.0125 | 0.71 | 0.11 | 2.97 | 1.11 | 474.8 | 176.9 | 1.19 |
| D3 | 2000 | 200 | 0.0125 | 1.09 | 0.09 | 3.78 | 1.52 | 604.5 | 243.3 | 1.96 |
| S1 | 800 | 80 | 0.02 | 0.06 | 0.17 | 1.24 | 0.54 | 197.8 | 86.4 | 0.27 |
| S2 | 800 | 80 | 0.02 | 0.38 | 0.12 | 1.96 | 0.86 | 313.5 | 137.0 | 0.68 |
| S3 | 800 | 80 | 0.02 | 0.63 | 0.11 | 2.37 | 1.04 | 379.5 | 165.8 | 1.00 |
| S4 | 4500 | 300 | 0.03 | 1.02 | 0.09 | 3.23 | 1.41 | 516.8 | 225.8 | 1.86 |
| S5 | 4500 | 300 | 0.03 | 1.20 | 0.08 | 3.07 | 1.34 | 491.4 | 214.7 | 6.76 |

flow region, $\nu_s/v_\tau$ is deemed more appropriate for the fully-suspended cases in which the particles are mixed across the pipe (Costa et al., 2016, 2018). The values of $\Delta x\, v_\tau/\nu_f$ for the fixed-bed and sliding-bed cases, and of $\Delta x\, v_\tau/\nu_s$ for the fully-suspended cases are $\mathcal{O}(1)$ and hence the turbulent flow is deemed sufficiently resolved at the grid resolution used.

The proxy for the wall friction velocity was used to calculate a few other numbers whose values are listed in Table 2. $Re_\tau = v_\tau R_{pipe}/\nu_f$ and $Re_{\tau,s} = v_\tau R_{pipe}/\nu_s$ are, respectively, the friction Reynolds number and the suspension friction Reynolds number with $R_{pipe}$ the pipe radius. Finally, the Shields number is defined as $\theta = v_\tau^2/(\rho_p/\rho_f - 1)|\tilde{\mathbf{g}}|D_p$. The Shields number (Shields, 1936; Ouriemi et al., 2007) is another parameter that can be used to distinguish between the regimes, especially at low flow rates, where the onset of particle entrainment in slurry flow is characterized by the balance between shear-induced lift from turbulence and the particle stresses on the one hand and the immersed weight of the particles on the other hand (Guazzelli and Pouliquen, 2018). The values of $\theta$ for cases D1–D3 are all well above the critical Shields number of 0.03–0.04 for the particles and flow conditions considered in the present study (Shields, 1936; van Rijn, 1984), suggesting that a significant portion of the particles will be suspended in all cases. In addition, the high value for $\theta$ in case D3 corresponds to the suspended regime according to the criteria given by van Rijn (1984).

## 5. Volume and time averaging

In the post-processing of the raw DNS data, first the data was averaged over the streamwise direction and then time averaged. Since both averaging operators are linear, the sequence in which they are applied to the data does not matter. The *superficial* volume and time average of the streamwise particle velocity $v_p$ is defined as:

$$\overline{\langle v_p\rangle^s}(x,z) = \frac{\Delta x \Delta z}{V_a}\int_y \overline{\gamma_p(x,y,z,t)v_p(x,y,z,t)}\,dy\,, \tag{7}$$

where the brackets denote the local volume average and the overline denotes the time or Reynolds average, $V_a = \Delta x \Delta z\, l_y$ is the averaging volume with, respectively, $\Delta x$ and $\Delta z$ the spanwise grid cell dimensions and $l_y$ the length of the pipe, and $\gamma_p \in [0,1]$ is the solid phase indicator function and measures the local solid volume fraction in a computational grid cell. Similarly, the mean macroscopic solid volume fraction is computed as:

$$\overline{\phi}(x,z) = \frac{\Delta x \Delta z}{V_a}\int_y \overline{\gamma_p(x,y,z,t)}\,dy\,. \tag{8}$$

The mean *intrinsic* or *phase-averaged* streamwise solid velocity is computed by dividing the mean superficial average by the mean concentration:

$$\overline{\langle v_p\rangle} = \frac{\overline{\langle v_p\rangle^s}}{\overline{\phi}}\,. \tag{9}$$

The mean intrinsic solid bulk velocity is computed from:

$$v_{bs} = \frac{\int_{A_{pipe}} \overline{\langle v_p\rangle^s}\,dA}{\int_{A_{pipe}} \overline{\phi}\,dA}\,, \tag{10}$$

where $A_{pipe}$ denotes the cross-sectional area of the pipe.

Consistent with Eq. (7), the mean superficial streamwise fluid velocity is defined as:

$$\overline{\langle v_f\rangle^s} = \frac{\Delta x \Delta z}{V_a}\int_y \overline{(1-\gamma_p)\,v_f}\,dy\,. \tag{11}$$

The corresponding mean intrinsic fluid velocity is defined as:

$$\overline{\langle v_f\rangle} = \frac{\overline{\langle v_f\rangle^s}}{1-\overline{\phi}}\,. \tag{12}$$

The total fluid stress in the fluid phase is denoted by $\boldsymbol{\sigma}_f$. Similarly, the total solid stress within the particles is denoted by $\boldsymbol{\sigma}_p$. Consistent with the definition of the modified pressure ($p$) in Section 2, the modified fluid and particle stresses are defined by, respectively:

$$\boldsymbol{\tau}_f = \boldsymbol{\sigma}_f + \left(\nabla p_e \cdot \mathbf{x}\right)\mathbf{I} + (\mathbf{g}\cdot\mathbf{x})\,\mathbf{I}\,, \tag{13a}$$

$$\boldsymbol{\tau}_p = \boldsymbol{\sigma}_p + \left(\nabla p_e \cdot \mathbf{x}\right)\mathbf{I} + (\mathbf{g}\cdot\mathbf{x})\,\mathbf{I}\,. \tag{13b}$$

At the surface of the particles it holds that $\boldsymbol{\sigma}_p \cdot \mathbf{n} = \boldsymbol{\sigma}_f \cdot \mathbf{n}$ and hence it also holds that $\boldsymbol{\tau}_p \cdot \mathbf{n} = \boldsymbol{\tau}_f \cdot \mathbf{n}$, where $\mathbf{n}$ is the surface unit normal.

Using Eqs. (13a) and (13b), the combined forces from stresses and gravity acting on the fluid and the solid phase can be written as, respectively:

$$\nabla\cdot\boldsymbol{\sigma}_f + \mathbf{g} = \nabla\cdot\boldsymbol{\tau}_f - \nabla p_e\,, \tag{14a}$$

$$\nabla\cdot\boldsymbol{\sigma}_p + (\rho_p/\rho_f)\mathbf{g} = \nabla\cdot\boldsymbol{\tau}_p - \nabla p_e + \left(\frac{\rho_p}{\rho_f} - 1\right)\mathbf{g}\,. \tag{14b}$$

From the definition of the superficial volume average it follows that:

$$\nabla\cdot\overline{\langle\boldsymbol{\tau}_f\rangle^s} = \frac{\Delta x\Delta z}{V_a}\int_y \overline{(1-\gamma_p)\nabla\cdot\boldsymbol{\tau}_f}\,dy + \frac{\Delta x\Delta z}{V_a}\int_y \overline{-\nabla\gamma_p\cdot\boldsymbol{\tau}_f}\,dy\,. \tag{15a}$$

The first term at the right-hand side is equal to $\overline{\langle\nabla\cdot\boldsymbol{\tau}_f\rangle^s}$. Since $\nabla\gamma_p = -\delta_d\mathbf{n}$ with $\mathbf{n}$ the outward surface unit normal and $\delta_d$ the Dirac delta function that peaks at the surface of the particles, the second term reduces to an integral of the stress over the solid/liquid interfaces within the averaging volume $V_a$. This term thus denotes the negative of the macroscopic drag force, $-\mathbf{f}_{p\to f}$, that the solid phase exerts on the fluid phase within $V_a$. Similarly, it holds that:

$$\nabla\cdot\overline{\langle\boldsymbol{\tau}_p\rangle^s} = \overline{\langle\nabla\cdot\boldsymbol{\tau}_p\rangle^s} + \mathbf{f}_{p\to f}\,, \tag{15b}$$

where we used that $\nabla\gamma_p\cdot\boldsymbol{\tau}_p = \nabla\gamma_p\cdot\boldsymbol{\tau}_f$ on the surface of the particles.

Using the above results, the mean superficial average of Eqs. (14a) and (14b) can be written as, respectively:

$$\overline{\langle\nabla\cdot\boldsymbol{\sigma}_f + \mathbf{g}\rangle^s} = \nabla\cdot\overline{\langle\boldsymbol{\tau}_f\rangle^s} + \mathbf{f}_{p\to f} - \overline{(1-\phi)\nabla p_e}\,, \tag{16a}$$

$$\overline{\langle\nabla\cdot\boldsymbol{\sigma}_p + (\rho_p/\rho_f)\mathbf{g}\rangle^s} = \nabla\cdot\overline{\boldsymbol{\Sigma}} - \mathbf{f}_{p\to f} - \overline{\phi\nabla p_e} + \overline{\phi}\left(\frac{\rho_p}{\rho_f} - 1\right)\mathbf{g}\,, \tag{16b}$$

where $\overline{\boldsymbol{\Sigma}} = \overline{\langle\boldsymbol{\tau}_p\rangle^s}$ is introduced here for ease of notation and will be simply referred to as the '(superficial) particle stress' in the sequel.

The mean superficial fluid stress can be worked out further in the following manner:

$$\overline{\langle\boldsymbol{\tau}_f\rangle^s} = -\overline{\langle p\rangle^s}\,\mathbf{I} + \left(\frac{1}{Re}\frac{D_{pipe}}{D_p}\right)\left(\nabla\overline{\langle\mathbf{u}_f\rangle^s} + \nabla\overline{\langle\mathbf{u}_f\rangle^s}^T\right) - \left(\frac{1}{Re}\frac{D_{pipe}}{D_p}\right)\left(\frac{\Delta x\Delta z}{V_a}\int_y \overline{(\nabla\gamma_f)\mathbf{u}_f}\,dy + \frac{\Delta x\Delta z}{V_a}\int_y \overline{(\nabla\gamma_f)\mathbf{u}_f}^T\,dy\right). \tag{17}$$

An expression for the integrals at the right-hand side can be found from considering the mean superficial average of (twice) the rate-of-strain in the solid phase:

$$\overline{\langle\nabla\mathbf{u}_p + \nabla\mathbf{u}_p^T\rangle^s} = \nabla\overline{\langle\mathbf{u}_p\rangle^s} + \nabla\overline{\langle\mathbf{u}_p\rangle^s}^T - \left(\frac{\Delta x\Delta z}{V_a}\int_y \overline{(\nabla\gamma_p)\mathbf{u}_p}\,dy + \frac{\Delta x\Delta z}{V_a}\int_y \overline{(\nabla\gamma_p)\mathbf{u}_p}^T\,dy\right). \tag{18}$$

For rigid particles, the left-hand side is zero. Furthermore, $(\nabla\gamma_p)\mathbf{u}_p = -(\nabla\gamma_f)\mathbf{u}_f$ at the surface of the particles. Using Eq. (18), the following result is obtained for the mean superficial fluid stress:

$$\overline{\langle\boldsymbol{\tau}_f\rangle^s} = -\overline{\langle p\rangle^s}\,\mathbf{I} + \left(\frac{1}{Re}\frac{D_{pipe}}{D_p}\right)\left(\nabla\overline{\mathbf{u}}_m + \nabla\overline{\mathbf{u}}_m^T\right), \tag{19}$$

where $\overline{\mathbf{u}}_m = \overline{\langle\mathbf{u}_f\rangle^s} + \overline{\langle\mathbf{u}_p\rangle^s}$ is the mean macroscopic mixture velocity.

Finally, the sum of Eqs. (16a) and (16b) represents the total macroscopic force on the mixture of fluid and particles from stresses and gravity:

$$\overline{\langle\nabla\cdot\boldsymbol{\sigma}_f + \mathbf{g}\rangle^s} + \overline{\langle\nabla\cdot\boldsymbol{\sigma}_p + (\rho_p/\rho_f)\mathbf{g}\rangle^s} = -\overline{\nabla p_e} - \nabla\overline{\langle p\rangle^s} + \left(\frac{1}{Re}\frac{D_{pipe}}{D_p}\right)\nabla^2\overline{\mathbf{u}}_m + \nabla\cdot\overline{\boldsymbol{\Sigma}} + \overline{\phi}\left(\frac{\rho_p}{\rho_f} - 1\right)\mathbf{g}\,, \tag{20}$$

where we used that $\nabla\cdot\overline{\mathbf{u}}_m = 0$ based on mass conservation for the mixture.

## 6. Comparison of experiments and DNS

### 6.1. Instantaneous flow snapshots

To facilitate a visual comparison, instantaneous snapshots from a side view of the slurry flow in the experiment (E1–E3) and DNS (D1–D3) are provided in Fig. 3 . In both the DNS and experiment, we observe an increase in the number of particles in suspension with increasing $Re$. Further, from the video recordings we observed a fixed (static) bed in E1 and a nearly fixed bed in D1, a sliding bed in E2 and D2, and a suspension of particles without clear presence of a bed in E3 and D3. In E1 and D1, we observe an ordered packing arrangement of particles within the bed at the pipe wall. This is also clearly visible in the sliding bed cases E2 and D2, where the packing structure is somewhat skewed due to bed sliding. The ordered packing at the wall originates from the kinematic condition that the particles cannot overlap with the wall. This effect is reinforced by the high degree of monodispersity of the spheres in the experiments and the perfect monodispersity in the DNS. In cases E3 and D3 all particles are suspended, but the distribution is clearly heterogeneous with more particles in the lower than the upper half of the pipe and moving at a lower velocity as well. Though the amount of particles in suspension and the bed height seems visually comparable between the experiments and corresponding DNS, it appears that there are more particles reaching the top of the pipe in cases E1 and E2 as compared to D1 and D2, respectively. The opposite holds for case E3 as compared to case D3.

For cases D1–D3, Fig. 4 presents snapshots of the streamwise fluid and solid velocity in two midplanes of the pipe, along with the 3D spatial particle distribution over part of the pipe. It is visually apparent that the flow is turbulent in the upper half of the pipe where the particle concentration is zero or low, while strongly damped in the region where the particle concentration is high. Normalized with the liquid bulk velocity, the highest peak fluid velocity is seen in D1. The immobile particles block the lower half of the pipe in D1 and hence the fluid is funneled through a smaller cross-sectional area in the upper half of the pipe. In contrast to D1, in D2 the bed of particles in the lower half of the pipe has a nonzero velocity. In D3, we observe a suspension of particles, with particles even at the top of the pipe, and there no longer appears to be a clear presence of a particle bed at the pipe bottom.

### 6.2. Mean streamwise pressure gradient

From the streamwise pressure gradient obtained from the DNS and experiments, the Darcy–Weisbach friction factor was computed according to:

$$f = -\frac{\overline{dp_e}}{dy}\frac{D_{pipe}}{\frac{1}{2}\rho_f v_{mix}^2}\,, \tag{21}$$

where here $\overline{dp_e/dy}$ is the *dimensional* mean pressure gradient, $v_{mix} = \phi_b v_{bs} + (1-\phi_b)v_{bl}$ is the bulk mixture velocity, and $\rho_f \approx 997.4$ kg/m$^3$ is the density of water at 23.5 °C in the experiments. Since $v_{mix}$ was not explicitly measured in the experiments, $v_{mix}$ from cases D1–D3 was used to determine the friction factor for cases E1–E3, respectively. In Fig. 5a the friction factor is plotted as function of the mixture Reynolds number defined as $Re_{mix} = v_{mix}D_{pipe}/\nu_f$. The DNS and experiment show good agreement for cases D3 and E3 ($Re_{mix} = 14164$), where the slurry flow is in the fully-suspended regime. However, the friction factor from the DNS underpredicts the experiment by −35% in case D1 compared to E1 and −21% in case D2 compared to E2 ($Re_{mix} = 7812$). The reason for this is not fully clear, but might be related to the uncertainty in

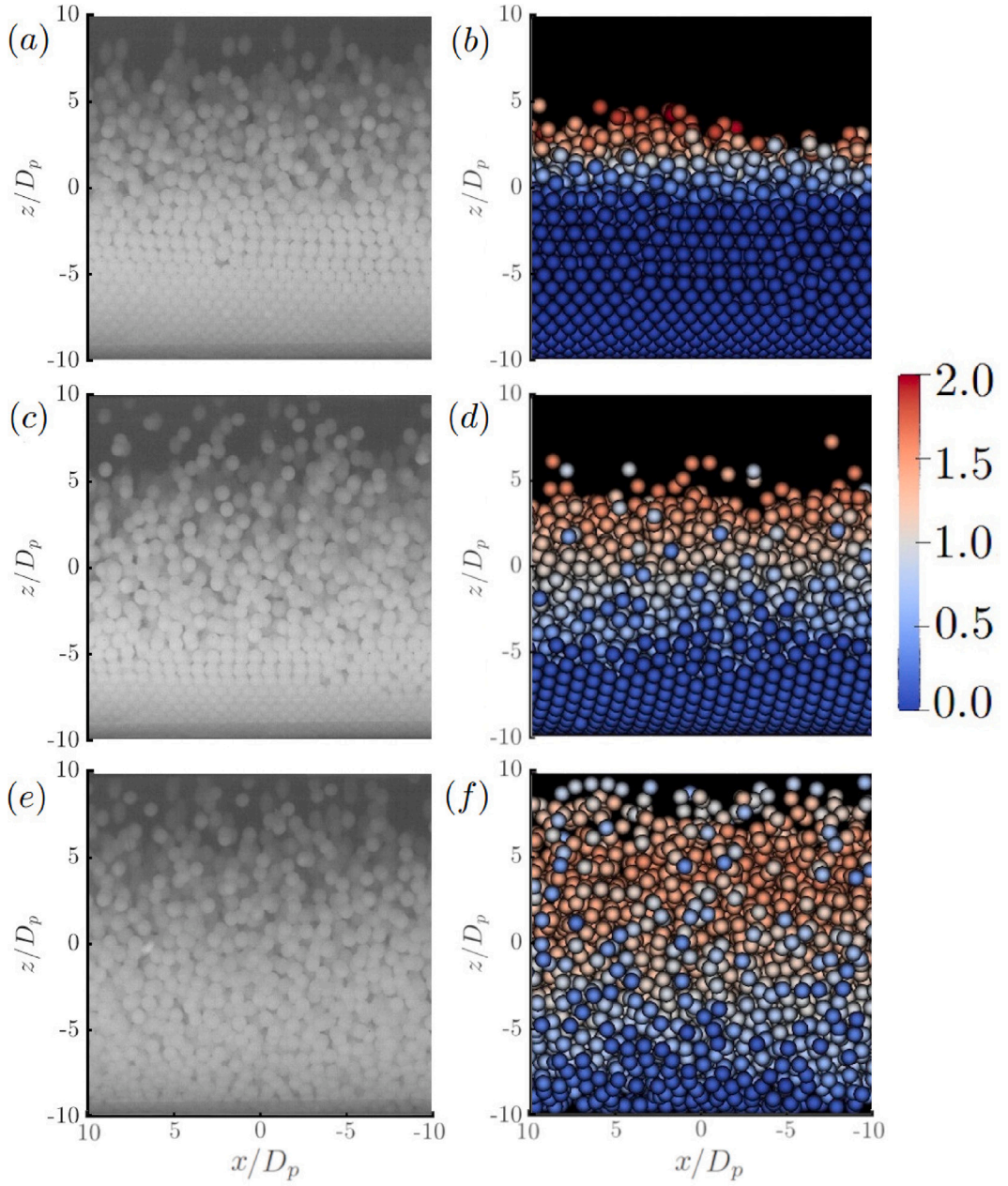


**Fig. 3.** Instantaneous snapshots of the spatial distribution and velocity of the particles in the experiment (left) and DNS (right). The particles in the DNS are colored by their streamwise velocity $v_p$ scaled with the fluid bulk velocity $v_{bl}$. Note that the snapshots provide a side view of the pipe along the $y$ direction. (a) E1, (b) D1, (c) E2, (d) D2, (e) E3 and (f) D3. (For interpretation of the references to color in this figure legend, the reader is referred to the web version of this article.)

the reconstructed liquid bulk velocity from the experiments, see the discussion in Section 3.

In Fig. 5a the DNS and experimental data are compared with a number of friction factor models, each developed for a *specific* flow regime, see Appendix D for details of the models. The model for the fixed-bed regime ($f_{FB}$) closely matches with the DNS for case D1, while strongly overpredicts the friction factor for cases D2/E2 and D3/E3 as may be expected since the flow is in a different regime. The original Durand and Condolios model ($f_{DC}$) (Durand and Condolios, 1953) strongly overpredicts the DNS and experimental data (see Table D.1, data points not shown in Fig. 5a), while the modified Durand and Condolios model ($f_{MDC}$) agrees very well with the sliding-bed case D2. This difference underlines the importance of using the *reduced gravity*, $(\rho_p/\rho_f - 1)|\tilde{\mathbf{g}}|$, in the friction factor model instead of *gravity*, $|\tilde{\mathbf{g}}|$, as suggested originally by Durand and Condolios, see Appendix D; this is especially relevant to our study where the density ratio is $\rho_p/\rho_f = 1.02$ and thus very different from the value of $\approx 2.65$ in the experiments of Durand and Condolios. The model of Newitt et al. (1955) for the sliding-bed regime ($f_{NSB}$) closely matches with the experiments for the sliding-bed case E2, while the model for the heterogeneous suspension regime ($f_{NHS}$) best matches with the experiments for the fully-suspended case E3. Finally, the equivalent liquid model ($f_{ELM}$) strongly underpredicts both the DNS and experiments as particles are rather large in our study and not homogeneously mixed across the pipe.

Fig. 5b depicts the Darcy–Weisbach friction factor, $f$, as function of the Shields number, $\theta$. As mentioned before, the Shields number is often used as a metric for the degree of particle entrainment into the flow and can thus be used to distinguish between the different regimes in slurry pipe flow. Fig. 5b shows that for cases S1–S4, in which only $Re$ was varied, $f$ drops off approximately as $f \approx 0.112/\theta$ for $\theta \lesssim 2$.

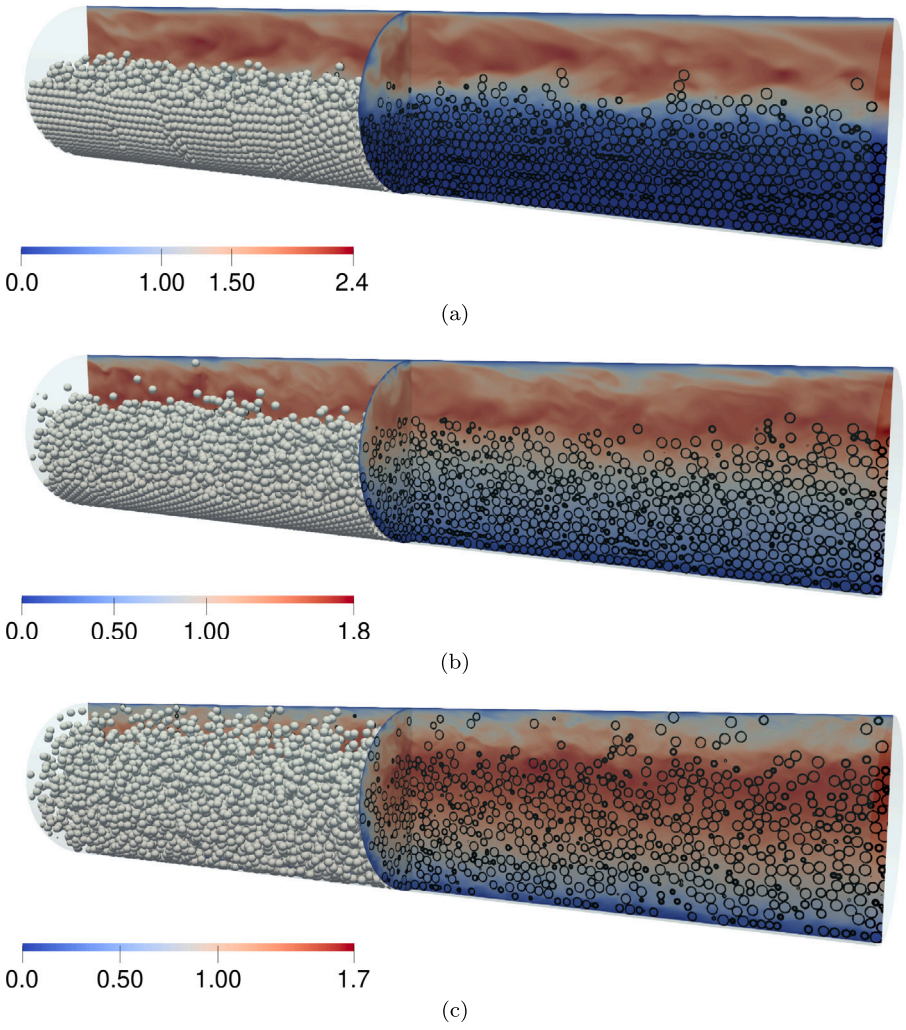


**Fig. 4.** Instantaneous flow snapshots from the DNS in an $xz$ and the $yz$ plane along the pipe axis. The flow is going from left to right. The color denotes the streamwise velocity normalized with the liquid bulk velocity. Contours indicate the particle positions (local grid cell solid volume fraction equal to 0.5). The 3D spatial particle distribution is shown for part of the pipe in gray color. (a) D1, (b) D2, and (c) D3. (For interpretation of the references to color in this figure legend, the reader is referred to the web version of this article.)

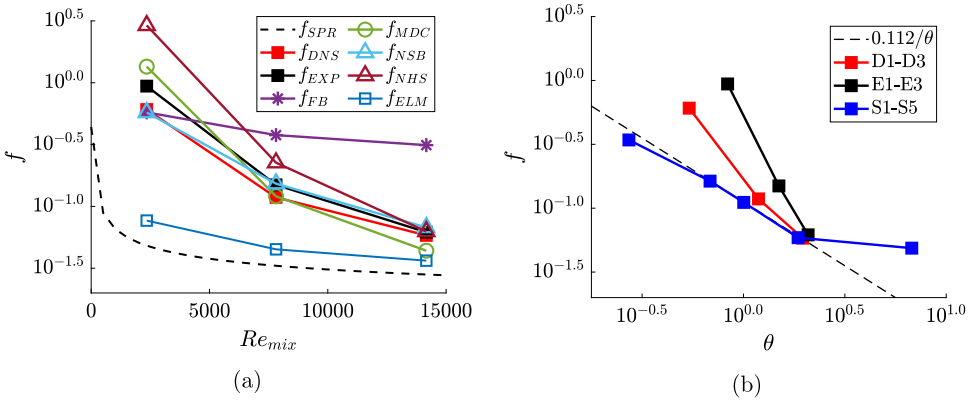


**Fig. 5.** (a) Darcy–Weisbach friction factor, $f$, as function of the bulk mixture Reynolds number, $Re_{mix}$. The red and black solid squares denote the data from the DNS (D1, D2 and D3) and experiments (E1, E2 and E3), respectively. Dashed line corresponds to the Haaland friction factor (Haaland, 1983) for single-phase flow in a smooth pipe, $f_{SPR}$. Remaining symbols correspond to correlations proposed in literature: $f_{FB}$ from a fixed-bed model D, $f_{MDC}$ a modified version of the Durand and Condolios model based on the use of the reduced gravity (Newitt et al., 1955), $f_{NSB}$ and $f_{NHS}$ from Newitt et al. (1955), and $f_{ELM}$ from the equivalent liquid model. (b) Darcy–Weisbach friction factor, $f$, as function of the Shields number $\theta$. The dashed lines corresponds to $f = 0.112/\theta$. (For interpretation of the references to color in this figure legend, the reader is referred to the web version of this article.)

In the range between $\theta \simeq 2$ and 6.76, corresponding to case S5, $f$ seems to level off and to become independent of $\theta$; in fact, $f$ is about three times larger for case S5 than predicted by the trend for cases S1–S4 for the smaller $\theta$−range. Note that for cases D1–D3 and E1–E3, $f$

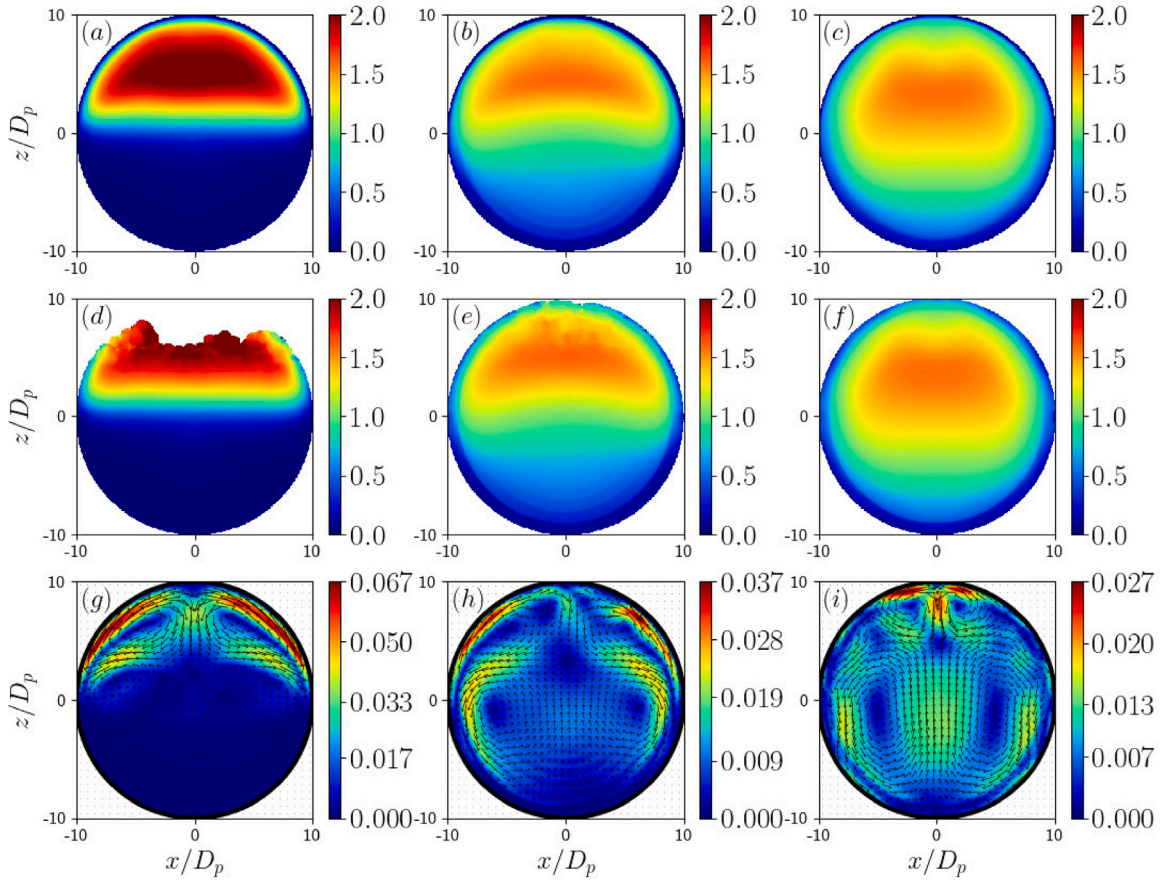


**Fig. 6.** Mean velocity distribution across the pipe obtained from the DNS. From left to right results are depicted for cases D1–D3. (a)–(c) Mean intrinsic liquid velocity, $\overline{\langle v_f \rangle}/v_{bl}$. (d)–(f) Mean intrinsic solid velocity, $\overline{\langle v_p \rangle}/v_{bl}$, where white indicates areas where particles are absent. (g)–(i) Mean secondary fluid flow, $\overline{\langle u_f \rangle}/v_{bl}$ and $\overline{\langle w_f \rangle}/v_{bl}$. The color denotes the secondary flow magnitude, $\sqrt{\overline{\langle u_f \rangle}^2 + \overline{\langle w_f \rangle}^2}/v_{bl}$, and the vectors indicate the flow direction. The reference vector length has been rescaled for every case to optimize visibility. (For interpretation of the references to color in this figure legend, the reader is referred to the web version of this article.)

decreases more steeply as $\theta$ increases and the results do not coincide onto a single curve, indicating that $f$ is also influenced by variations in $\phi_b$ and, though small, $Ga$.

From the definition of the friction factor it can be shown that:

$$f = 8\,\theta \left( \frac{Ga}{Re_{mix}} \frac{D_{pipe}}{D_p} \right)^2 . \tag{22}$$

Our results thus indicate that for cases S1–S4 and the constant values of $Ga$ and $D_{pipe}/D_p$ used, $\theta \approx Re_{mix}/6349$ and $f \approx 711/Re_{mix}$, and suggest that $\theta \sim Re_{mix}^2$ and $f$ constant for $\theta \gg 1$. The $f \sim 1/Re_{mix}$ behavior for cases S1–S4 is a rather surprising result as it reminds of the behavior of the friction factor for laminar single-phase flows ($f = 64/Re_{mix}$), while in these cases the slurry flow is clearly turbulent outside the bed and high particle concentration regions as will be shown later (see, e.g., Fig. 12). The reason for this is not fully clear yet, but must be related to the change in flow regimes from fixed to sliding bed and to the suspended regime with increasing $Re_{mix}$ and $\theta$, which is associated with significant changes in the flow pattern and the amount of sediment carried by the flow. Finally, the constant friction factor for very high $\theta$ is intuitively expected based on the constant friction factor of a turbulent single-phase flow in a hydraulically rough pipe (Pope, 2000).

### 6.3. Mean velocity profile

For the DNS cases D1–D3, Fig. 6 shows the mean velocity in the cross-flow plane. The top, middle and bottom row depict, respectively, the mean streamwise fluid velocity, $\overline{\langle v_f \rangle}$, the mean streamwise particle velocity, $\overline{\langle v_p \rangle}$, and the mean secondary fluid flow, $\overline{\langle u_f \rangle}$ and $\overline{\langle w_f \rangle}$. The streamwise fluid and particle velocity distributions appear nearly the same, a first indication that macroscopic particle/fluid slip in the mean streamwise velocity is generally small. In all cases, but especially in case D1, the bulk flow happens through the top half of the pipe.

In all cases a clear secondary flow of Prandtl's second kind is present. Relative to the liquid bulk velocity, the magnitude of the secondary flow is strongest in case D1 and weakest in case D3, with maximum values on the order of 7% and 3%, respectively. The high maximum value for case D1 is significantly higher than the maximum value of around 3% found for turbulent single-phase flows in semi-circular pipes in previous studies (Larsson et al., 2011; Liu et al., 2023). This may be partially explained by our normalization with the liquid bulk velocity based on the entire pipe cross-section, while for case D1 the liquid bulk velocity would be roughly twice as large when it would based on the upper half of the pipe only.

In case D1, the secondary flow is characterized by two counter-rotating recirculation cells that stretch over the entire flow region above the bed and which are responsible for a significant downflow underneath the top of the pipe. The resemblance of the recirculation cells with the secondary flow structure found for turbulent single-phase flows in semi-circular pipes, suggests a similar origin from centrifugal forces acting on curved paths of fluctuating fluid motions near the corners (Nikitin et al., 2021). However, in case D1, only two main recirculation cells are present (one cell near each corner), contrary to two counter-rotating recirculation cell *pairs* (one pair near each corner) found for turbulent single-phase flows in semi-circular pipes (Larsson

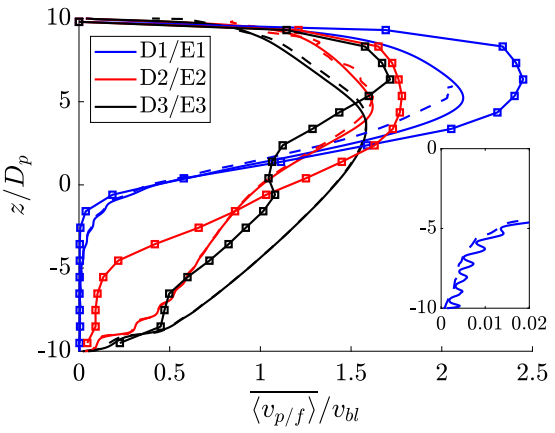


**Fig. 7.** Mean streamwise velocity profile as function of height shown for the DNS (D1–D3) and experiments (E1–E3). The profiles from the DNS were taken from the streamwise-vertical midplane, while the experimental profiles represent the mean streamwise particle velocity as function of height *along the pipe wall in the side view of the pipe*. Solid lines with square symbols: experimental data for the mean streamwise particle velocity. Solid and dashed lines: DNS profiles for mean streamwise fluid and particle velocity. In case D1, the particle velocity profile reaches to $z/D_p \approx 6$ as beyond that height no particles are present in the flow. The inset shows an enlarged view of the bottom half of the pipe for case D1.

et al., 2011; Liu et al., 2023). We ascribe this difference to the presence of a dense particle layer above the stationary bed in case D1 (cf. Figs. 6g and 8d), and the associated damping of secondary flow by the particle stress (related to drag and a locally high suspension viscosity). Furthermore, for case D1, the secondary flow is negligible inside the stationary sediment bed, presumably because of viscous drag which tends to damp any spatial inhomogeneity of the flow within the bed.

In case D2, the secondary flow is characterized by two main counter-rotating vortex pairs. The upper vortices bear a clear resemblance to the main vortices in case D1. This suggests that they are dynamically similar and thus caused by turbulent fluctuating motions in the apparent presence of internal flow corners. Different from case D1, a lower vortex pair is present that extends over the entire lower half of the pipe, including the sliding-bed region. Within the bed, both drag and the high suspension viscosity are likely responsible for damping of the secondary flow. A relatively strong downward secondary flow is present in the low-concentration regions flanking the sliding bed, which might be caused by turbulent fluctuations in a 'corner-like' geometry and is possibly amplified by particle-stress gradients (Kazerooni et al., 2017; Fornari et al., 2018; Lin et al., 2017b) and local particle sedimentation (Lin et al., 2017a). The secondary flow pattern in case D2 exhibits a 'saddle' point at $x \approx 0$ and $z \approx 3D_p$, which is accompanied by a smooth 'dimple' in the streamwise fluid and particle velocity distributions in Figs. 6b and 6e, respectively. This suggests a mutual coupling between the mean streamwise and the mean secondary flow.

As in case D2, the secondary flow in case D3 is characterized by two main vortex pairs. Compared to case D2, in case D3 the upper, corner-induced, vortices are confined to a smaller region below the top of the pipe, which can be explained from the significantly higher elevation to which particles are suspended in this case (cf. Figs. 8e and 8f). The lower vortex pair extends over the entire lower half of the pipe. A fairly strong upward secondary flow is visible inside the dense particle core (cf. Figs. 6i and 8f), which contributes to the lifting of the particle core. The resemblance of the lower vortex pair in case D3 to the lower vortex pair in case D2, strongly suggests that they are dynamically similar and originate from similar physical mechanisms. Distinction should be made here between the primarily downward secondary flow inside the low-concentration zones flanking the particle core, of which the physical mechanism was discussed above, and the primarily upward flow inside the dense particle core. After the study of Kazerooni et al. (2017) and based on the observation from Fig. 4c that turbulence is strongly damped inside the dense particle core, it is likely that spatial variations in the particle stresses are responsible for generating and maintaining the secondary flow inside the dense particle core. We hypothesize that this can be conceptually related to centrifugal forces acting on curved paths of fluctuating particle motions, similar to the mechanism by which secondary flow is generated in turbulent single-phase flow over longitudinal corners, ridges and riblets (Nikitin et al., 2021). The fluctuating particle motions arise from interactions of adjacent particle layers under shear. For non-axisymmetric mean particle concentration and particle velocity distributions, the centrifugal forces from fluctuating particle motions are on statistical average responsible for mean particle-stress gradients that drive the secondary flow. We speculate that the 'wedge-shaped' high-concentration zone above the bottom of the pipe in cases D2 and D3 as observed from Fig. 8, might act as an apparent ridge to the particles around it and drives the particles along the wedge upwards.

Fig. 7 shows mean streamwise fluid and particle velocity profiles as function of height obtained from both the DNS and experiments. While the DNS profiles were obtained from the streamwise-vertical midplane, the experimental profiles were reconstructed based on the camera recordings from a side view of the flow, see Appendix B, and thus represent the mean particle velocity as function of height *along the pipe wall in the side view of the pipe*. Nonetheless, since Fig. 6 shows that the mean streamwise particle velocity is rather homogeneous in $x$, the bias from the different way in which the experimental and DNS profiles were obtained, is deemed to be small.

In general, the DNS and experimental profiles show reasonable agreement, especially when the uncertainty in the estimation of the bulk velocity from the experimental data is taken into account as discussed in Section 3. For the fixed-bed cases D1 and E1, the velocity within the bed region is close to zero. While in the experiment the bed is not moving at all, as observed from the high-speed camera recordings (cf. Fig. 3a), in the DNS the bed has a slight mean velocity of $\mathcal{O}(5 \cdot 10^{-3}\, v_{bl})$, see the inset in Fig. 7. Another striking observation is that the peak velocity at $z/D_p \approx 5-6$ is roughly 20% higher in the experiment than in the DNS. This might indicate that the actual bulk velocity in the experiment has been somewhat higher than we have estimated; this is also consistent with the higher friction factor for the experiment than for the DNS. In E2 and D2, we observe a non-stationary bed in both experiment and DNS. In the experiment, we observe a nearly constant velocity in the bed indicating that the bed moves as a single unit. However, in the DNS we observe a gradual increase in the velocity of the bed with increasing height, indicating a pronounced downward momentum transfer by shearing motion between adjacent particle layers within the sliding bed. Furthermore, the DNS underpredicts the peak velocity at $z/D_p \approx 5$ by roughly 10% as compared to the experiment. In the fixed and sliding-bed cases, we observe a distinct change in the slope of the velocity profile demarcating a diffuse interface between the bed of particles and the overlying fluid. This is not observed in E3 and D3 where a bed is absent, likely due to shear-induced migration of particles into the flow.

Finally, we note that the DNS results show that the mean streamwise particle and fluid velocity profiles are nearly identical over the entire height for all cases; small deviations are observed only for the top half of the pipe. The small macroscopic slip can be understood from a consideration of the particle Stokes number, $St = t_p/t_f$, where $t_p = (\rho_p/\rho_f + 1/2)\, D_p^2/(18\nu_f)$ is the viscous particle response time to changes in the flow (Balachandar and Eaton, 2010) with the factor $1/2$ accounting for the added mass of an unsteady sphere in free space (Brennen, 2005), and $t_f = R_{pipe}/v_\tau$ (Pope, 2000) is a typical time scale for the large turbulent eddies in the bulk fluid. For cases D1–D3, $St$ is in the range of 0.02–0.05 and thus much smaller than

one, indicating that the particles tend to follow the large-scale fluid motions and explaining the small slip.

### 6.4. Mean concentration

In Fig. 8, we present the mean concentration distribution, $\overline{\phi}(x, z)$, in the cross-flow plane of the pipe for both the experiments and corresponding DNS. To ease the comparison of the different flow regimes, the concentration is normalized with the bulk concentration $\phi_b$. The mean concentration distributions are qualitatively similar for the experiments and the corresponding DNS. For all cases the 2D mean concentration distribution appears intimately connected to the mean secondary flow pattern (cf. Figs. 8d–f and 6g–i). In the fixed-bed cases E1 and D1, the bed interface is flat and centered around $z = 0$. In case D1 we clearly observe a layered arrangement of the particles in concentric rings. This originates from the constraint that the perfectly monodisperse particles cannot overlap with the wall and tend to align parallel to the wall, as observed before from the flow snapshots shown in Fig. 3. This effect is likely also present in the experiment, though probably less pronounced as in the DNS due to a lesser degree of monodispersity. It is probably because of insufficient spatial resolution that the layering is not captured by the ERT sensor (cf. Figs. 8a and 3a).

In the sliding-bed cases E2 and D2, the bed interface is curved with the highest position of the interface in the middle. Highest concentrations are found in a 'wedge-shaped' zone in the lower circle quadrant centered around $x = 0$. Particle layering is visible in the DNS result, but mostly confined to this lower quadrant. Particle transport and drag from secondary flow likely contributed to the peculiar bed shape and solid volume distribution within the bed, cf. Figs. 6h and 8e.

In case E3 the particles are lifted upwards with respect to case E2. In the corresponding DNS case D3, the particles are lifted significantly higher than in E3 though. The lifted particle core in case D3 has a nearly uniform concentration with the absence of layering. Interestingly, two particle layers can still be observed near the bottom of the pipe, with a distinct fluid gap in between with a strongly reduced concentration. We attribute the origin of the lifted dense particle core and pronounced particle–wall layer to shear-induced migration (Leighton and Acrivos, 1987; Lashgari et al., 2014, 2016) and a combined effect of gravity and particle lubrication at the pipe wall (Lashgari et al., 2016), respectively. The upward migration of the particles is associated with repulsive forces of lubricated and collisional contacts of adjacent particle layers in relative motion due to shear. The repulsive forces from particle–particle interactions already exist for suspensions in Stokes flow (Leighton and Acrivos, 1987), but are amplified in the inertial regime due to particle inertia, a phenomenon dubbed as 'inertial shear thickening' by Picano et al. (2013) (see also Fig. 3 and related discussion in Lashgari et al. (2016)). From a continuum perspective, the repulsive forces are associated with a wall-normal gradient in the wall-normal particle stress (Guazzelli and Pouliquen, 2018). The particle stress is higher for increasing shear rate and increasing concentration. Consequently, the repulsive forces between adjacent particle layers act such that particles tend to accumulate in low-shear regions. Since the secondary flow pattern closely matches with the particle concentration pattern, transport by secondary flow and viscous drag inside the particle core might also contribute to maintaining the shape and lifting of the particle core.

We hypothesize that shear-induced particle migration is also responsible for the low-concentration zones flanking the sliding bed for $z/D_p \approx -4$ till 0 in case D2. With increasing shear rate, shear-induced migration becomes stronger and the low-concentration zones will extend further downwards along the pipe wall until the whole bed is lifted from the wall (which has nearly happened in case D3). This suggests that the angle of the wedge-shaped high-concentration zone at the pipe bottom might be set by a balance between the force from shear-induced particle migration directed upwards along the wedge edge and the component of the net gravity force on the particles directed downwards along the wedge edge. Within the sliding bed but outside the high-concentration zone at the pipe bottom, shear-induced migration is responsible for an apparent 'fluidization' of the bed at a significantly lower concentration than of the bed packing in the high-concentration zone.

In Fig. 9 the mean concentration profiles from the experiments and corresponding DNS are shown in the streamwise-vertical midplane (i.e., at $x = 0$). Furthermore, a moving-mean filter of one particle diameter width is applied to the DNS data to approximately match the resolution of the ERT sensor. For cases D1/E1 and D2/E2 the profiles are in good quantitative agreement. However, as already noticed from Fig. 8, the agreement for cases D3 and E3 is not as good, with particles being mixed higher up in the pipe and with a lower concentration in the particle plug in case D3.

The 2D mean concentration distributions of cases D2 and D3 bear a striking resemblance to the concentration distributions shown by Zhang et al. (2021a) (their figure 3) for horizontal gas–solid pipe flow in the so-called gravity-dominant and the particle-inertia-dominant regime, respectively. However, particle layering seems absent in their simulations, probably because of the much lower solid bulk concentrations considered, which was varied in the range of $\phi_b = 5.3 \cdot 10^{-5}$ to $1.1 \cdot 10^{-3}$, and the absence of particle–wall lubrication. Zhang et al. (2021a) hypothesized that the wedge-shaped concentration distribution in the gravity-dominated regime is caused by a secondary flow pattern, although not analyzed in further detail. This hypothesis is substantiated by the mean secondary flow pattern found for our case D2, see Fig. 6, indeed showing two circulation cells centered around the wedge-shaped high-concentration zone at the bottom of the pipe. As discussed before, we speculate that the wedge-shaped high-concentration zone might also act as an apparent ridge, which, in the presence of mean shear, drives a flow of particles along the ridge upwards. Furthermore, Zhang et al. postulated that the lifted particle core in the particle-inertia dominant regime originated from a Saffman lift force acting on the particles (Saffman, 1965; McLaughlin, 1991), but without evaluating the requirements for the presence of this force. As the bulk solid volume fractions in our study are much higher, particle–particle interactions will dominate over particle-fluid interactions in the highly concentrated regions of the flow. Therefore, we deem it more likely that the lifted particle core in case D3 originated from shear-induced migration from particle–particle interactions as discussed before.

Interestingly, the presence of a lifted particle core was reported in a few other studies in literature, with different speculations about its origin. Campbell et al. (2004) found experimental evidence of a lifted particle core in slurry flow through a rectangular channel. They speculated that it arose from multi-particle interactions, more specifically an attraction between particles from a 'Bernoulli interaction' in the presence of large particle-liquid slip. However, macroscopic particle-fluid slip is generally small in our simulations, see the collapse of the particle and fluid velocity profiles in Fig. 7, especially for case D3 with a lifted particle core. Wilson and Sellgren (2003) attributed the presence of a lifted particle core to Kutta–Joukowski lift acting on particles with a size larger than the viscous sublayer, though it is questionable to apply results from potential flow theory to slurry flows, in particular in the presence of turbulence. Kaushal and Tomita (2007) found evidence of a lifted particle core in $\gamma$-ray densitometer measurements, especially for coarser particles at higher concentrations and higher velocities. This was ascribed to a lift force related to the 'impact of the viscous-turbulent interface' on the bottom-most particle layer and a possible additional effect from particle–particle interactions. Furthermore, Kaushal and Tomita (2007) observed particle lift in CFD/TFM simulations and related this to lift from particle-fluid slip near the pipe wall. However, the simulated concentration profiles differed significantly from their $\gamma$-ray densitometer measurements and the 2D concentration distributions appear quite different from our

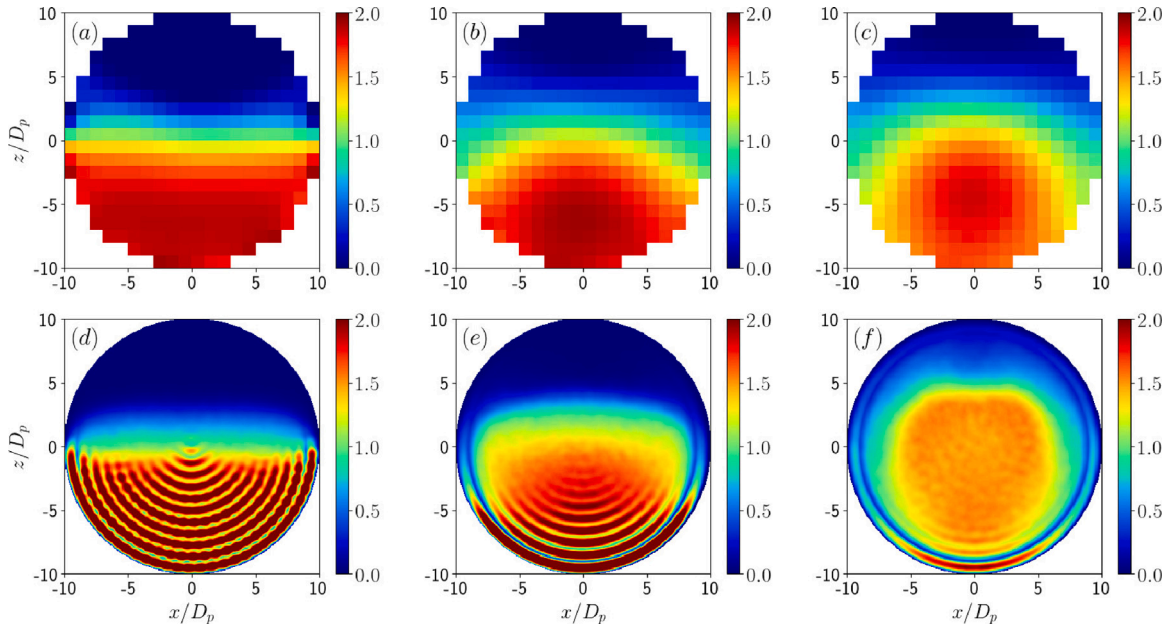


**Fig. 8.** Normalized mean concentration distribution, $\overline{\phi}(x,z)/\phi_b$, in the cross-flow plane of the pipe. (a)–(c) Experimental cases E1–E3. (d)–(f) Corresponding DNS cases D1–D3.

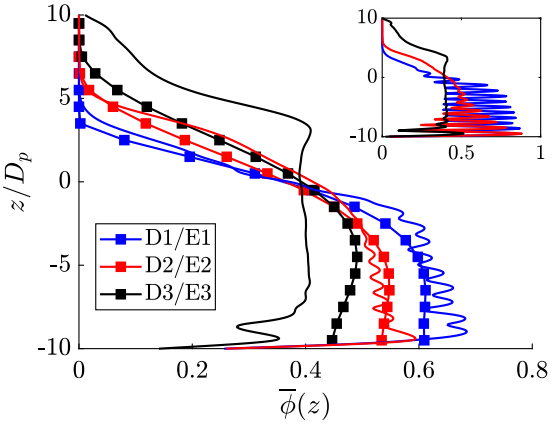


**Fig. 9.** Mean concentration profile as function of height in the streamwise-vertical midplane, shown for the DNS (D1–D3, solid lines) and the experiments (E1–E3, solid lines with square symbols). A moving mean filter of 1 particle diameter was applied to the DNS profiles for the sake of comparison with the ERT data. The inset shows the unfiltered concentration profiles from the DNS.

observation for case D3. Again, we consider it more plausible that shear-induced migration from particle–particle interactions has been responsible for the lifted particle core in our experiments and simulations, since turbulence near the bottom of the pipe is strongly suppressed by the high particle concentration.

Finally, Zhang et al. (2021a) mentioned that the degree of non-axisymmetry of the 2D mean concentration distribution or the 'gravity bias', is primarily controlled by the Froude number, which they defined as $v_{bl}/\sqrt{|\tilde{\mathbf{g}}|D_{pipe}}$. For comparison with the present study on liquid–solid pipe flow, the densimetric Froude number ($Fr$) is more relevant as it is based on the reduced gravity instead of gravity itself, see our previous discussion in Section 6.2. Using $\rho_p/\rho_f = 1000$ and $v_{mix} \approx v_{bl}$, the densimetric Froude number varied in the range of 0.27–1.08 in the simulations of Zhang et al. while $Fr = 0.60$, 2.00 and 3.67 in our cases D1, D2 and D3, respectively. The densimetric Froude numbers are thus having a similar order of magnitude, although we observe a fixed-bed regime for case D1 with $Fr = 0.60$ while this regime is not observed at all in the simulations of Zhang et al. As an alternative to the densimetric Froude number, the Shields number may be considered for comparison, but no information is provided on the values of the wall friction velocity in the study by Zhang et al. Instead, we compare the particle-based densimetric Froude number, defined here as $Fr_p = v_{mix}/\sqrt{(\rho_p/\rho_f - 1)|\tilde{\mathbf{g}}|D_p} = \sqrt{8\theta/f}$. In the simulations by Zhang et al. $Fr_p$ is in the range of 5.7–22.8, while $Fr_p = 2.7$, 8.9 and 16.4 in our cases D1, D2 and D3, respectively. The match between the particle-based densimetric Froude numbers is closer than for the pipe-diameter-based densimetric Froude number; the low value of $Fr_p$ for case D1 may explain why no fixed-bed regime is observed in Zhang et al. The above comparison suggests that the particle-based densimetric Froude number and likely also the Shields number are better metrics to distinguish between the different flow regimes than the pipe-diameter-based densimetric Froude number.

### 6.5. Mean streamwise momentum balance

To gain insight in the dynamics of the mean flow and thus mechanisms behind pipe friction, pressure drop and energy loss, we applied spatial and Reynolds averaging to the governing equations in order to derive an equation for the mean streamwise ($y$) momentum balance of the mixture flow (Batchelor, 1970; Guazzelli and Morris, 2011; Picano et al., 2015), see also the partial derivation in Section 5:

$$-\frac{\overline{dp_e}}{dy} + T + D + R = 0\,, \tag{23a}$$

$$T = \left(-\frac{\partial}{\partial x}\langle\overline{v_f u_f}\rangle^s - \frac{\partial}{\partial z}\langle\overline{v_f w_f}\rangle^s\right) + \frac{\rho_p}{\rho_f}\left(-\frac{\partial}{\partial x}\langle\overline{v_p u_p}\rangle^s - \frac{\partial}{\partial z}\langle\overline{v_p w_p}\rangle^s\right), \tag{23b}$$

$$D = \frac{1}{Re\,(D_p/D_{pipe})}\left(\frac{\partial^2\overline{v}_m}{\partial x^2} + \frac{\partial^2\overline{v}_m}{\partial z^2}\right), \tag{23c}$$

$$R = \frac{\partial\overline{\Sigma}_{yx}}{\partial x} + \frac{\partial\overline{\Sigma}_{yz}}{\partial z}\,, \tag{23d}$$

where we made use of the statistical properties of the flow (statistically steady and homogeneous in $y$), $T$ represents the momentum transport by fluid and particle motions, $D$ accounts for viscous diffusion with $\overline{v}_m = \overline{\langle v_f\rangle^s} + \overline{\langle v_p\rangle^s}$ the mixture velocity, and $R$ is the momentum

transport by superficial particle stresses, $\overline{\Sigma}_{yx}$ and $\overline{\Sigma}_{yz}$, related to the hydrodynamic particle stresslet and particle collisions/contacts (Guazzelli and Morris, 2011). The latter was not computed explicitly, but implicitly from $R = -(-\overline{dp_e/dy} + T + D)$, i.e., by using Eq. (23a).

The flow-induced momentum transport, Eq. (23b), is further decomposed into separate contributions from (a) the mean secondary flow and (b) turbulent fluctuations. To this purpose, we decomposed the momentum fluxes in Eq. (23b) according to:

$$\langle\overline{v_f u_f}\rangle^s = \langle\overline{v}_f\overline{u}_f\rangle^s + \langle\overline{v'_f u'_f}\rangle^s . \tag{24a}$$

Following Breugem and Boersma (2005) (p. 10,11), the first term at the right-hand side can be further decomposed according to:

$$\langle\overline{v}_f\overline{u}_f\rangle^s \approx \frac{\langle\overline{v}_f\rangle^s\langle\overline{u}_f\rangle^s}{1-\overline{\phi}} + \langle\widetilde{\overline{v}}_f\widetilde{\overline{u}}_f\rangle^s , \tag{24b}$$

where the approximation holds under sufficient scale separation between the macroscopic and the subfilter-scale flow, and the second term at the right-hand side denotes the subfilter-scale contribution to the momentum flux from the mean secondary flow with $\widetilde{\overline{v}}_f = \overline{v}_f - \langle\overline{v}_f\rangle$ and $\widetilde{\overline{u}}_f = \overline{u}_f - \langle\overline{u}_f\rangle$. We can thus make the following decomposition:

$$\langle\overline{v_f u_f}\rangle^s \approx \frac{\langle\overline{v}_f\rangle^s\langle\overline{u}_f\rangle^s}{1-\overline{\phi}} + \langle\widetilde{\overline{v}}_f\widetilde{\overline{u}}_f\rangle^s + \langle\overline{v'_f u'_f}\rangle^s . \tag{24c}$$

The above decomposition inspired us to rewrite the flow-induced momentum transport, $T$, into the contributions from the macroscopic mean secondary flow, $T_S$, and from subfilter-scale mean secondary flow and turbulent motions, $T_F$, according to:

$$T = T_S + T_F , \tag{25a}$$

$$\begin{aligned} T_S = &\left(-\frac{\partial}{\partial x}\left[\frac{\langle\overline{v}_f\rangle^s\langle\overline{u}_f\rangle^s}{1-\overline{\phi}}\right] - \frac{\partial}{\partial z}\left[\frac{\langle\overline{v}_f\rangle^s\langle\overline{w}_f\rangle^s}{1-\overline{\phi}}\right]\right) \\ &+ \frac{\rho_p}{\rho_f}\left(-\frac{\partial}{\partial x}\left[\frac{\langle\overline{v}_p\rangle^s\langle\overline{u}_p\rangle^s}{\overline{\phi}}\right] - \frac{\partial}{\partial z}\left[\frac{\langle\overline{v}_p\rangle^s\langle\overline{w}_p\rangle^s}{\overline{\phi}}\right]\right), \end{aligned} \tag{25b}$$

$$\begin{aligned} T_F = &\left(-\frac{\partial}{\partial x}\left[\langle\overline{v_f u_f}\rangle^s - \frac{\langle\overline{v}_f\rangle^s\langle\overline{u}_f\rangle^s}{1-\overline{\phi}}\right] - \frac{\partial}{\partial z}\left[\langle\overline{v_f w_f}\rangle^s - \frac{\langle\overline{v}_f\rangle^s\langle\overline{w}_f\rangle^s}{1-\overline{\phi}}\right]\right) \\ &+ \frac{\rho_p}{\rho_f}\left(-\frac{\partial}{\partial x}\left[\langle\overline{v_p u_p}\rangle^s - \frac{\langle\overline{v}_p\rangle^s\langle\overline{u}_p\rangle^s}{\overline{\phi}}\right] - \frac{\partial}{\partial z}\left[\langle\overline{v_p w_p}\rangle^s - \frac{\langle\overline{v}_p\rangle^s\langle\overline{w}_p\rangle^s}{\overline{\phi}}\right]\right). \end{aligned} \tag{25c}$$

Since the typical length scale of the secondary flow patterns is on the order of the pipe radius and since the dimensions of the averaging volume used to compute the macroscopic stresses, are equal to one grid cell in the cross-stream directions, the contribution of the subfilter-scale secondary flow to $T_F$ is likely negligible compared to the Reynolds stress contribution from turbulent motions.

The contributions from the four terms in Eq. (23) are shown in Fig. 10 as function of height for the streamwise-vertical midplane for the DNS cases D1–D3, along with the separate contributions from the mean secondary flow ($T_S$) and turbulent motions ($T_F$) to the flow-induced transport.

Focusing first on the fixed-case D1, we observe that inside the bed the streamwise pressure gradient is balanced by the particle-stress term. In fact, this is consistent with Darcy's law (Breugem et al., 2006), as the particle-stress term should counterbalance the drag force within the bed (no net force on the particles):

$$0 = -\overline{\frac{dp_e}{dy}} - \frac{1}{Re\,(D_p/D_{pipe})}\frac{D_p^2}{\kappa}(1-\overline{\phi})\left[\overline{\langle v_f\rangle} - \overline{\langle v_p\rangle}\right], \tag{26}$$

where $\kappa$ is the bed permeability. Estimating $\left[\overline{\langle v_f\rangle} - \overline{\langle v_p\rangle}\right]/v_{bl} \approx 0.0025$ from Fig. 7, the bed concentration $\overline{\phi} \approx 0.62$ from Fig. 9, and $-\overline{dp_e/dy} \approx 0.007$ (in units of $\rho_f v_{bl}^2/D_p$) from Fig. 10a, we find that $\kappa/D_p^2 \approx 8.3\times 10^{-4}$. This is comparable to the prediction from the modified Ergun equation (Macdonald et al., 1979) with an uncertainty of ±50% for a random packed bed, $\kappa/D_p^2 = (1/180)(1-\overline{\phi})^3/\overline{\phi}^2 \approx 7.9\times 10^{-4}$.

The particle-stress term in case D1 exhibits oscillations, which are accompanied with opposite oscillations in the diffusion term. This is a footprint of particle layering (cf. the insets of Figs. 7 and 9). In the top half of the pipe, the particle-stress term rapidly declines to zero and the flow-induced transport term becomes the dominant loss term, as may be expected for a turbulent flow and the absence of particles in this region. Interestingly, from Fig. 10b we observe that the contributions from secondary flow and turbulent motions to the overall flow-induced transport have the same order of magnitude and often have opposite sign, which seem typical features of secondary flows of Prandtl's second kind (Nikitin et al., 2021). For the range of $z/D_p \approx 6-9$, the transport by secondary flow is the dominant contribution, being responsible for downward transport of low-momentum fluid from the region near the pipe top (cf. Fig. 6g), hence the negative sign of the transport term. For the range of $z/D_p \approx -1$ till 5, transport by turbulent motions is responsible for downward transport of high-momentum fluid towards the bed interface, consistent with the swap in sign of the transport term at $z/D_p \approx 2$. Close to the top wall, the overall flow-induced transport term in Fig. 10a swaps sign and becomes zero at the wall since there can be no transport across the wall. Furthermore, a thin viscous wall layer is present where viscous diffusion is the dominant loss term of momentum.

The momentum balance for case D2 is comparable to case D1. The particle-stress term is not only the dominant loss term inside the sliding bed ($z \lesssim 0$), but also in the dense suspension layer above the bed till $z/D_p \approx 3$ (cf. Fig. 8e). Oscillatory behavior in the particle-stress term is only significant close to pipe bottom, where particle layering is present. Fig. 10d shows that turbulence in the streamwise-vertical midplane is confined to the region $z/D_p \gtrsim 3$, indicating that turbulent motions are strongly suppressed in the dense suspension layer above the sliding bed.

In case D3, the particle-stress term is only dominant in the region close to pipe bottom due to particle layering and in a small region centered around $z/D_p \approx 3$. The latter corresponds approximately to the top of the lifted particle core (Fig. 8f), which is characterized by a rapid decline in the particle concentration with increasing height and a local mean velocity maximum (Fig. 7). The flow-induced transport term is negative over most part of the streamwise-vertical midplane except near the pipe top and bottom and in a small region around the top of the lifted particle core at $z/D_p \approx 3$ where it is zero. Fig. 10f shows that this coincides with a transition from downward momentum transport by turbulent motions in the region directly above the lifted particle core to upward transport of low-momentum fluid by secondary flow within the particle core. Furthermore, within the lifted particle core, the zero turbulent transport indicates that turbulence is strongly suppressed. Interestingly, the transport from secondary flow is dominant over the particle-stress term in the bulk part of the lifted particle core ($z/D_p \approx -7$ till 0). This suggests that the upward directed secondary flow in the particle core likely contributes to the homogeneous concentration profile observed over the same region in Fig. 9 and acts in concert with shear-induced particle migration to counteract gravity.

To gain additional insight in the contributions of the secondary flow and turbulence to streamwise momentum transport, Fig. 11 depicts the spatial distributions of $T$, $T_S$ and $T_F$ in the cross-flow plane. As observed before for the streamwise-vertical midplane, $T_S$ and $T_F$ have a similar magnitude and often opposite sign. The contribution from turbulent motions, $T_F$, is confined to the areas with comparatively low particle concentration. It is typically negative inside these areas, but flips sign and becomes positive near the pipe wall and near the bed interface for case D1, indicating turbulent transport of streamwise momentum down the mean velocity gradient. The transport by secondary flow clearly bears the imprint of the secondary flow pattern. In case D1, this is responsible for transport of high-momentum fluid towards

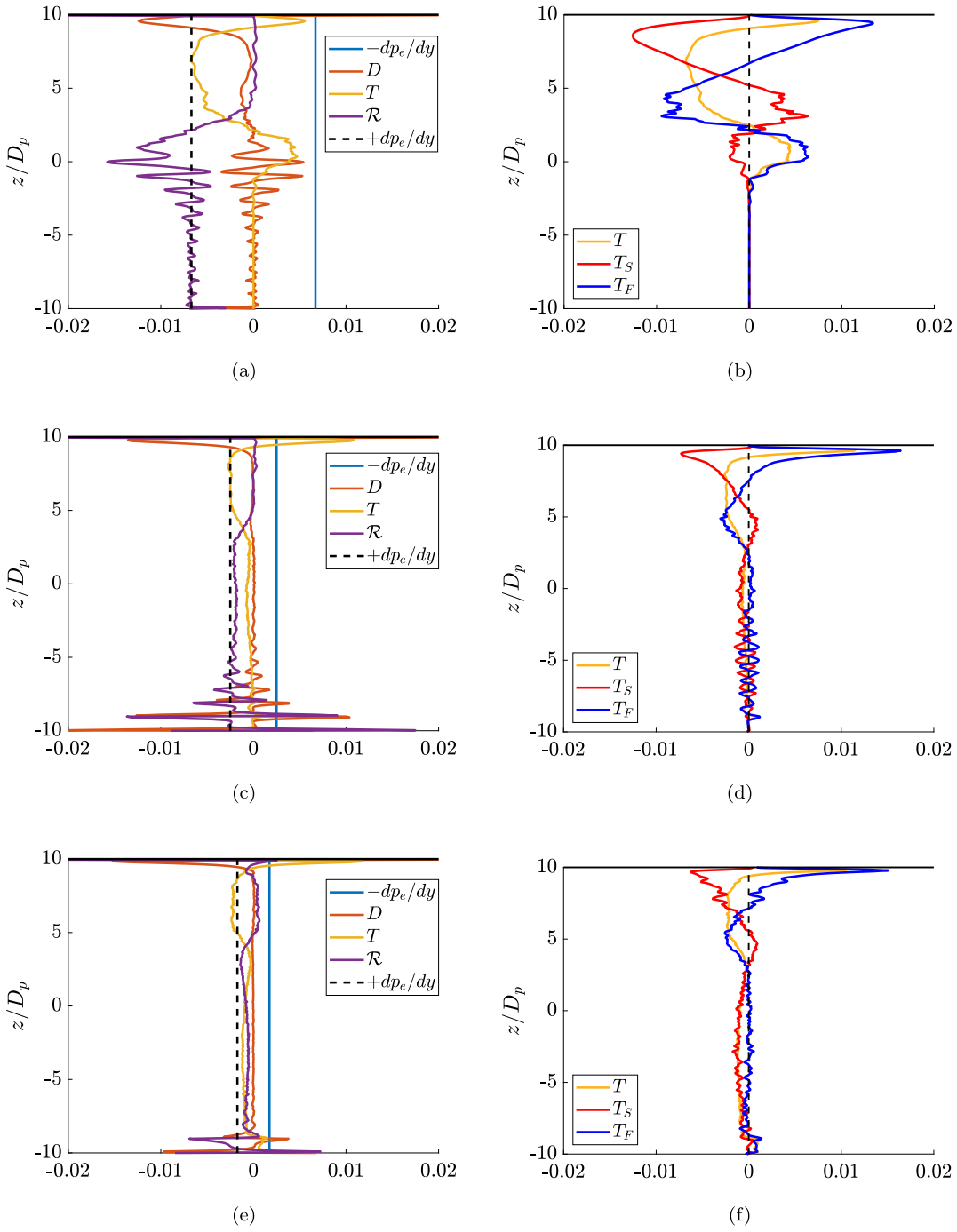


**Fig. 10.** Mean streamwise momentum balance in the streamwise-vertical midplane (left) and decomposition of the flow-induced momentum transport into contributions from the mean macroscopic secondary flow and turbulent motions (right), shown for the DNS cases D1 (a,b), D2 (c,d) and D3 (e,f). $-\overline{dp_e/dy}$, $D$, $T$ and $R$ correspond to the external pressure gradient that drives the flow, viscous diffusion, transport of mean momentum by secondary flow ($T_S$) and turbulent stresses ($T_F$), and momentum transfer by particle stresses, respectively. In the left panels, $+\overline{dp_e/dy}$ is indicated with a black dashed line for visual comparison. The budget terms are normalized with $\rho_f u_{bl}^2/D_p$.

the flow corners and downward transport of low-momentum fluid from the region near the pipe top. In case D2, the transport by secondary flow is dominant over turbulent transport in the low-concentration zones in between the pipe wall and the sliding bed. Finally, for case D3, turbulence appears strongly suppressed inside the entire lifted particle core given the zero transport from turbulent motions in this area. Note the significance of momentum transport by turbulent motions in the low-concentration zones flanking the dense particle core. This supports our previous hypothesis that the downward secondary flow in these zones is generated by turbulent motions and possibly augmented by particle-stress gradients and local particle sedimentation.

### 6.6. Discussion

In general, the DNS results are in fairly good agreement with the corresponding experiments. Each of the three investigated cases resembles a different flow regime: the fixed-bed regime for case D1/E1, the sliding-bed regime for case D2/E2, and the suspended regime for case D3/E3, though the degree to which particles are suspended in the flow

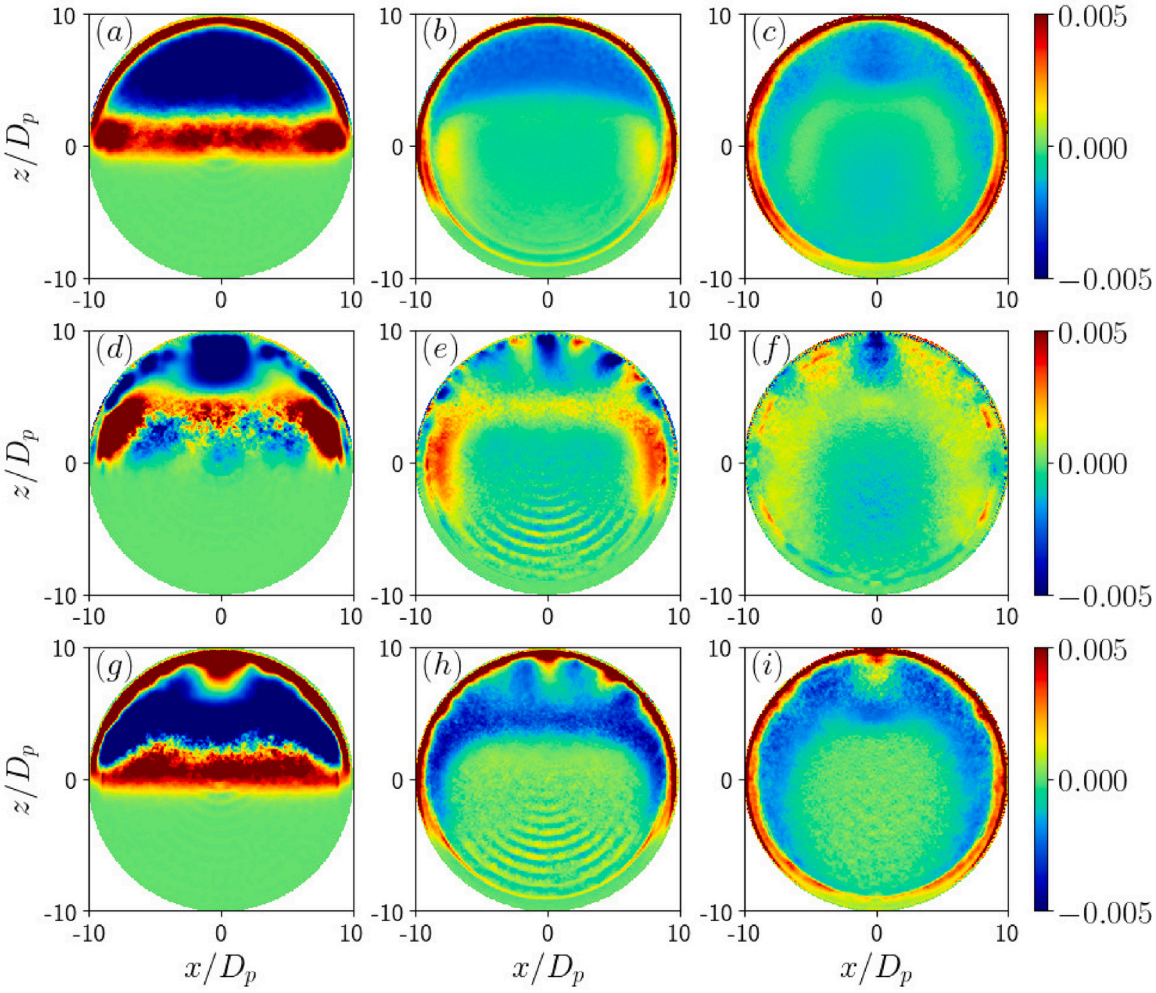


**Fig. 11.** Spatial distribution of the flow-induced momentum transport defined by Eq. (23b) ($T$, top row), and the contributions from the macroscopic mean secondary flow ($T_S$, middle row) and turbulent stresses ($T_F$, bottom row), shown for the cross-flow plane for cases D1–D3. (a,d,g) Case D1. (b,e,h) Case D2. (c,f,i) Case D3.

is significantly higher in the DNS (case D3) than in the experiment (case E3). The quantitative differences between the DNS and experiments are attributed primarily to two factors.

First, from Fig. 7 we observe a lower peak velocity in the DNS cases D1 and D2 than in the corresponding experiments, suggesting that the experimental value of the bulk liquid velocity and thus $Re$, which served as input parameter for the DNS, was underestimated. As discussed in Section 3 and Appendix B, the liquid bulk velocity in the horizontal test section was not measured directly and had to be determined indirectly from available experimental data based on a number of assumptions and related uncertainty in the final estimate. An underestimation of the liquid bulk velocity in cases D1 and D2 is consistent with a lower friction factor in these DNS cases as compared to the corresponding experiments, see Fig. 5.

Second, another source of uncertainty relates to the actual value of the Galileo number: $Ga = 37.9 \pm 12.3$ at a reference temperature of $T = 25$ °C, see Appendix A. The relatively large uncertainty in $Ga$ stems from the small relative density difference in the experiments, $(\rho_p/\rho_f - 1) \approx 0.02$, which strongly amplifies the uncertainty in the measured particle mass and particle diameter, see Eq. (A.2). We hypothesize that the higher degree to which particles are suspended in case D3, might originate from an underestimation of the actual Galileo number in the experiments and thus that the value used in the DNS was too low. Supporting evidence for this is given by the similar friction factor in Fig. 5 and similar peak velocity in Fig. 7 for cases D3 and E3, indicating a similar power input per unit pipe length from the driving pressure gradient, $(-\overline{dp_e/dy})(\pi D_{pipe}^2/4)\, v_{mix}$ with $v_{mix}$ the bulk mixture velocity. If the power input is the same, part of which is needed to counteract gravity, then the higher degree to which particles are suspended in the DNS, is consistent with an underestimation of the relative density difference and thus the Galileo number in case D3.

Other possible causes for the observed discrepancies between the DNS and the experiments could be related to some, though limited, degree of polydispersity in size, shape and density of the particles used in the experiments, and experimental uncertainty in the parameters of the collision/contact model, see Appendix A. In particular, the Coulomb coefficient of sliding friction, $\mu_c$, is deemed important for the sliding and suspended regime with frequent occurrence of particle/particle contact. Nonetheless, the spread in the measured values for $\mu_c$ is rather small, see Appendix A. In light of the above discussion, for future experiments we recommend to measure the liquid bulk velocity directly in the horizontal test section itself. Furthermore, we recommend to use PMMA particles with $\rho_p \approx 1200\ \mathrm{kg/m^3}$ in an aqueous glycerine solution. This will not only enhance the particle/fluid density contrast, but also provides flexibility in tuning the glycerol weight fraction for the desired fluid viscosity in order to keep the Galileo number around 40–45 as in the present experiments. As explained earlier, relatively low Galileo numbers are required to suspend the particles at moderate Reynolds

numbers in reach of DNS. Finally, other measurement techniques such as Magnetic Resonance Imaging (MRI) may be considered too, which would enable simultaneous and accurate measurements of the local particle velocity and concentration field (Hogendoorn, 2021; Hogendoorn et al., 2023).

## 7. Parametric DNS study

The comparison between experiment and DNS was performed at different $Re$, $Ga$ and $\phi_b$. To investigate the influence of these parameters individually, an additional DNS study was performed. This consisted of five different cases, labeled S1–S5, of which the parameters are listed in Tables 1 and 2. In cases S1–S4, only $Re$ was varied, which is lowest for S1 and highest for S4. The parameters of case S5 are the same as for S4, except that $Ga$ is twice as small.

### 7.1. Instantaneous flow snapshots

Fig. 12 shows instantaneous flow snapshots in two different pipe cross-sections as well as the 3D particle distribution over the upstream part of the pipe. With increasing $Re$ (S1–S4) and decreasing $Ga$ (S4–S5), we observe that more particles are entrained into the flow. In case S1 we observe a fixed bed with clear particle layering, at least near the wall, and a turbulent flow above the bed as in cases E1/D1. In cases S2 and S3, the flow is in the sliding-bed regime as in cases E2/D2. In cases S4 and S5, we observe a suspended-flow regime. Interestingly, while case S4 displays a clear heterogeneous particle distribution across the pipe, with more particles and slower flow at the pipe bottom than at the pipe top, in case S5 the particle distribution and flow appears nearly axisymmetric. In the latter case, a pronounced particle plug is present with a high particle concentration in the center of the pipe. While turbulence is fully damped inside the dense particle plug, the flow appears clearly turbulent outside the plug.

### 7.2. Mean concentration and velocity distributions in cross-flow plane

Fig. 13 shows the mean concentration and mean secondary flow in the cross-flow section of the pipe for cases S1–S5. Because of mirror-symmetry only half of the pipe is shown. A clear layered arrangement of particles in concentric rings can be observed for cases S1–S3 and to a lesser extent for case S4 near the pipe bottom. In case S4 we observe that the majority of the particles is lifted upwards in a plug between $z \approx -7$ till 3 with a fairly uniform concentration. In case S5 a large fraction of the particles even migrated towards the center of the pipe, where a distinct densely packed particle core can be seen with a diameter equal to $\sim 5D_p$. Furthermore, as already noticed from the flow snapshot of case S5 in Fig. 12, the mean particle concentration is nearly axisymmetric, though with a slightly upwards offset of the dense particle core and the presence of a more concentrated particle–wall layer at the pipe bottom as compared to the pipe top due to gravity. As discussed before for case D3, we attribute the origin of the dense particle core and particle–wall layer in case S5 to shear-induced migration and particle–wall lubrication at the pipe wall, respectively. The very same flow features have been recently observed for dense neutrally-buoyant particle suspensions in pipe flow by Hogendoorn et al. (2023). Also, a similar concentration distribution was reported by Zhang et al. (2021a) for horizontal gas–solid pipe flow for their highest investigated Froude number, albeit with much less pronounced particle–wall layering. Obviously, in case S5, $Re$ is sufficiently high and $Ga$ is sufficiently low to reach a high value of the Shields number such that shear-induced particle migration towards the pipe core can overcome the tendency of particles to settle under gravity.

The radial force acting on the particles from shear-induced migration towards the pipe center (i.e., towards the low-shear zone) is expected to gradually increase with $Re$ associated with the increase in shear rate. We argue that shear-induced migration is already significant in the sliding-bed regime and responsible for the gradual expansion of the low-concentration zones flanking the bed towards the pipe bottom as can be observed from Figs. 13b–d. Simultaneously, the wedge-shaped high-concentration zone at the bottom of the pipe becomes smaller. We associate this high-concentration zone with the region where shear-induced migration is too weak to 'fluidize' the bed, related to the weaker mean shear rate in this region and the larger component of gravity acting in the direction perpendicular to the pipe wall in this zone.

In all cases, a clear secondary flow is present, which is confined to the top half of the pipe in cases S1 and S2, but extends over the entire cross-section in cases S3–S5. Furthermore, as observed before for cases D1–D3, the secondary flow pattern is intertwined with the spatial particle distribution. Albeit minor differences can be observed, the secondary flow patterns in cases S1, S3 and S4 are quite similar to the patterns observed before for cases D1, D2 and D3, respectively; this is probably because of the fairly similar Froude and Shields numbers, see Tables 1 and 2. Normalized with the liquid bulk velocity, the strength of the secondary flow significantly drops from case S1 to S5.

In case S5, the secondary flow is weak (less than 1% of the liquid bulk velocity), which we ascribe to the near axisymmetry of the mean concentration and streamwise velocity distribution in this case, similar to the reason why a secondary flow is absent in single-phase turbulent pipe flow (Nikitin et al., 2021). A weak upward flow is present from the bottom of the pipe towards the dense particle core and a downward flow near the pipe edges around $x/D_p \approx \pm 9$. Inside the dense particle core of case S5, the secondary flow is close to zero and hence not contributing to lifting of the core. Apart from the near axisymmetry of the flow, we ascribe the nearly zero secondary flow inside the core also to the locally high suspension viscosity and low permeability of the core packing.

While the concentration field in S5 is nearly axisymmetric in the core region, this is not the case near the wall, with more pronounced particle–wall layering at the bottom than at the top. This is clearly visible in the mean concentration and mean velocity profile along the streamwise-vertical midplane in Fig. 14a and b. The loss of axisymmetry near the pipe wall combined with the dense sphere packing in the pipe core, is ultimately responsible for the rather complex mean secondary flow pattern in Fig. 13j with a clear up–down asymmetry.

### 7.3. Mean concentration and velocity profiles

In Fig. 14a and b the mean concentration and velocity profiles are plotted as function of height in the streamwise-vertical midplane. The concentration profiles of cases S1–S3 are characterized by typical oscillations of about one particle diameter, related to regular particle layering within the bed. Peak concentrations well beyond 0.8 are observed, close to the value of approximately 0.91 for a hexagonal packing of circles in a plane (cf. the packing of the spheres near the wall in cases S1–S3 in Fig. 12). The uniform concentration plug in case S4 has a packing fraction somewhat less than 0.4. Different from case S4, where the concentration profile is non-axisymmetric and characterized by a large uniform plug, the profile in S5 is predominantly axisymmetric with a gradually varying concentration. The peak concentration in case S5 with a value of slightly less than 0.6, suggests a loose random sphere packing in the pipe center. The emerging picture is that shear-induced particle migration is responsible for 'filling' of the pipe core up to the maximum possible concentration for a loose random packing, after which the particle plug expands radially outwards (Hogendoorn et al., 2023). We hypothesize that the growth of the particle plug stops once shear-induced migration (which is expected to weaken for decreasing concentration outside the plug) counterbalances turbulent particle diffusion in the region outside the particle plug.

For case S5 the particle concentration at the pipe bottom is significantly higher than at the pipe top by a factor of 1.5–2, likely related to an effect of gravity. This asymmetry in the particle concentration

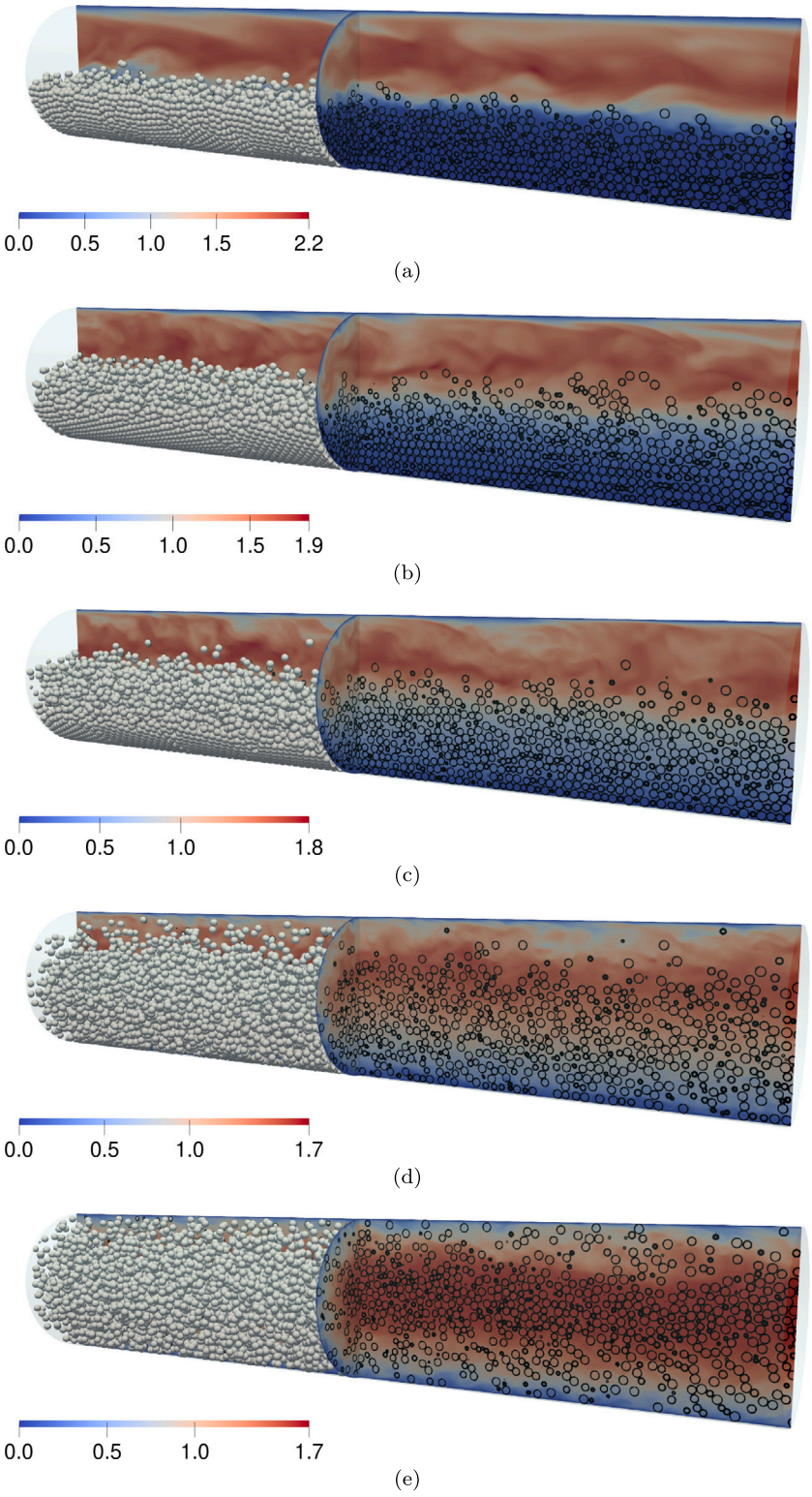


**Fig. 12.** Instantaneous flow snapshots in two different pipe cross-sections as well as the 3D particle distribution over the upstream part of the pipe. The flow is going from left to right. The color denotes the streamwise velocity normalized with the liquid bulk velocity. Contours in the cross-sections indicate the particle positions (local grid cell solid volume fraction equal to 0.5). (a) S1, (b) S2, (c) S3, (d) S4, and (e) S5. (For interpretation of the references to color in this figure legend, the reader is referred to the web version of this article.)

near the wall is accompanied by a corresponding asymmetry in the mean velocity profile (cf. Fig. 14b). We speculate that this has been responsible for enhanced wall friction and stronger shear-induced particle migration in the bottom half of the pipe as compared to the top half, which is consistent with the slight upward offset of the dense particle core with respect to the pipe centerline in this case.

The mean velocity profile in case S1 is similar to case D1 and characterized by a very slow (nearly zero) fluid flow through the fixed particle bed described by Darcy's law. The mean velocity profile in cases S2

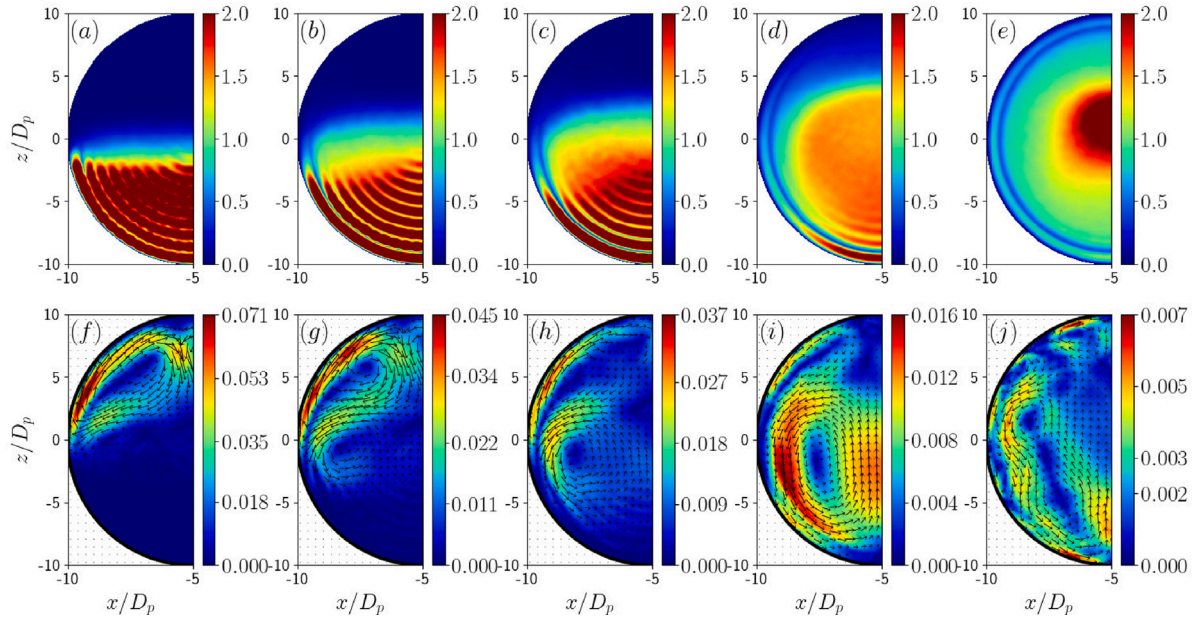


**Fig. 13.** (a)–(e) Mean concentration field in the cross-flow section of the pipe for cases S1–S5. The color value indicates the mean concentration scaled with the bulk concentration $\phi_b$. (f)–(j) Mean secondary fluid flow, $\overline{\langle u_f \rangle}/v_{bl}$ and $\overline{\langle w_f \rangle}/v_{bl}$, in the cross-flow section of the pipe for cases S1–S5. The color denotes the secondary flow magnitude $\sqrt{\overline{\langle u_f \rangle}^2 + \overline{\langle w_f \rangle}^2}/v_{bl}$ and the vectors indicate the direction of the secondary flow. The reference vector length has been rescaled for every case to optimize visibility. (For interpretation of the references to color in this figure legend, the reader is referred to the web version of this article.)

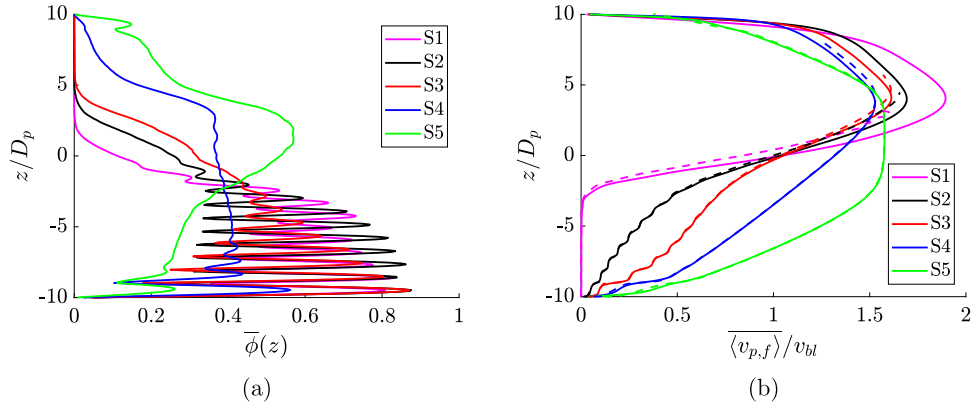


**Fig. 14.** (a) Mean concentration and (b) mean velocity profiles in the streamwise-vertical midplane of the pipe for cases S1–S5. The solid and dashed lines in (b) denote the fluid and particle velocity profiles, respectively.

and S3 is gradually increasing with height inside the sliding bed and the mild oscillations visible in the velocity profile are consistent with the oscillations in the corresponding concentration profiles. The mean velocity profile in case S5 is blunted in the core, which can be explained from the high concentration in the dense particle core and related high values of the particle shear stress and suspension viscosity. Finally, we note that the mean velocity profiles for the particles and fluid nearly coincide in all cases, indicating negligible macroscopic slip between the solid and fluid phase in the streamwise direction, in particular for cases S2–S4 in the lower half of the pipe and for case S5 away from the particle–wall layer. The particle Stokes number varies between $St = 0.04 - 0.11$ for cases S1–S5, and the low values may thus explain the negligible slip.

### 7.4. Particle-mean velocity and height

In Fig. 15a, the particle-mean streamwise velocity (red symbols) and the particle-mean height (black symbols) are shown as function of $Re$. Interestingly, normalized with the liquid bulk velocity, the particle-mean velocity increases close to linearly with $Re$ between cases S1–S3 (i.e., the left three data points), suggesting that below $Re \approx 2000$ the particles would not move anymore at all. In case S4 the particle move on average with approximately the same velocity as the liquid phase. In case S5, where $Ga$ is twice as low as in case S4 at the same $Re$, the particle-mean velocity is about 20% higher than the liquid bulk velocity, consistent with the high particle concentration in the core in this case where the velocity is maximum. Interestingly, this is accompanied by a drop of nearly 10% in the streamwise pressure gradient for case S5 (based on Table 2 and given that the streamwise pressure gradient is proportional to $v_\tau^2$), likely related to the much lower particle concentration near the bottom of the pipe compared to case S4 as can be observed from Fig. 14a. This is in line with the recent study of Hogendoorn et al. (2023) on dense suspensions of neutrally-buoyant spheres in pipe flow, who reported drag reduction for core-peaking concentration distributions up to about 25% compared to the expected drag for a spatially uniform concentration distribution. They ascribed

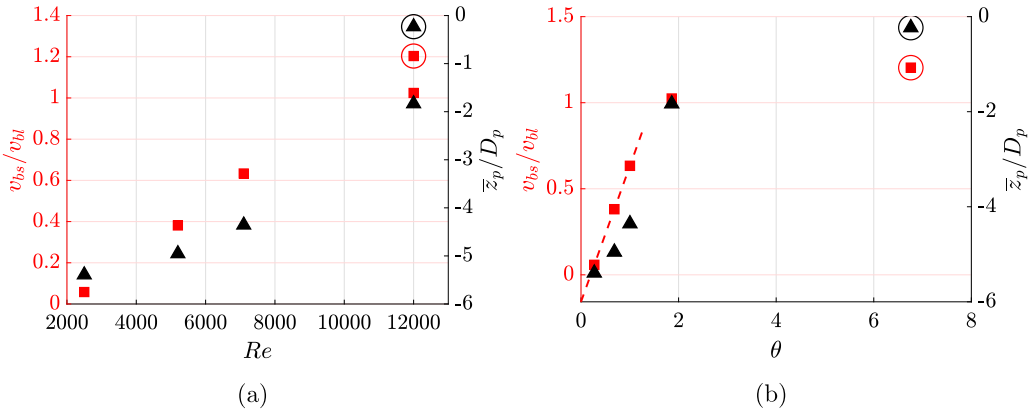


**Fig. 15.** (a) Particle-averaged statistics for cases S1–S5 as function of $Re$. The left axis (red color and square symbols) shows the particle-mean streamwise velocity, $v_{bs}$, normalized with the liquid bulk velocity. The right axis shows the particle-mean vertical position in the pipe. The data points of case S5 are encircled. (b) Particle-averaged statistics for cases S1–S5 as function of $\theta$. The dashed line is a linear fit through the particle-mean streamwise velocity of cases S1–S3. (For interpretation of the references to color in this figure legend, the reader is referred to the web version of this article.)

this to the relatively low concentration outside the dense particle core, which acts as an apparent lubrication layer with a relatively low viscosity between the dense and highly viscous particle core and the pipe wall.

The particle-mean vertical position in the pipe increases with $Re$ in a clearly non-linear fashion. The lowest value found for case S1 is close to the limiting value corresponding to the case where all particles are settled in a bed at the pipe bottom and do not move at all. While in all cases the particle-mean position is negative, in case S5 the value is close to zero, indicating nearly negligible effect of gravity in this case.

In Fig. 15b the particle-mean (or solid bulk) streamwise velocity and particle-mean vertical position in the pipe are again depicted, but now as function of the Shields number, $\theta$. The solid-to-fluid bulk velocity ratio, $v_{bs}/v_{bl}$, rises steeply with $\theta$ for the low $\theta$-range, while beyond $\theta \approx 1$ the bulk velocity ratio increases less steeply with $\theta$ and should ultimately become independent of $\theta$ for high $\theta$ when gravity effects are expected to be negligible. Interestingly, for cases S1–S3 (i.e., the lower $\theta$-range), the bulk velocity ratio appears to scale as $v_{bs}/v_{bl} \approx 0.78 \cdot (\theta - 0.19)$, as indicated by the dashed line in the figure. This suggests a critical Shields number of about 0.19 beyond which particle transport is initiated by the flow over the bed, at least under the conditions chosen for the parametric DNS study. This is quite a bit higher than the critical value of 0.03–0.04 expected a priori from the original Shields diagram (Shields, 1936) given that the so-called grain Reynolds number of case S1 is equal to $v_\tau D_p/\nu_f \approx 20$. The reason for this is not fully clear. It might be related to non-linear scaling of $v_{bs}/v_{bl}$ as function of $\theta$ just above the critical Shields number for incipient motion, which would thus invalidate our estimate based on the linear fit. Furthermore, we remark that the line fit would predict that $v_{bs}/v_{bl} \approx 0.27$ in case D1, while the actual value is 0.13 in this case (see Table 2). This indicates that $v_{bs}/v_{bl}$ depends also on $Ga$ and/or $\phi_b$ as the values of these parameters were different in case D1 as compared to the parameter values chosen for the parametric DNS study. Finally, we remark that our flow geometry is different from the open-channel flow geometry studied by Shields and characterized by the presence of a secondary flow. We speculate that the downward-directed flow from the top of the pipe towards the bed as observed for the fixed-bed regime, see Fig. 13f, might have a stabilizing effect on the bed.

### 7.5. Streamwise momentum balance

As before for cases D1–D3, also for cases S1–S5 we analyze the streamwise momentum balance given by Eq. (23)a–d. The different contributions to the balance are presented in Fig. 16 for the streamwise-vertical midplane. From the comparison with Fig. 10 for cases D1–D3, it may be noticed that S1 is similar to D1 (fixed-bed regime), S2 and in particular S3 are similar to D2 (sliding-bed regime), and S4 is similar to D3 (heterogeneously suspended regime). Hence, cases S1–S4 are not discussed here for the sake of brevity and we focus on case S5.

In case S5, we observe a near vertical symmetry about the center of the pipe, suggesting negligible influence of gravity. As discussed before, the observed deviation from perfect vertical flow symmetry is attributed to a still minor influence of gravity. In particular, the higher peak value of the particle-stress term at the pipe bottom relative to the pipe top, is consistent with the significantly more dense particle–wall layer near the pipe bottom (cf. Fig. 14a). For the core region, we observe that the pressure gradient is balanced entirely by momentum transport from the particle stress, originating from the high local particle concentration (cf. Fig. 14a) and the related high suspension viscosity which tends to diverge near the maximum flowable packing limit (Eq. (6)). While the flow-induced momentum transport is zero in the dense core region, indicating that turbulence is fully damped and secondary flow is absent here, it is the dominant loss term in the intermediate region of $4.5 \lesssim |z|/D_p \lesssim 8.5$ between the dense particle core and the pipe wall. The decomposition of the flow-induced transport in Fig. 16f shows that it originates almost fully from turbulent motions and related turbulent diffusion for $4.5 \lesssim z/D_p \lesssim 8.5$ in the upper part of the pipe, while it is the combined transport from secondary flow in the first place and turbulent diffusion in the second place for $-8.5 \lesssim z/D_p \lesssim -4.5$ in the lower part of the pipe. The dominance of the transport by secondary flow in the lower part of the pipe is rather surprising, given the weak secondary flow magnitude of less than 1% of the liquid bulk velocity (Fig. 13.j). The negative sign of the transport by secondary flow is consistent with the upward flow in the bottom half of the pipe that transports low-momentum fluid from the bottom wall region towards the pipe core. Turbulent diffusion is negative for $4.5 \lesssim |z|/D_p \lesssim 8.5$, but swaps sign and becomes positive inside the particle layer lining the pipe wall, related to the transport of high-momentum fluid by turbulent motions from the core region towards the wall. Within the particle–wall layer, the pressure gradient is balanced by the combined momentum transport from viscous diffusion, turbulent diffusion and the divergence from the particle stress. The contribution from the particle stress can be related to the local suspension viscosity (a diffusive effect) and a possible consequence from a slight macroscopic slip between the particles and the fluid in this layer (a drag effect), see Fig. 14b. Exactly at the wall,

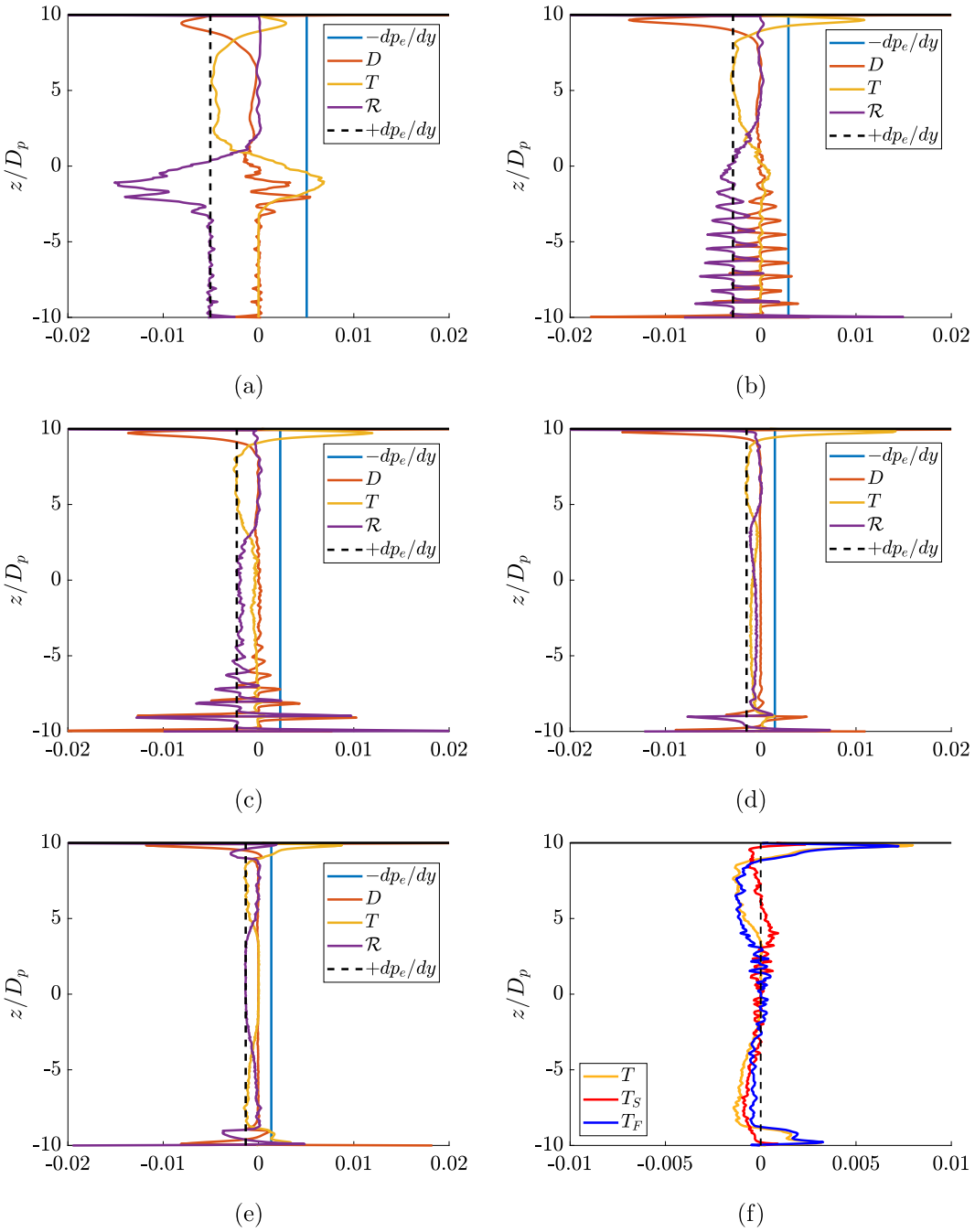


**Fig. 16.** (a)–(e) Mean streamwise momentum balance in the streamwise-vertical midplane, shown for cases S1 (a), S2 (b), S3 (c), S4 (d) and S5 (e). $-\overline{dp_e/dy}$, $D$, $T$ and $R$ correspond to the external pressure gradient that drives the flow, viscous diffusion, flow-induced transport of mean momentum by secondary flow and turbulent fluctuations, and momentum transfer by particle stresses, respectively. $+\overline{dp_e/dy}$ is indicated with a black dashed line for visual comparison. The budget terms are normalized with $\rho_f v_{bl}^2/D_p$. (f) Decomposition of the flow-induced transport term, $T$, into the contribution from the mean secondary flow, $T_S$, and turbulent fluctuations, $T_F$, shown for case S5. Note the change in the range of the $x$-axis with respect to panels (a)–(e).

the streamwise pressure gradient is balanced by viscous diffusion and the divergence of the particle shear stress.

Finally, Fig. 17 depicts the spatial distributions of the flow-induced transport term, $T$, and the separate contributions from the mean secondary flow, $T_S$, and turbulent motions, $T_F$, for the cross-flow plane. The spatial distributions for cases S1–S4 by and large resemble the ones of cases D1–D3 previously discussed in Section 6.5. For case S5, the negative flow-induced transport in the layer between the dense particle core and the particle–wall layer is mostly dominated by turbulent diffusion except in the regions directly below the core at $x = 0$ and sidewards of the core around $x/D_p \approx \pm 8$ where secondary flow contributes to the overall transport. Though the flow and concentration distributions in case S5 are nearly axisymmetric, the overall stronger turbulent diffusion in the upper part of the pipe indicates that turbulent motions are generally stronger here than in the bottom part of the pipe. An explanation for this might be the stronger turbulence production in the upper half of the pipe related to the generally steeper mean velocity gradient here from the upward offset of the dense particle core.

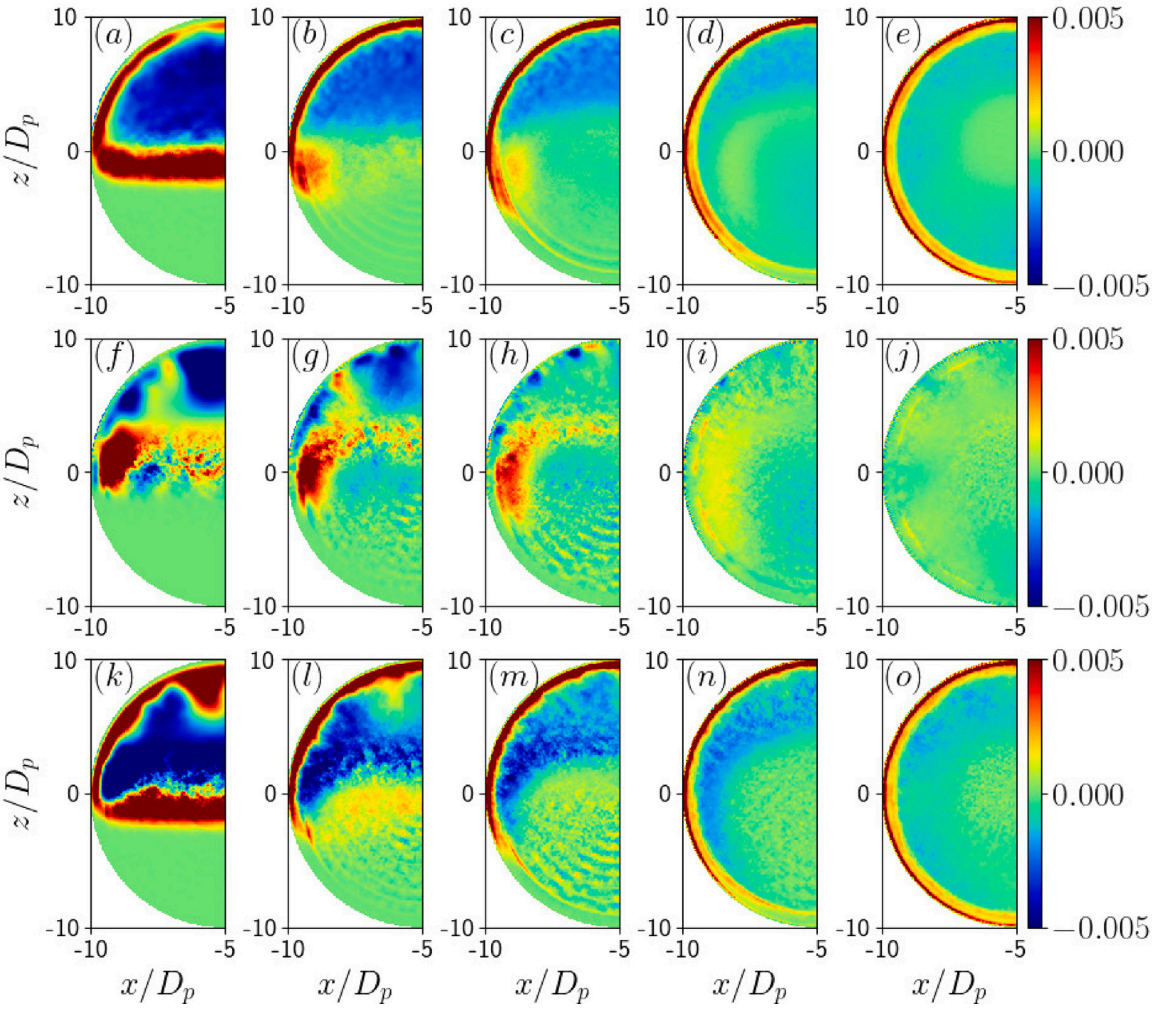


**Fig. 17.** Spatial distribution of the flow-induced momentum transport defined by Eq. (23b) ($T$, top row), and the contributions from the macroscopic mean secondary flow ($T_S$, middle row) and turbulent stresses ($T_F$, bottom row), shown for the cross-stream plane for cases S1–S5. (a,f,k) Case S1. (b,g,f) Case S2. (c,h,m) Case S3. (d,i,n) Case S4. (e,j,o) Case S5.

## 8. Conclusions and discussion

We have studied the three basic transport regimes in horizontal slurry pipe flow by means of experiments in a slurry flow loop and interface-resolved DNS. In general, we found the DNS results in fairly good agreement with the experimental results, in particular given the experimental uncertainty in the actual values of the liquid bulk velocity and Galileo number. We also found fairly good agreement of the friction factor with popular empirical models from literature.

The experiments and simulations provided detailed insight into the characteristics of horizontal slurry transport through a small-diameter pipe. The densimetric Froude number, $Fr$, and in particular the Shields number, $\theta$, are useful metrics to distinguish between the different flow regimes. Our main findings are summarized below.

- In the fixed-bed regime for $Fr \lesssim 1$ and $\theta \lesssim 0.75$, a rather sharp and flat interface exists between the overlying flow and the stationary bed. The bed is characterized by a regular packing of the spheres in circular rings. The particle alignment along the pipe wall originates from the constraint that the spheres cannot overlap with the wall. The perfect monodispersity of the spheres, at least in the DNS, is responsible for further layering deeper inside the bed. The flow inside the stationary bed is governed by Darcy's law with the bed permeability comparable to the prediction from the modified Ergun model for slow flow through a packed bed. The turbulent flow above the bed is characterized by a secondary flow of Prandtl's second type and characterized by two main counter-rotating vortices related to the presence of two internal flow corners at the locations where the flat bed interface meets the pipe wall. The vortices stretch from the flow corners to the pipe top and are associated with a downflow from the pipe top into the bulk liquid above the bed. In the bulk of the turbulent flow above the bed, secondary flow transport and turbulent diffusion of streamwise momentum are balancing the streamwise pressure gradient. Here, secondary flow transport dominates over turbulent diffusion in regions where the secondary flow is strong, and vice versa in regions where the secondary flow is weak.
- In the sliding-bed regime for $1 \lesssim Fr \lesssim 2$ and $0.75 \lesssim \theta \lesssim 1.5$, the interface between the sliding bed and overlying turbulent flow is diffuse and curved down sideways. Turbulent low-concentration zones are flanking the top part of the bed. Furthermore, particle layering is still present within the bed, but confined to a wedge-shaped high-concentration zone above the pipe bottom. The secondary flow is characterized by a pair of counter-rotating vortices in the turbulent flow above the bed, with similar characteristics as in the fixed-bed regime, and another pair of counter-rotating vortices that extends over the lower half of the pipe though damped in the bed core. Inside the bed, the mean particle and fluid velocity gradually increase with height with negligible macroscopic slip. The streamwise pressure gradient is balanced

here by the divergence of the particle shear stress associated with a high suspension viscosity from particle layers moving under shear.

- The suspended-flow regime for $Fr \gtrsim 2$ and $\theta \gtrsim 1.5$, is characterized by a dense lifted core of particles, which moves towards the pipe centerline with increasing $Fr$ and $\theta$. For very high $Fr$ and $\theta$, gravity has a minor influence on the flow dynamics, resulting in nearly axisymmetric distributions of the mean flow and concentration and a characteristic concentration peak near the pipe wall from a particle layer lining the wall. The peak concentration in the core is about 0.6, characteristic for a random loose packing of spheres. The very high suspension viscosity in the core is responsible for a locally uniform velocity distribution and full damping of turbulence. Furthermore, the secondary flow has nearly disappeared in this limit as a result of the statistical axisymmetry of the flow. For the lower range of $Fr$ and $\theta$, when the lifted core of particles is still located significantly below the pipe centerline, the secondary flow pattern is similar to the pattern in the sliding bed regime, but the upper vortex pair is more confined to the pipe top and the lower vortex pair exhibits more pronounced upflow around the streamwise-vertical midplane. For $Fr \sim 3.5$ and $\theta \sim 2$, the upward secondary flow inside the particle core is found to be the dominant mechanism for transport of streamwise momentum across the core, with a secondary role for particle-induced diffusion related to the high suspension viscosity.
- For $\theta \lesssim 2$, the Darcy–Weisbach friction factor scales approximately as $f \sim 1/Re_{mix}$ and the Shields number as $\theta \sim Re_{mix}$, at least when all other parameters ($Ga$, $\phi_b$, $D_p/D_{pipe}$, $\rho_p/\rho_f$, collision/contact parameters) are fixed. Since a turbulent flow is present in all cases, we ascribe this quasi-laminar behavior of the friction factor to changes in the flow topology and the amount of sediment carried by the flow. For $\theta \gg 1$, $f$ seems to become approximately constant in $Re_{mix}$ and $\theta \sim Re_{mix}^2$, consistent with the expectation for a turbulent flow in the presence of wall roughness related to a particle layer lining the wall.
  Using the analogy of the flow above the bed with the flow in a circular pipe with the same hydraulic diameter and wall roughness, we proposed a model for the friction factor in the fixed-bed regime. Although this model does not account for secondary flow effects, still good agreement was found with the friction factor obtained from the DNS. For the sliding-bed regime, the friction factor is described well with the sliding-bed model of Newitt et al. (1955) and the modified Durand–Condolios model (Newitt et al., 1955). The strong overprediction by the original Durand–Condolios model (Durand and Condolios, 1953) underlines the importance of using the reduced gravity instead of gravity itself in the modeling of the friction factor, especially when the density ratio is strongly different from the value of $\approx 2.65$ in the experiments of Durand and Condolios. For the heterogeneously suspended regime, the friction factor appears to be well described by the heterogeneous suspension model of Newitt et al. (1955).
  Our results on the influence of the Galileo number on the suspended flow regime at fixed bulk liquid Reynolds number (e.g., by simultaneously varying the bulk liquid velocity and the fluid viscosity), show that the axisymmetric core-peaking concentration distribution at high $\theta$ is accompanied by a reduction in drag and pressure drop relative to the non-axisymmetric concentration distribution at less high $\theta$. This is ascribed to a higher particle concentration near the bottom wall for the non-axisymmetric case.
- All flow regimes are characterized by a secondary flow of Prandtl's second kind comprising mainly one counter-rotating vortex pair in the fixed-bed regime and two main counter-rotating vortex pairs in the other regimes. The maximum strength of the secondary flow is on the order of a few percent of the liquid bulk velocity. In all flow regimes, the secondary flow patterns, the mean streamwise velocity and the spatial concentration distribution appear intimately related and mutually coupled with each other. Because of the resemblance to the secondary flow found for turbulent single-phase flow in semi-circular pipes, the upper vortex pair likely originated from turbulent motions in the apparent presence of internal flow corners. The origin of the lower vortex pair is more complex. We hypothesize that the downflow in the low-concentration zones flanking the bed, is primarily caused by turbulent motions in a corner-like geometry and possibly amplified by particle-stress gradients and local particle sedimentation. While the upflow in the core of the bed is weak in the sliding-bed regime due to the high suspension viscosity, it is significant in the suspended-flow regime. Since turbulence is fully damped here, we hypothesize that this upflow inside the lifted particle core originates from particle-stress gradients, which arise from centrifugal forces acting on curved paths of fluctuating particle motions near the wedge-shaped high-concentration zone at the pipe bottom.
- The prime physical mechanism for transition between the flow regimes is the competition in the bed region between the downward-directed net gravity force on the particles and shear-induced particle migration from particle–particle interactions towards a low-shear region. In this respect, the square root of the Shields number, $\sqrt{\theta}$, can be interpreted as the time scale ratio of gravity acting on a single particle within the bed, $\sqrt{D_p/(\rho_p/\rho_f - 1)g}$, to a time scale of the shear rate imposed by the overlying turbulent flow onto the hydraulically rough bed, $D_p/v_\tau$. The definition of the Shields number thus seems to capture the relevant physics for flow transition in slurry pipe flow. This is less clear for the densimetric Froude number as it does not contain the particle diameter and is based on the mixture bulk velocity rather than the friction velocity related to the bed shear stress.
- The shear-induced particle migration can be understood from repulsive forces from lubricated and collisional contacts between adjacent particle layers under shear and thus in relative motion, resulting in a tendency of particles to accumulate in a region with low shear. Particle inertia may reinforce shear-induced migration. Assuming that the shear rate scales with $v_\tau/D_p$ and considering that $\rho_p/\rho_f$ is nearly one in our study, this effect can be qualitatively assessed by means of the grain Reynolds number, $Re_p = v_\tau D_p/\nu_f$ (Picano et al., 2013; Shields, 1936), which varies from approximately 30 in case S1 to approximately 50 in cases S4 and S5. This is thus well in the regime where 'inertial' shear thickening is expected to happen (Picano et al., 2013).
- The mechanism of shear-induced migration is already at work in the sliding-bed regime and responsible for (a) the formation of low-concentration zones flanking the upper part of the bed and (b) an apparent fluidization of the particles in the upper part of the bed at a solid volume fraction significantly below that of the wedge-shaped high-concentration zone at the pipe bottom. With increasing $\theta$, the low-concentration zones flanking the bed, extend further downwards along the pipe wall until the bed is fully lifted from the wall. The transition from the fixed-bed to the sliding-bed and ultimately the suspended regime for increasing $\theta$, is thus a gradual transition process in which shear-induced particle migration becomes progressively more important. In the fixed-bed regime, gravity is strongly dominant and shear-induced migration negligible. The transition from the fixed-bed to the sliding-bed regime is marked by the formation of low-concentration zones flanking the bed and the subsequent formation of a secondary flow here. Shear-induced particle migration starts to dominate over gravity first at the top corners of the bed. It is here that the local shear rate is sufficiently large and the local component

of gravity in the radial direction sufficiently small for shear-induced migration to dominate over gravity. The transition from the sliding-bed to the suspended regime corresponds to deepening of the low-concentration zones flanking the bed down to the bottom of the pipe. This is accompanied by the lifting of a dense particle core away from the wall and with a local maximum in the concentration (after filtering out the possible presence of particle layering). For very high Shields number, gravity will eventually become negligible, and shear-induced migration causes particles to accumulate in the pipe core until it is counter-acted by turbulent diffusion outside of the dense particle core.

The results from our study have some important implications for CFD modeling of slurry pipe flow. For Reynolds-averaged continuum (mixture and two-fluid) models to accurately capture secondary flow patterns and related effects on the flow dynamics, the closure model for the Reynolds-stress tensor should account for the stress anisotropy as this is a prerequisite for existence of the secondary flow in zero and low-concentration regions (Nikitin et al., 2021). Furthermore, because of the vital role played by shear-induced particle migration, accurate modeling of the particle stress is required, in particular particle stress gradients and, for capturing particle-induced secondary flow, anisotropy of the particle-stress tensor (similar to the anisotropy of the Reynolds-stress tensor required for generation of secondary flow by turbulence).

In the present study the particle/fluid density ratio was chosen close to 1 in order to obtain Shields numbers of $\mathcal{O}(1)$ at flow conditions in reach of DNS. To discuss this in more detail, we rewrite Eq. (22) into the following expression for the Shields number:

$$\theta = \frac{f}{8}\left(\frac{Re_{mix}}{Ga}\frac{D_p}{D_{pipe}}\right)^2.$$

DNS is limited to moderate values of $Re_{mix}$ as the required mesh width and computational time step to fully resolve the flow, both decrease with increasing $Re_{mix}$. Furthermore, interface-resolved DNS is also limited by the value of $D_{pipe}/D_p$ as the computational costs scale with the number of particles in the domain and the flow has to be resolved both at the pipe and the particle scale. This leaves the Galileo number as the 'free' parameter that can be 'tuned' for the desired range of the Shields number, i.e., to simulate the fixed-bed, sliding-bed and suspended-flow regimes at moderate values of the mixture Reynolds number as in the present study. A sufficiently low value of the Galileo number can be accomplished in three different manners: (1) by choosing a particle/fluid density ratio close to 1 as in the present study where $(\rho_p/\rho_f - 1) \approx 0.02$ and $Ga \approx 40 - 45$, (2) by increasing the kinematic fluid viscosity, and/or (3) by adopting a lower value for the gravitational acceleration. Though experimentally (nearly) impossible, the last option is numerically interesting as it enables to simulate for example sand/water slurries for realistic particle/fluid density ratio and fluid viscosity.

Through the present study, we hope to have sufficiently demonstrated the high potential of interface-resolved DNS to unravel the fundamental structure and dynamics of slurry pipe flow. To bridge the gap between idealized and real slurries, the present research may be extended towards investigating polydispersity effects in particle size, shape and density on the slurry flow dynamics and transition across flow regimes. We remark that polydispersity in size and shape may have a significant effect on the maximum (random) packing fraction (Baule et al., 2013; Desmond and Weeks, 2014) and hence on the bed height in the fixed and sliding bed regime for given solid bulk concentration. Furthermore, polydispersity is also expected to reduce the tendency of particles to arrange themselves in a regular packing as observed in the present study for perfect monodisperse spheres.

## Funding

This work is part of the research programme Topsector Water with Number ALWTW.2016.050, which is (partly) financed by the Dutch Research Council (NWO), The Netherlands.

## CRediT authorship contribution statement

**Tariq Shajahan:** Visualization, Conceptualization, Data curation, Formal analysis, Investigation, Methodology, Software, Validation, Writing – original draft. **Thijs Schouten:** Data curation, Investigation, Writing – review & editing. **Shravan K.R. Raaghav:** Investigation, Writing – review & editing. **Cees van Rhee:** Funding acquisition, Supervision. **Geert Keetels:** Conceptualization, Funding acquisition, Investigation, Methodology, Supervision, Writing – review & editing. **Wim-Paul Breugem:** Conceptualization, Formal analysis, Funding acquisition, Investigation, Methodology, Project administration, Software, Supervision, Writing – review & editing.

## Declaration of competing interest

The authors declare that they have no known competing financial interests or personal relationships that could have appeared to influence the work reported in this paper.

## Data availability

The data that support the findings of this study are openly available in 4TU.ResearchData at https://doi.org/10.4121/a3aa03d5-f01b-4de3-8e29-5766bd11489e.

## Acknowledgments

The authors would like to dedicate this article to the memory of our dear colleague and co-author Prof. Cees van Rhee, who passed away suddenly on July 15, 2023 while on vacation, shortly before we submitted our original manuscript to Int. J. Multiph. Flow. We thank SURF (https://www.surf.nl) for using the Dutch National Supercomputer Snellius for performing the numerical simulations and data analysis under Computing Grant No. 2020.036 from the Dutch Research Council (NWO), The Netherlands. Finally, we acknowledge the anonymous reviewers for their constructive feedback, which triggered us to conduct a more in-depth analysis of the DNS data.

## Appendix A. Measurements of material properties and related uncertainties

Tilted flume experiments were performed to estimate the Coulomb coefficient of static friction between (i) polystyrene particles, and (ii) between polystyrene particles and a plexiglass wall. The experimental setup is shown in Fig. A.1 and comprises a tiltable plexiglass box filled with tap water and a flat bed of particles. The Coulomb coefficient of friction between the polystyrene particles is measured from the tangent of the tilt angle at which there is initiation of motion of the bed of particles. The friction coefficient between polystyrene particles and the plexiglass bottom wall was measured in a similar manner, where (as opposed to a bed of particles) a number of polystyrene particles were glued to the bottom side of small plates and the tilt angle at which the plates began to slide was measured. The plates used are shown in Fig. A.2 and the measured friction coefficients are shown in Fig. A.3. From the measurements, we find that the friction coefficients for polystyrene-polystyrene contacts and for polystyrene-plexiglass contacts both have an overall mean value of close to 0.39. We adopted this value for the Coulomb coefficient of sliding friction in our interface-resolved DNS.

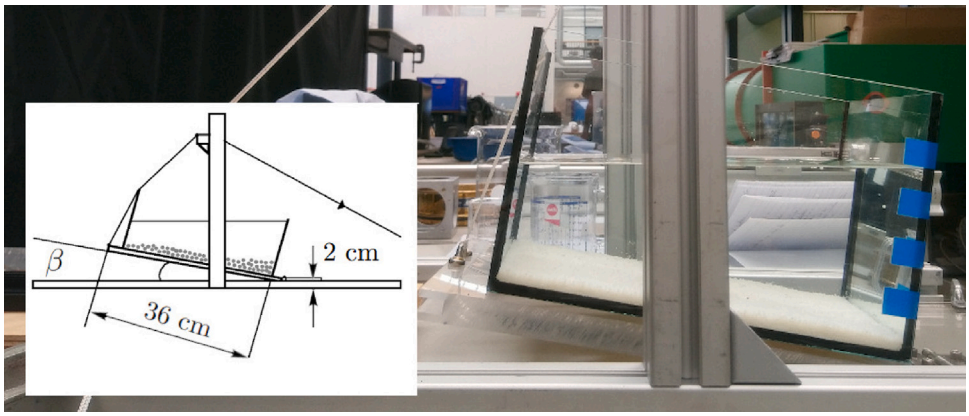


**Fig. A.1.** Experimental setup used to measure the Coulomb coefficient of static friction. The inset depicts a schematic of the setup. The coefficient of friction was estimated from the tangent of the angle $\beta$ at which initiation of motion was observed.

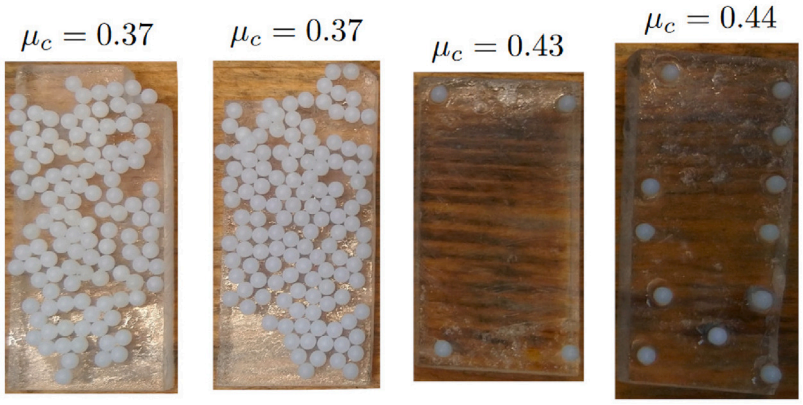


**Fig. A.2.** Plates with polystyrene particles used to estimate the Coulomb coefficient of static friction between the polystyrene particles and the plexiglass pipe wall.

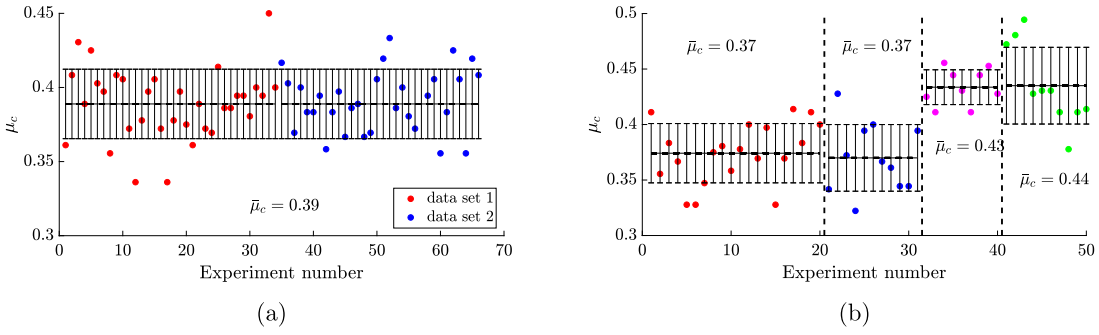


**Fig. A.3.** Coulomb coefficient of static friction between (a) polystyrene particles and (b) polystyrene particles and a plexiglass wall. The solid bars show the standard deviation of the measurements.

Water absorption by the polystyrene particles over the course of the experiments is negligible. This was checked by comparing the weight of a sample batch of particles after 1 week of immersion in water. To assess the effect of wear on the particles in the test loop, the particle diameter was remeasured after 40 h of slurry flow loop operation. The distribution in particle size before and after operation is shown in Fig. A.4a where the particle diameters were measured from circle fitting of particle images by means of a circle Hough transform in MATLAB (Atherton and Kerbyson, 1999; Yuen et al., 1990). The particles undergo some wear over the course of operation, as observed in the mean particle diameter which slightly decreased to 1.97 mm.

Uncertainty in the measured temperature yields an uncertainty in the value of the kinematic viscosity of the water as this was determined from the measured temperature: $\delta\nu_f = |\partial\nu_f/\partial T|\delta T$. Fig. A.4b shows the variation in the viscosity of water as a function of temperature, from which $\partial\nu_f/\partial T$ was determined by means of a least squares line fit. The water density was determined also from the measured temperature where we assumed that the related uncertainty was negligible. The uncertainty in the mass and diameter of 20 individual particles was measured using a microgram weighing scale and a microscope (using again a circle Hough transform to fit circles to the particle images),

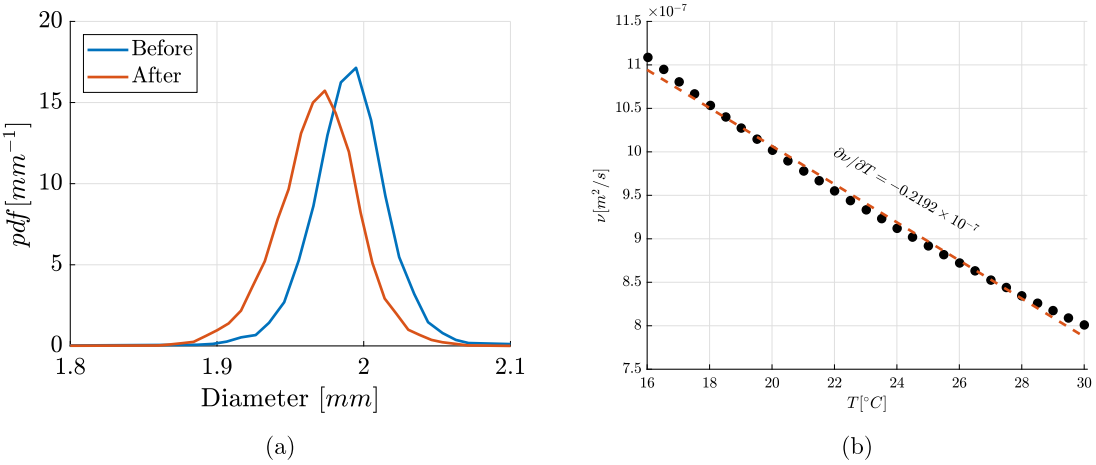


**Fig. A.4.** (a) Distribution in particle diameter before and after 40 h of operation of the slurry flow loop indicated in blue and red, respectively. (b) Variation of kinematic viscosity of water as a function of temperature in the range where the experiments were performed, with the least squares line fit indicated by a red dashed line. (For interpretation of the references to color in this figure legend, the reader is referred to the web version of this article.)

**Table A.1**
Parameters related to the polystyrene spheres used in the slurry flow loop at $T = 25\,°C$.

| | | |
|---|---|---|
| $D_p$ | 2.02 | $\pm$ 4.07 × $10^{-3}$ mm |
| $m$ | 4.39 ×$10^{-6}$ | $\pm$ 0.04 × $10^{-6}$ kg |
| $\rho_p$ | 1018 | $\pm$ 11 kg/m$^3$ |
| $Ga$ | 37.88 | $\pm$ 12.27 |

respectively. The uncertainty in $\rho_p$ was estimated from this by:

$$\delta\rho_p = \rho_p \sqrt{\left(\frac{\delta m}{m}\right)^2 + 9\left(\frac{\delta D_p}{D_p}\right)^2}\,. \tag{A.1}$$

Finally, the uncertainty in $Ga$ was computed from:

$$\delta Ga = Ga\sqrt{\frac{1}{4}\left[\frac{\rho_p/\rho_f}{\rho_p/\rho_f - 1}\right]^2\left(\frac{\delta m}{m}\right)^2 + \frac{9}{4}\left[\frac{1}{\rho_p/\rho_f - 1}\right]^2\left(\frac{\delta D_p}{D_p}\right)^2 + \left(\frac{\delta \nu_f}{\nu_f}\right)^2}\,. \tag{A.2}$$

The uncertainty in particle diameter, mass, density and $Ga$ of the particles are listed in Table A.1, where the value of $Ga$ was determined using the kinematic viscosity of water at a temperature of 25 °C. The actual value of $Ga$ was determined for each case E1–E3 based on the corresponding water temperature during the experiment (listed in Table 1).

## Appendix B. Estimate of intrinsic liquid bulk velocity in test section of slurry loop

The estimation of the intrinsic liquid bulk velocity in the test section, $v_{bl}$, involved three steps, which are discussed below in detail.

1. **Estimation of solid volume flux**
   Fig. B.1 (left) shows a snapshot of the test section recorded at a frame rate of 1125 Hz. By scanning the row of pixels along the horizontal extent at each vertical pixel over all recorded frames, a $y-t$ diagram for each vertical pixel position was obtained. An example of such a $y-t$ diagram is depicted in Fig. B.1 (right), where the entire range of pixels in the horizontal is shown in the horizontal axis and the vertical axis shows the variation in pixel intensity over time. Here, the bright and dark pixels correspond to the particles and fluid, respectively.
   The mean particle velocity profile in the test section was estimated either by manually tracking lines corresponding to a particular intensity or by performing a temporal auto-correlation of each row of pixels in the video data. The two approaches yield comparable results, see Fig. B.2, and we decided to use the manual approach in the sequel. The video data presents a planar view of the pipe cross-section and therefore it is not possible to perceive depth from the video data. We expect that particles close to the center of the pipe will travel at a higher velocity than particles closer to the walls of the pipe. Hence, we might underpredict the depth-averaged particle velocity. Nevertheless, the solid volume flux in the test section, $Q_p$, was estimated using the expression:

$$Q_p = \int_0^{D_{pipe}} \bar{\phi}(z) 2l(z) \overline{v}_p(z) dz\,, \tag{B.1}$$

   where $\bar{\phi}(z)$ is the mean vertical concentration profile (averaged over $x$) obtained from the ERT sensor, $l(z) = \sqrt{z(D_{pipe} - z)}$ is the lateral half width of the pipe at a height $z$, and $\overline{v}_p(z)$ is the mean streamwise velocity profile of the particles.
2. **Estimation of the particle concentration in the riser**
   For fully developed flow, the solid volume fluxes of the particles in the riser and the test section have to be equal to each other and are given by the expression:

$$c_r A_{pipe} v_{bs,r} = Q_p\,, \tag{B.2}$$

   where $c_r$ is the concentration of particles in the riser, $v_{bs,r}$ is the bulk velocity of particles in the riser, and $A_{pipe}$ is the cross-sectional area of the pipe. By rewriting $v_{bs,r}$ as the difference of the liquid bulk velocity and the sedimentation velocity of the particles in the riser, we estimated the riser concentration $c_r$ using the expression:

$$c_r = (Q_p/A_{pipe})/(v_{bl,r} - v_{sed}(c_r, Re_T, D_p/D_{pipe}))\,, \tag{B.3}$$

   where $v_{bl,r}$, $v_{sed}$ and $Re_T$ are the liquid bulk velocity in the riser, the mean sedimentation velocity of particles in a quiescent fluid and the terminal Reynolds number of a single settling particle in free space, respectively. The liquid bulk velocity in the riser is known (from measurements using the magnetic flow meter installed in the riser). The sedimentation velocity was estimated using a correlation for the settling velocity of particles given by Richardson and Zaki (1954):

$$v_{sed} = v_T(1 - c_r)^n\,, \tag{B.4}$$

   where we calculated $n$ based on a correlation from Richardson and Zaki for $1 < Re_T < 200$, given by:

$$n = (4.45 + 18 D_p/D_{pipe}) Re_T^{-0.1}\,. \tag{B.5}$$

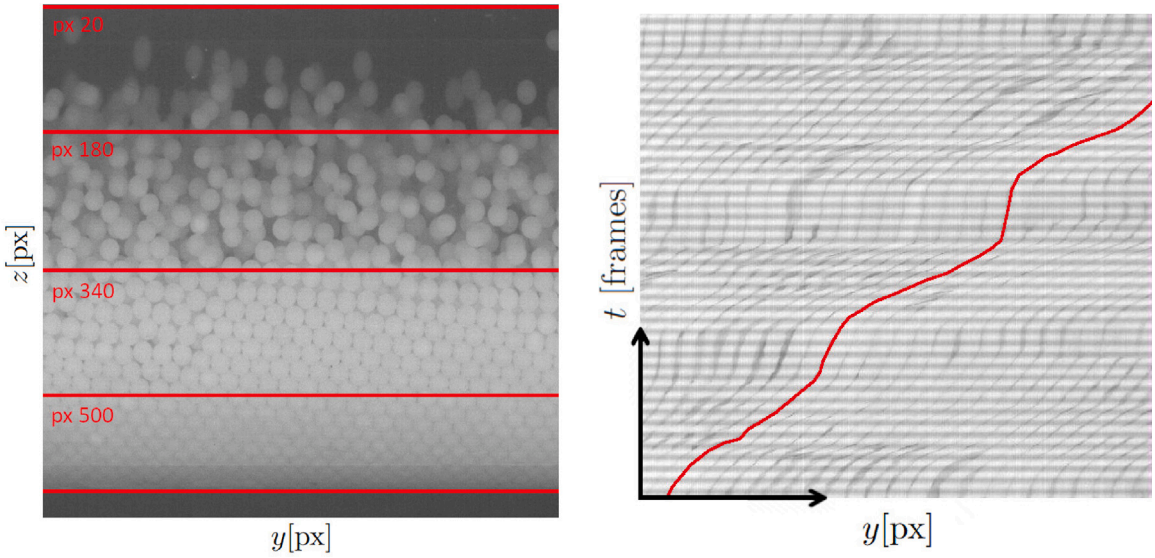


**Fig. B.1.** Instantaneous snapshot (left) of the flow from the video recording at a frame size of 650 × 650 pixels. Some of the scanning lines along the horizontal at different vertical pixel heights are indicated in red. The evolution of the particle position with time along vertical pixel height 340 is shown on the right. (For interpretation of the references to color in this figure legend, the reader is referred to the web version of this article.)

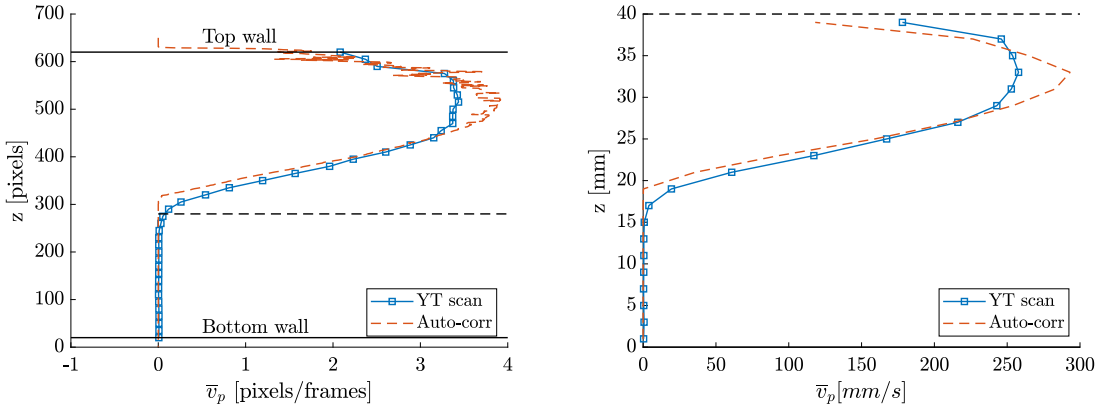


**Fig. B.2.** Mean velocity of the particles in pixels/frames (left) and the same in mm/s (right). In the right figure, a moving mean filter with a width equal to one particle diameter was applied to the velocity profile. The blue and red dashed lines correspond to the estimation performed manually and using the temporal autocorrelation, respectively. (For interpretation of the references to color in this figure legend, the reader is referred to the web version of this article.)

The terminal settling Reynolds number of a particle was estimated from a balance between the net gravity force and the drag force acting on a settling particle (Raaghav et al., 2022), using Abraham's correlation for the sphere drag coefficient (Abraham, 1970), given by:

$$Re_T = \frac{Ga}{\frac{\sqrt{3}}{2}\left(\sqrt{\frac{24}{Re_T}} + 0.5407\right)}. \tag{B.6}$$

Note that the Galileo number of the polystyrene particles is known. The terminal settling velocity of the particles was computed using the expression $v_T = Re_T \nu_f / D_p$.

3. **Estimation of the liquid bulk velocity in the test section**
For fully developed flow, the liquid volume flux in the riser and the test section have to be equal, from which the liquid bulk velocity in the test section was finally estimated using the relation $v_{bl,t} = ((1 - c_r)/(1 - c_t))v_{bl,r}$. The estimated liquid bulk velocity for E1–E3 is given in Table B.1 and this estimate for the liquid bulk velocity was used to calculate the bulk liquid Reynolds number, $Re$, in the test section.

**Table B.1**
Table showing the estimated bulk concentration of particles in the riser, $c_r$, the measured bulk concentration in the test section, $c_t$, and the measured liquid bulk velocity in the riser, $v_{bl,r}$ and the estimated liquid bulk velocity in the test section $v_{bl,t}$.

| | $c_r$ | $c_t$ | $v_{bl,r}$ [mm/s] | $v_{bl,t}$ [mm/s] |
|---|---|---|---|---|
| E1 | 0.12 | 0.33 | 57 | 75 |
| E2 | 0.14 | 0.28 | 164 | 196 |
| E3 | 0.17 | 0.27 | 283 | 320 |

## Appendix C. Volume penalization method and driving pressure gradient

The wall of the pipe is implemented by means of a volume-penalization method (Kajishima et al., 2001; Breugem et al., 2014). The no-slip/no-penetration condition on the pipe wall is enforced by the projection:

$$\mathbf{u}^* \rightarrow \beta \mathbf{u}^*, \tag{C.1}$$

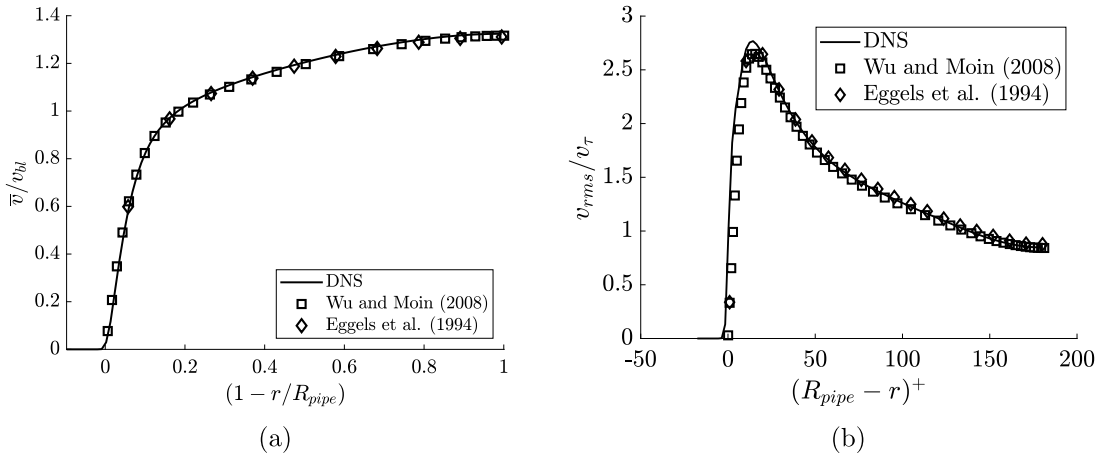


**Fig. C.1.** DNS of single-phase pipe flow at $Re = 5300$ compared with results of Eggels et al. (1994) and Wu and Moin (2008). (a) Mean streamwise velocity as function of radial distance from the pipe wall. (b) Streamwise root-mean-square (rms) velocity scaled with the wall friction velocity ($v_\tau$) and plotted as function of radial distance from the pipe wall measured in viscous wall units.

where $\mathbf{u}^*$ is a provisional velocity estimate obtained from Eq. (1b) in the fractional step scheme and $\beta$ is the local pipe wall volume fraction in a fluid grid cell. The latter is computed from a midpoint quadrature rule (Kempe et al., 2009) to have a value of 1 in cells fully within the pipe, 0 in the cells fully outside it and an intermediate value for cells cut by the pipe wall:

$$\beta = \frac{\sum_{l=1}^{8} S_l H(S_l)}{\sum_{l=1}^{8} |S_l|}, \tag{C.2}$$

where $l$ runs over the 8 corners of the fluid grid cell and $H$ is the Heaviside function given by:

$$H(x) = \begin{cases} 1 & x \geq 0 \\ 0 & x < 0 \end{cases}.$$

$S_l$ is the signed distance function to the pipe wall ($S_l > 0$ corresponds to the interior of the pipe), given by:

$$S_l = R_{pipe} - \sqrt{(x_l - x_c)^2 + (z_l - z_c)^2}, \tag{C.3}$$

where $R_{pipe}$ is the pipe radius, and $x_c$ and $z_c$ are the coordinates of the centerline of the pipe.

The streamwise pressure gradient that drives the flow, is computed from the requirement that the non-dimensional intrinsic liquid bulk velocity has to be kept constant at a value of 1. At Runge–Kutta level 1 it is computed from:

$$-\left.\frac{dp_e}{dy}\right|_{\alpha=1} = -\left.\frac{dp_e}{dy}\right|_{\alpha=0} + (1-\phi_b)\left(\frac{1 - v_{bl}^*|_{\alpha=1}}{RK_{\alpha=1}\Delta t}\right), \tag{C.4}$$

where $\alpha = 0$ refers to the previous time step, $\Delta t$ is the time step, $RK_\alpha$ is the Runge–Kutta coefficient at Runge–Kutta step $\alpha$, and $v_{bl}^*$ is the provisional phase-averaged fluid bulk velocity computed after the projection step (see Eq. (C.1)). The pressure gradient is kept constant at this value after the first Runge–Kutta step, i.e.:

$$-\left.\frac{dp_e}{dy}\right|_{\alpha=3} = -\left.\frac{dp_e}{dy}\right|_{\alpha=2} = -\left.\frac{dp_e}{dy}\right|_{\alpha=1}. \tag{C.5}$$

This method has been validated by performing DNS of a turbulent single-phase pipe flow at $Re = 5300$ and using the same grid resolution as in the slurry flow simulations ($\Delta x/D_{pipe} = 1/320$, corresponding to $\Delta x^+ = 1.13$ here, which is of the same order as the values given in Table 2 for the DNS of slurry pipe flow). The results are compared with single-phase pipe flow simulations of Eggels et al. (1994) and Wu and Moin (2008). Excellent agreement is found for the mean and rms streamwise velocity, see Fig. C.1.

## Appendix D. Friction factor models for slurry pipe flow

In this appendix, details are provided of the Darcy–Weisbach friction factor models for slurry pipe flow used for the comparison with the DNS and experimental data in Fig. 5.

### *Model for the fixed-bed regime*

To model the friction factor for this regime, we assume first that the great majority of the liquid flow is confined to the channel region above the bed. The liquid bulk velocity in the channel region, $v_{blc}$, is approximated from the liquid bulk velocity through the entire pipe, $v_{bl}$, as:

$$v_{blc} \approx (1 - \phi_b) A_{pipe} v_{bl} / A_c, \tag{D.1}$$

where $A_{pipe}$ and $A_c$ are the cross-sectional area of the pipe and channel region, respectively. Following the methodology described in chapter 6.8 of White (2011), the streamwise pressure gradient for the channel region is estimated from the analogy of the flow through the non-circular channel with flow through a circular pipe with a hydraulic diameter $D_H = 4A_c/P_c$ with $P_c$ the perimeter of the channel. The relative roughness height of the equivalent pipe is estimated by $\epsilon = D_p/D_H$. This yields the following model for the friction factor in the fixed-bed regime:

$$f_{FB} = f_{SPR}(Re_c, \epsilon) \cdot \frac{D_{pipe}}{D_H} \frac{v_{blc}^2}{v_{mix}^2}, \tag{D.2}$$

where $Re_c = v_{blc} D_H / \nu_f$ is the apparent Reynolds number for the equivalent pipe. $f_{SPR}$ is the friction factor for the single-phase flow reference, which we estimated from the correlation of Haaland (1983):

$$f_{SPR} = \left(1.8 \log_{10}\left[\frac{6.9}{Re} + \left(\frac{\epsilon}{3.7}\right)^{1.11}\right]\right)^{-2}. \tag{D.3}$$

Given that $\phi_b = 0.325$ in the fixed-bed case E1/D1 and assuming an average bed packing fraction of 0.64, we estimated that $A_c \approx A_{pipe}/2$ and $P_c \approx (\pi/2 + 1) D_{pipe}$.

### *Durand and Condolios model (1953)*

The original model for the friction factor proposed by Durand and Condolios (1953) is given by:

$$f_{DC} = f_{SPR}\left(1 + 176\,\phi_d \left[\frac{v_{mix}^2}{|\tilde{\mathbf{g}}| D_{pipe}} \frac{\sqrt{|\tilde{\mathbf{g}}| D_p}}{v_T}\right]^{-1.5}\right), \tag{D.4}$$

**Table D.1**
Darcy–Weisbach friction factor $f_{DNS}$, $f_{EXP}$, $f_{FB}$, $f_{DC}$, $f_{MDC}$, $f_{NSB}$, $f_{NHS}$ and $f_{ELM}$ obtained from, respectively, DNS, experiment, proposed model for the fixed-bed regime, Durand and Condolios model (Durand and Condolios, 1953), modified Durand and Condolios model based on the reduced gravity (Newitt et al., 1955), Newitt et al. model for the sliding-bed regime (Newitt et al., 1955), Newitt et al. model for the heterogeneous suspension regime (Newitt et al., 1955), and equivalent liquid model.

| Case | $Re_{mix}$ | $f_{DNS}$ | $f_{EXP}$ | $f_{FB}$ | $f_{DC}$ | $f_{MDC}$ | $f_{NSB}$ | $f_{NHS}$ | $f_{ELM}$ |
|---|---|---|---|---|---|---|---|---|---|
| D1/E1 | 2347 | 0.607 | 0.939 | 0.576 | 35.7 | 1.351 | 0.575 | 2.909 | 0.077 |
| D2/E2 | 7812 | 0.118 | 0.149 | 0.377 | 2.4 | 0.121 | 0.153 | 0.226 | 0.045 |
| D3/E3 | 14 164 | 0.058 | 0.062 | 0.313 | 0.46 | 0.044 | 0.068 | 0.063 | 0.036 |

where $f_{SPR}$ is the estimated friction factor for pure liquid pipe flow, which is estimated here from the Haaland correlation for a hydraulically smooth pipe, see Eq. (D.3), $\phi_d = \phi_b v_{bs}/(\phi_b v_{bs} + (1-\phi_b)v_{bl})$ is the so-called delivered concentration, and $v_T$ is the terminal velocity of a single settling particle in free space. The latter can be calculated from the Galileo number according to $Re_T = \sqrt{\frac{4}{3C_d}}Ga$ (Raaghav et al., 2022), where $Re_T = v_T D_p/\nu_f$ is the terminal Reynolds number and $C_d = (\sqrt{24/Re_T} + 0.5407)^2$ is the sphere drag coefficient estimated here from Abraham's drag correlation (Abraham, 1970). We note that the coefficient of 176 in Eq. (D.4) was not given explicitly by Durand and Condolios, but it can be deduced from the line fit presented in Fig. 17b of their paper (Durand and Condolios, 1953).

As discussed by Miedema (2016), Durand and Condolios (1953) normalized $v_T$ with $\sqrt{|\tilde{\mathbf{g}}|D_p}$ and $v_{mix}$ with $\sqrt{|\tilde{\mathbf{g}}|D_{pipe}}$. To account for the Archimedes force on the particles, it is deemed more appropriate to multiply $|\tilde{\mathbf{g}}|$ with the relative density difference between the particles and the fluid, $(\rho_p/\rho_f - 1)|\tilde{\mathbf{g}}|$, i.e., to replace the gravity by the *reduced* gravity. Since Durand and Condolios proposed their correlation based on a fit to experimental data for sand/water slurries with a fixed density ratio of $\rho_p/\rho_f \approx 2.65$, their correlation can be modified in a straightforward manner according to:

$$f_{MDC} = f_{SPR}\left(1 + 121\,\phi_d\left[Fr^2\frac{\sqrt{(\rho_p/\rho_f - 1)|\tilde{\mathbf{g}}|D_p}}{v_T}\right]^{-1.5}\right). \tag{D.5}$$

Eq. (D.5) is precisely the form of the Durand and Condolios model as given by Newitt et al. (1955) (p. 94), but we will refer to this correlation as the *modified* Durand and Condolios model as it is different from the original model when the density ratio is not equal to 2.65.

### *Models of Newitt et al. (1955)*

Newitt et al. (1955) distinguished between a sliding-bed and a heterogeneous suspension regime. For the sliding-bed regime, the authors assumed that the excess pressure gradient from the solids (with respect to single-phase pipe flow at the same mixture bulk velocity) can be modeled from the frictional contact force exerted by the pipe wall onto the moving bed. Based on this, they proposed the following model for the friction factor in the sliding-bed regime:

$$f_{NSB} = f_{SPR}\left[1 + 66\,\phi_d\frac{1}{Fr^2}\right], \tag{D.6}$$

where the coefficient of 66 was obtained from a best fit with their experimental data. For the heterogeneous suspension regime, the authors assumed that the suspended solids are responsible for an excess pressure gradient needed to provide the required power for maintaining the solids suspended in the flow. Based on this, they proposed the following model for the friction factor in the heterogeneous suspension regime:

$$f_{NHS} = f_{SPR}\left(1 + 1100\,\phi_d\frac{1}{Fr^3}\frac{v_T}{\sqrt{(\rho_p/\rho_f - 1)|\tilde{\mathbf{g}}|D_p}}\sqrt{\frac{D_p}{D_{pipe}}}\right), \tag{D.7}$$

where the value of 1100 is an empirically determined coefficient to provide the best fit with their experiments.

### *Equivalent liquid model*

The equivalent liquid model is based on the assumption that the particles are homogeneously suspended in the flow and very small (i.e., a small diameter and response time relative to the length and time scales of the liquid flow). In that particular case, it may be expected that the suspension behaves like an equivalent liquid based on the mixture density and suspension viscosity with a friction factor given by:

$$f_{ELM} = f_{SPR}\cdot\frac{\rho_{mix}}{\rho_f}, \tag{D.8}$$

where $f_{SPR}$ is the friction factor for the single-phase flow reference based on $Re_s$, the suspension Reynolds number defined as $Re_s = \rho_{mix} v_{mix} D_{pipe}/\mu_s$ with $\rho_{mix} = \rho_s\phi_b + \rho_f(1-\phi_b)$ the mixture mass density and $\mu_s$ the suspension viscosity. We computed $f_{SPR}$ from Haaland's correlation, Eq. (D.3), for a hydraulically smooth pipe, and estimated $Re_s$ using the suspension viscosity from Eilers' correlation, Eq. (6).

### *Friction factor data*

The above friction factor models have been evaluated for the conditions of cases D1/E1, D2/E2 and D3/E3. The data is provided in Table D.1 and shown in Fig. 5.

## References


Abraham, F.F., 1970. Functional dependence of drag coefficient of a sphere on Reynolds number. Phys. Fluids 13 (8), 2194–2195.

Arolla, S.K., Desjardins, O., 2015. Transport modeling of sedimenting particles in a turbulent pipe flow using Euler—Lagrange large eddy simulation. Int. J. Multiph. Flow 75, 1–11.

Atherton, T.J., Kerbyson, D.J., 1999. Size invariant circle detection. Image Vis. Comput. 17 (11), 795–803.

Balachandar, S., Eaton, J.K., 2010. Turbulent dispersed multiphase flow. Annu. Rev. Fluid Mech. 42, 111–133.

Batchelor, G., 1970. The stress system in a suspension of force-free particles. J. Fluid Mech. 41 (3), 545–570.

Baule, A., Mari, R., Bo, L., Portal, L., Makse, H.A., 2013. Mean-field theory of random close packings of axisymmetric particles. Nature Commun. 4 (1).

Bernier, R.N., Brennen, C.E., 1983. Use of the electromagnetic flowmeter in a two-phase flow. Int. J. Multiph. Flow 9 (3), 251–257.

Bradshaw, P., 1987. Turbulent secondary flows. Annu. Rev. Fluid Mech. 19 (1), 53–74.

Brennen, C.E., 2005. Fundamentals of Multiphase Flow. Cambridge University Press.

Breugem, W.-P., 2012. A second-order accurate immersed boundary method for fully resolved simulations of particle-laden flows. J. Comput. Phys. 231 (13), 4469–4498.

Breugem, W.-P., Boersma, B.J., 2005. Direct numerical simulations of turbulent flow over a permeable wall using a direct and a continuum approach. Phys. Fluids 17 (2), 025103.

Breugem, W.-P., Boersma, B.J., Uittenbogaard, R.E., 2006. The influence of wall permeability on turbulent channel flow. J. Fluid Mech. 562, 35–72.

Breugem, W.-P., van Dijk, V., Delfos, R., 2014. Flows through real porous media: X-ray computed tomography, experiments, and numerical simulations. J. Fluids Eng. 136 (4), 040902.

Campbell, C.S., Avila-Segura, F., Liu, Z., 2004. Preliminary observations of a particle lift force in horizontal slurry flow. Int. J. Multiph. Flow 30 (2), 199–216.

Capecelatro, J., Desjardins, O., 2013a. An Euler–Lagrange strategy for simulating particle-laden flows. J. Comput. Phys. 238, 1–31.

Capecelatro, J., Desjardins, O., 2013b. Eulerian–Lagrangian modeling of turbulent liquid–solid slurries in horizontal pipes. Int. J. Multiph. Flow 55, 64–79.

Chen, L., Duan, Y., Pu, W., Zhao, C., 2009. CFD simulation of coal-water slurry flowing in horizontal pipelines. Korean J. Chem. Eng. 26 (4), 1144–1154.

Costa, P., Boersma, B.J., Westerweel, J., Breugem, W.-P., 2015. Collision model for fully resolved simulations of flows laden with finite-size particles. Phys. Rev. E 92, 053012.

Costa, P., Picano, F., Brandt, L., Breugem, W.-P., 2016. Universal scaling laws for dense particle suspensions in turbulent wall-bounded flows. Phy. Rev. Lett. 117, 134501.

Costa, P., Picano, F., Brandt, L., Breugem, W.-P., 2018. Effects of the finite particle size in turbulent wall-bounded flows of dense suspensions. J. Fluid Mech. 843, 450–478.

Deen, N.G., Westerweel, J., Delnoij, E., 2002. Two-phase PIV in bubbly flows: Status and trends. Chem. Eng. Technol. 25 (1), 97–101.

Desmond, K.W., Weeks, E.R., 2014. Influence of particle size distribution on random close packing of spheres. Phys. Rev. E 90 (2), 022204.

Doron, P., Barnea, D., 1993. A three-layer model for solid-liquid flow in horizontal pipes. Int. J. Multiph. Flow 19, 1029–1043.

Doron, P., Barnea, D., 1996. Flow pattern maps for solid-liquid flow in pipes. Int. J. Multiph. Flow 22 (2), 273–283.

Doron, P., Granica, D., Barnea, D., 1987. Slurry flow in horizontal pipes - Experimental and modeling. Int. J. Multiph. Flow 13 (4), 535–547.

Durand, R., 1953. Basic relationships of the transportation of solids in pipes—Experimental research. In: Proceedings 5th Minneapolis International Hydraulics Convention. pp. 89–103.

Durand, R., Condolios, E., 1953. Étude expérimentale du refoulement des matériaux en conduites, en particulier des produits de dragage et des schlamms. J. Hydraul. 2 (1), 29–55.

Eggels, J.G.M., Unger, F., Weiss, M.H., Westerweel, J., Adrian, R.J., Friedrich, R., Nieuwstadt, F.T.M., 1994. Fully developed turbulent pipe flow: a comparison between direct numerical simulation and experiment. J. Fluid Mech. 268, 175–210.

Eilers, H., 1941. Die Viskosität von Emulsionen hochviskoser Stoffe als Funktion der Konzentration. Kolloid-Zeitschrift 97 (3), 313–321.

Ekambara, K., Sanders, R.S., Nandakumar, K., Masliyah, J.H., 2009. Hydrodynamic simulation of horizontal slurry pipeline flow using ANSYS-CFX. Ind. Eng. Chem. Res. 48 (17), 8159–8171.

Elghobashi, S., 1994. On predicting particle-laden turbulent flows. Appl. Sci. Res. 52, 309–329.

Fadlun, E.A., Verzicco, R., Orlandi, P., Mohd-Yusof, J., 2000. Combined immersed-boundary finite-difference methods for three-dimensional complex flow simulations. J. Comput. Phys. 161 (1), 35–60.

Fornari, W., Kazerooni, H.T., Hussong, J., Brandt, L., 2018. Suspensions of finite-size neutrally buoyant spheres in turbulent duct flow. J. Fluid Mech. 851, 148–186.

Führböter, A., 1961. Über die Förderung von Sand-Wasser-Gemischen in Rohrleitungen. Mitteilungen des Franzius-Instituts für Grund- und Wasserbau der Technischen Hochschule Hannover, Heft 19. Eigenverlag, Hannover.

Gibert, R., 1960. Transport hydraulique et refoulement des mixtures en conduites. Ann. Ponts Chaussées 130 (3), 307–374.

Guazzelli, É., Morris, J.F., 2011. A Physical Introduction to Suspension Dynamics. In: Cambridge Texts in Applied Mathematics, Cambridge University Press.

Guazzelli, É., Pouliquen, O., 2018. Rheology of dense granular suspensions. J. Fluid Mech. 852, P1.

Gurung, A., Haverkort, J.W., Drost, S., Norder, B., Westerweel, J., Poelma, C., 2016. Ultrasound image velocimetry for rheological measurements. Meas. Sci. Technol. 27 (9), 094008:1–9.

Haaland, S.E., 1983. Simple and explicit formulas for the friction factor in turbulent pipe flow. J. Fluids Eng. 105 (1), 89–90.

Hogendoorn, W.J., 2021. Suspension Dynamics in Transitional Pipe Flow (Ph.D. thesis). Delft University of Technology.

Hogendoorn, W., Breugem, W.-P., Frank, D., Bruschewski, M., Grundmann, S., Poelma, C., 2023. From nearly homogeneous to core-peaking suspensions: Insight in suspension pipe flows using MRI and DNS. Phys. Rev. Fluids 8, 124302.

Kajishima, T., Takiguchi, S., Hamasaki, H., Miyake, Y., 2001. Turbulence structure of particle-laden flow in a vertical plane channel due to vortex shedding. JSME Int. J. B 44 (4), 526–535.

Kaushal, D.R., Thinglas, T., Tomita, Y., Kuchii, S., Tsukamoto, H., 2012. CFD modeling for pipeline flow of fine particles at high concentration. Int. J. Multiph. Flow 43, 85–100.

Kaushal, D.R., Tomita, Y., 2007. Experimental investigation for near-wall lift of coarser particles in slurry pipeline using $\gamma$-ray densitometer. Powder Technol. 172 (3), 177–187.

Kazerooni, H.T., Fornari, W., Hussong, J., Brandt, L., 2017. Inertial migration in dilute and semidilute suspensions of rigid particles in laminar square duct flow. Phys. Rev. Fluids 2, 084301.

Kempe, T., Schwarz, S., Fröhlich, J., 2009. Modelling of spheroidal particles in viscous flows. In: Proceedings of the Academy Colloquium Immersed Boundary Methods: Current Status and Future Research Directions, KNAW, Amsterdam, the Netherlands. vol. 845.

Kidanemariam, A.G., Uhlmann, M., 2014. Direct numerical simulation of pattern formation in subaqueous sediment. J. Fluid Mech. 750, R2.

Kidanemariam, A.G., Uhlmann, M., 2017. Formation of sediment patterns in channel flow: minimal unstable systems and their temporal evolution. J. Fluid Mech. 818, 716–743.

Lareo, C., Fryer, P.J., Barigou, M., 1997. The fluid mechanics of two-phase solid-liquid food flows: a review. Food Bioprod. Process. 75 (2), 73–105.

Larsson, I.A.S., Lindmark, E.M., Lundström, T.S., Nathan, G.J., 2011. Secondary flow in semi-circular ducts. J. Fluids Eng. 133 (10), 101206.

Lashgari, I., Picano, F., Breugem, W.-P., Brandt, L., 2014. Laminar, turbulent, and inertial shear-thickening regimes in channel flow of neutrally buoyant particle suspensions. Phys. Rev. Lett. 113 (25), 254502.

Lashgari, I., Picano, F., Breugem, W.-P., Brandt, L., 2016. Channel flow of rigid sphere suspensions: Particle dynamics in the inertial regime. Int. J. Multiph. Flow 78, 12–24.

Leighton, D., Acrivos, A., 1987. The shear-induced migration of particles in concentrated suspensions. J. Fluid Mech. 181, 415–439.

Lin, Z.-W., Shao, X.-M., Yu, Z.-S., Wang, L.-P., 2017a. Effects of finite-size heavy particles on the turbulent flows in a square duct. J. Hydrodyn. B 29 (2), 272–282.

Lin, Z., Yu, Z., Shao, X., Wang, L.-P., 2017b. Effects of finite-size neutrally buoyant particles on the turbulent flows in a square duct. Phys. Fluids 29 (10), 103304.

Ling, J., Skudarnov, P.V., Lin, C.X., Ebadian, M.A., 2003. Numerical investigations of liquid–solid slurry flows in a fully developed turbulent flow region. Int. J. Heat Fluid Flow 24 (3), 389–398.

Liu, M., Zhao, Y., Yan, Y., Fairweather, M., Yao, J., 2023. Particle behavior in a turbulent pipe flow with a flat bed. Particuology (ISSN: 1674-2001) 81, 58–72.

Macdonald, I.F., El-Sayed, M.S., Mow, K., Dullien, F.A.L., 1979. Flow through porous media-the Ergun equation revisited. Ind. Eng. Chem. Fundam. 18 (3), 199–208.

Maxey, M., 2017. Simulation methods for particulate flows and concentrated suspensions. Annu. Rev. Fluid Mech. 49 (1), 171–193.

McLaughlin, J.B., 1991. Inertial migration of a small sphere in linear shear flows. J. Fluid Mech. 224, 261–274.

Messa, G.V., Matoušek, V., 2020. Analysis and discussion of two fluid modelling of pipe flow of fully suspended slurry. Powder Technol. 360, 747–768.

Miedema, S.A., 2016. In: Ramsdell, R.C. (Ed.), Slurry Transport: Fundamentals, A historical overview and the Delft Head Loss & Limit Deposit Velocity Framework, first ed. S. A. Miedema / Delft University of Technology.

Newitt, D.M., Richardson, J.F., Abbott, M., Turtle, R.B., 1955. Hydraulic conveying of solids in horizontal pipes. Trans. Inst. Chem. Eng. 33, 93–113.

Nezu, I., 2005. Open-channel flow turbulence and its research prospect in the 21st century. J. Hydraul. Eng. 131 (4), 229–246.

Nikitin, N.V., Popelenskaya, N.V., Stroh, A., 2021. Prandtl's secondary flows of the second kind. Problems of description, prediction, and simulation. Fluid Dyn. 56 (4), 513–538.

Ouriemi, M., Aussillous, P., Medale, M., Peysson, Y., Guazzelli, É., 2007. Determination of the critical shields number for particle erosion in laminar flow. Phys. Fluids 19 (6), 061706.

Peskin, C.S., 1972. Flow patterns around heart valves: A numerical method. J. Comput. Phys. 10 (2), 252–271.

Picano, F., Breugem, W.-P., Brandt, L., 2015. Turbulent channel flow of dense suspensions of neutrally buoyant spheres. J. Fluid Mech. 764, 463–487.

Picano, F., Breugem, W.-P., Mitra, D., Brandt, L., 2013. Shear thickening in non-Brownian suspensions: An excluded volume effect. Phys. Rev. Lett. 111, 098302.

Pope, S.B., 2000. Turbulent Flows. Cambridge University Press.

Prandtl, L., 1952. Essentials of Fluid Dynamics with Applications to Hydraulics, Aeronautics, Meteorology and Other Subjects. Hafner Pub..

Raaghav, S.K.R., Poelma, C., Breugem, W.-P., 2022. Path instabilities of a freely rising or falling sphere. Int. J. Multiph. Flow 153, 104111.

Radhakrishnan, A.K.T., 2019. Domestic Slurry Hydraulics in Transport. (Ph.D. thesis). Delft University of Technology.

Ramsdell, R.C., Miedema, S.A., 2013. An overview of flow regimes describing slurry transport. In: Proceedings WODCON XX: The art of dredging, Brussels (Belgium), 3–7 June 2013. p. 16.

Richardson, J.F., Zaki, W.N., 1954. Sedimentation and fluidization: Part I. Trans. Inst. Chem. Eng. 32, 35–53.

van Rijn, L.C., 1984. Sediment transport, Part II: Suspended load transport. J. Hydraul. Eng. 110 (11), 1613–1641.

Saffman, P.G., 1965. The lift on a small sphere in a slow shear flow. J. Fluid Mech. 22 (2), 385–400.

Shajahan, T., Breugem, W.-P., 2020. Influence of concentration on sedimentation of a dense suspension in a viscous fluid. Flow Turbul. Combust. 105 (2), 537–554.

Shajahan, T., Breugem, W.-P., 2023. Inertial effects in sedimenting suspensions of solid spheres in a liquid. Int. J. Multiph. Flow 166, 104498.

Shields, A., 1936. Anwendung der ähnlichkeitsmechanik und der turbulenzforschung auf die geschiebebewegung. pp. 1–26, Preußische Versuchsanstalt für Wasser-, Erd- und Schiffbau (VWS). Heft 26..

Stickel, J.J., Powell, R.L., 2005. Fluid mechanics and rheology of dense suspensions. Annu. Rev. Fluid Mech. 37, 129–149.

Turian, R.M., Hsu, F.-L., Ma, T.-W., 1987. Estimation of the critical velocity in pipeline flow of slurries. Powder Technol. 51 (1), 35–47.

Uhlmann, M., 2005. An immersed boundary method with direct forcing for the simulation of particulate flows. J. Comput. Phys. 209 (2), 448–476.

Uzi, A., Levy, A., 2018. Flow characteristics of coarse particles in horizontal hydraulic conveying. Powder Technol. 326, 302–321.

Vocadlo, J.J., Charles, M.E., 1972. Prediction of pressure gradient for the horizontal turbulent flow of slurries. In: Proceedings 2nd International Conference on the Hydraulic Transport of Solids in Pipes. pp. 1–14.
White, F.M., 2011. Fluid Mechanics, first ed. Seventh Edition in SI Units. McGraw-Hill.
Wilson, W.E., 1942. Mechanics of flow with noncolloidal, inert solids. Tran. Am. Soc. Civ. Eng. 107 (1), 1576–1586.
Wilson, K.C., Addie, G.R., Sellgren, A., Clift, R., 2006. Slurry Transport Using Centrifugal Pumps. Springer Science & Business Media.
Wilson, K.C., Sellgren, A., 2003. Interaction of particles and near-wall lift in slurry pipelines. J. Hydraul. Eng. 129 (1), 73–76.
Wilson, K., Sellgren, A., 2016. Developments in slurry flow modelling in a historical perspective. Can. J. Chem. Eng. 94, 1019–1024.
Wu, X., Moin, P., 2008. A direct numerical simulation study on the mean velocity characteristics in turbulent pipe flow. J. Fluid Mech. 608, 81–112.
Xu, J.-Y., Wu, Y.-X., Zheng, Z.-C., Wang, M., Munir, B., Oluwadarey, H.I., Schlaberg, H.I., Williams, R.A., 2009. Measurement of solid slurry flow via correlation of electromagnetic flow meter, electrical resistance tomography and mechanistic modelling. J. Hydrodyn. 21 (4), 557–563.
Yuen, H.K., Princen, J., Illingworth, J., Kittler, J., 1990. Comparative study of hough transform methods for circle finding. Image Vis. Comput. 8 (1), 71–77.
Zade, S., Fornari, W., Lundell, F., Brandt, L., 2019. Buoyant finite-size particles in turbulent duct flow. Phys. Rev. Fluids 4, 024303.
Zhang, X., Nathan, G.J., Tian, Z.F., Chin, R.C., 2021a. Flow regimes within horizontal particle-laden pipe flows. Int. J. Multiph. Flow 143, 103748.
Zhang, X., Nathan, G.J., Tian, Z.F., Chin, R.C., 2021b. The influence of the coefficient of restitution on flow regimes within horizontal particle-laden pipe flows. Phys. Fluids 33 (12), 123318.
Zhang, X., Nathan, G.J., Tian, Z.F., Chin, R.C., 2022. The dominant mechanisms for each regime of secondary flows in horizontal particle-laden pipe flows. J. Fluid Mech. 949, A10.